Advanced Serpentine Heat Exchangers to Minimize Number of Joints and Leakage in HVAC&R Systems

DE-EE0007680

Prepared for
United States Department of Energy
Energy Efficiency and Renewable Energy

June 2022

Daniel Bacellar[1], Yoram Shabtay[2], John Black[2], Dennis Nasuta[1], Cara Martin[1], Reinhard Radermacher[1], Max Mzhen[1], Matthew Blaylock[3].

[1] Optimized Thermal Systems, Inc.
[2] Heat Transfer Technologies, LLC
[3] Stone Mountain Technologies, Inc.

Prime Contractor:	**Optimized Thermal Systems, Inc.**
Principal Investigator:	**K. Reinhard Radermacher, Ph.D.**
Lead Technical Engineers:	**Daniel Bacellar**
	Dennis Nasuta
Business Contact:	**Cara Martin**
Subcontractors:	**Heat Transfer Technologies, LLC**
	United Technology Research Center

Acknowledgements

The project team could not have accomplished the successful evaluation of the advanced serpentine heat exchanger technology without the support of several key suppliers and partners including the R&D team at Brazeway for their input on manufacturing and support in prototyping, the team at Virtus Precision Tubes in securing a US-based manufacturing and materials pipeline, and both Sub-Zero, Inc. and Stone Mountain Technologies, Inc. for expressing their interest in the technology and helping to evaluate its potential in the context of their systems.

This material is based upon work supported by the U.S. Department of Energy's Office of Energy Efficiency and Renewable Energy (EERE) under the Building Technologies Office Award Number DE-EE0007680.

Table of Contents

List of Figures

List of Tables

List of Abbreviations

AAO	**Approximation Assisted Optimization**
AC	**Air Conditioning/Conditioner**
AHAM	**Association of Home Appliance Manufacturers**
AHRI	**Air-Conditioning Heating and Refrigeration Institute**
ALT	**Accelerated Life Tests**
BP	**Budget Period**
CAB	**Controlled Atmosphere Brazing**
CAD	**Computer Aided Design**
CEEE	**Center for Environmental Energy Engineering**
CFD	**Computational Fluid Dynamics**
COP	**Coefficient of Performance**
CT	**Computed Tomography**
DO	**Direct Optimization**
DOE	**Department of Energy**
DoE	**Design of Experiments**
EDM	**Electrical Discharge Machining**
FEA	**Finite Element Analysis**
GHG	**Greenhouse Gases**
GWP	**Global Warming Potential**
HFC	**Hydrofluorocarbons**
HP	**Heat Pump**
HPWH	**Heat Pump Water Heater**
HTC	**Heat Transfer Coefficient**
HTT	**Heat Transfer Technologies, LLC**
HVAC&R	**Heating, Ventilation, Air-Conditioning and Refrigeration**
HX	**Heat Exchanger**
LHS	**Latin Hypercube Sampling**
LPM	**Liters per Minute**
MAS	**Maximum Acceptance Score**

MOGA	**Multi-Objective Genetic Algorithm**
OD	**Outer Diameter**
OTS	**Optimized Thermal Systems, Inc.**
PPCFD	**Parallel Parametrized CFD**
PTAC	**Packaged Terminal Air Conditioner**
PTHP	**Packaged Terminal Heat Pump**
Re	**Reynolds Number**
RTPF	**Round Tube and Plate Fin**
SBIR	**Small Business Innovation Research**
SEM	**Scanning Electron Microscopy**
SHX	**Serpentine Heat Exchanger**
SMTI	**Stone Mountain Technologies Institute**
LMTD	**Log Mean Temperature Difference**
UMD	**University of Maryland**
UTC	**United Technologies Corporation**
UTRC	**United Technologies Research Center**
VPT	**Virtus Precision Tube**

Nomenclature

Symbol	Description	Units
AFR	**Air Flowrate**	m^3**/s**
A_{cs}	**Cross-Section Area**	m^2
A_f	**Face Area**	m^3
A_i	**Area**	m^2
cp	**Specific Heat**	**J/kg.K**
D	**Depth**	**m**
D_h	**Hydraulic Diameter**	**m**
D_i	**Tube Inner Diameter**	**m**
D_o	**Tube Outer Diameter**	**m**

Symbol	Description	Units
F	**Friction Factor**	**-**
F_p	**Fin Pitch**	**m**
FPI	**Fins Per Inch**	in^{-1}
H	**Height**	**m**
h	**Air Heat Transfer Coefficient**	$W/m^2.K$
L	**Length**	**m**
L_h	**Louver depth/height**	**m**
L_l	**Louver length**	**m**
MFR	**Refrigerant Mass Flowrate**	**g/s**
$\dot{m}$	**Mass Flow Rate**	**kg/s**
M_r	**Tube Internal Volume**	m^3
N_c	**Number of Circuits**	**-**
N_{DoE}	**DoE Size**	**-**
N_{dv}	**Number of Design Variables**	**-**
N_{joints}	**Number of Joints**	**-**
N_l	**Number of Louvers**	**-**
N_{ll}	**Number of "Lower Louvers"**	**-**
N_r	**Number of Tube Rows**	**-**
N_t	**Number of Tubes per Circuit**	**-**
N_{ul}	**Number of "Upper Louvers"**	**-**
P	**Perimeter**	**m**
P	**Pressure**	**Pa**
P_f	**Refrigerant Penalty Factor in the Flattened Elbow**	**-**
P_l	**Tube Longitudinal Pitch**	**m**
P_t	**Tube Transverse Pitch**	**m**
Q	**Heat Load**	**W**
R_{joints}	**Joint Reduction**	**%**

Symbol	Description	Units
S_c	Slit Count	-
S_d	Diagonal Spacing	m
s_d	Slit Depth	m
s_l	Slit Length	m
s_p	Slit Pitch	m
s_w	Slit Width	m
T_{in}	Temperature	K
u	Air Frontal Velocity	m/s
UA_{air}	Air Thermal Conductance	W/K
V_{air}	Air Volumetric Flowrate	m^3/s
v_m	Material Volume	m^3
$\dot{W}_p$	Air Pumping Power	W
x_{ip}	Quality	-

Greek Symbol	Description	Units
δ_f	Fin Thickness	m
δ_m	Minimum Wall/Edge Distance	m
δ_t	Tube Wall Thickness	m
ΔP_{air}	Air Pressure Drop	Pa
ΔP_{ref}	Refrigerant Pressure Drop	kPa
ζ	Contact Area Reduction Factor	-
η_o	Fin Effectiveness	-
Θ	Dog-Bone Cut Angle	°
ρ	Density	kg/m^3

Subscript	Description
sc	Sub-Cooling
sh	Super-Heating

Executive Summary

Refrigerant leakage has a significant impact on heating, ventilation, air conditioning and refrigeration (HVAC&R) industries in terms of both greenhouse gas (GHG) emissions and lost efficiency of the systems themselves. Refrigerant leakage from HVAC&R equipment constitutes a small but significant source of GHG emissions due to their high global warming potential (GWP). In 2019, the EPA reported that HFCs in refrigeration and AC accounted for about 2.2% of all GHG emissions in the US in 2017. Furthermore, according to the Department of Energy (DOE), "energy consumption increase due to refrigerant leakage can be as high as 30 TBtu over a 10-year span for a single market segment" (Miljkovic et al, 2019) including residential and commercial HVAC applications.

One of the major causes of refrigerant leakage is braze joints within a vapor compression system. The brazing process is often inconsistent and almost always imperfect. As a result, braze joints are left vulnerable to leaks and can be weaker than non-brazed tubing. Conventional tube-fin heat exchangers (HXs) are manufactured using one brazed joint per tube.

An alternative to the conventional HX approach is the use of a single continuous serpentine tube. Serpentine heat exchangers (SHXs), unlike conventional tube-fin HXs, do not require braze joints. Instead, the continuous tube is bent back and forth multiple times and is inserted into a fin pack that has an additional opening to allow for the bent radius to enter. This gap is often referred to as a "dog-bone" fin design given the shape it produces in the fin material. Significantly reducing the number of joints in a system would, by definition, reduce the potential for leakage. Utilizing serpentine aluminum tubes in a HX, as opposed to a conventional round tube plate fin (RTPF) coil, has the potential to eliminate between 70% and 100% of joints in the HX, depending on coil type, size, and pressure drop allowances. This is achieved by significantly reducing the number of U-bend joints requiring brazing.

Serpentine HXs are currently widely used in small capacity refrigerators and coolers, such as those often found in supermarkets, as they are inexpensive, sturdy and remain reliable for long periods of operation. Furthermore, since they operate as evaporators, condensate or frost can fill voids between the fin and the tube, compensating for their poor tube-fin contact resistance relative to convention RTHXs. Current performance limitations, however, render them scarcely used for

commercial and residential HVAC&R applications. As such, there is opportunity to improve on the existing SHX technology by improving the heat transfer to present a new HX solution that reduces the number of joints and continues to compete with conventional technology on the metrics of performance, cost, manufacturability, and durability.

In addition to the significant potential in brazed joint reduction, and consequential refrigerant leakage, SHXs also possess several other direct manufacturing cost-saving advantages including:

- **Reduction or elimination of return U-bends and their brazing, thus eliminating manufacturing steps;**
- **Elimination of the tube expansion process, saving an additional significant manufacturing step and its related equipment;**
- **Internal tube enhancements, like inner grooves, remain undamaged since there is no need for tube expansion, ultimately improving tube efficiency and overall heat transfer performance; and,**
- **Simple construction, with a one-step brazing process to a complete finished product.**

Between October 2016 and September 2021, the concept of an advanced SHX was designed, modeled, prototyped and tested both as an individual heat exchanger and within the context of multiple systems. Initial analysis focused on a residential heat pump application and leveraged computational fluid dynamics (CFD) and CoilDesigner®, a proprietary air-to-refrigerant heat exchanger design and simulation tool. Initial CFD simulations established the baseline and analyzed multiple serpentine replacements, ultimately identifying designs that would reduce the number of joints by 85% and 70% for indoor and outdoor coils, respectively. Further simulations then focused on fin design, particularly different types of fin enhancements. An initial fin design emerged with a vertical dog-bone cut and sets of louvers on the top and bottom. With an initial concept established, a thorough optimization was conducted to refine the design. Benchtop tests focused on the ability to braze the serpentine tubes to the newly optimized enhanced fins. These processes were verified by microsection analysis and deemed ready to apply to full-scale HX prototypes.

Four prototype HXs were constructed with the support of project partners and vendors. Each prototype underwent performance testing in a temperature-

controlled wind tunnel. One prototype further underwent accelerated life tests (ALT) to predict its real-time cyclic life.

With the HX concept proven, the advanced SHXs were implemented within multiple system applications. While the SHX design for a residential heat pump was promising, prototyping a full-size SHX and then bending it as would be typical to include in a residential condensing unit was too risky and costly. Specifically, the risks included the possibility of crushing the fins and additional damage from bending the coil, which further required special equipment that was unavailable and cost prohibitive during the prototype stage. The project budget could not enable production of such a large coil and there was no guarantee a large prototype would survive the bending process to incorporate the unit into a full heat pump. A change in scope and target market was approved such that the SHX concept could be evaluated for a novel gas absorption heat pump water heater system, a household freezer, and a through-the-wall heat pump.

In the case of the gas absorption heat pump, the advanced SHX provided improved heat transfer leading to higher system performance, a reduction in weight, and added corrosion resistance as compared to a carbon-steel baseline HX.

For the residential freezer, testing revealed that the advanced SHX could achieve higher efficiency (2.6% less energy consumption) than a wire-on-tube condenser baseline. Energy efficiency was less than that measured for tube-fin and microchannel baselines, but still very competitive, especially considering a prototype was compared against mass-produced coils.

The prototype advanced SHX tested in the through-the-wall heat pump was originally designed for another application and was significantly smaller in terms of surface area. As would be expected given this condition, the advanced SHX case resulted in lower unit capacity and COP as compared to the baseline system. Regardless, test results demonstrate the SHX's ability to operate in this application and indicates potential for further optimization.

In parallel with system testing, work was done to: 1) evaluate the manufacturing concerns for mass producing the advanced SHX designs, 2) engaging in cost analysis, 3) evaluating potential market barriers and technology risks versus market opportunities, and 4) outlining a commercialization pathway. The proposed advanced SHXs are estimated to provide approximately 76% cost savings over

conventional copper RTPF HXs, the original baseline technology. Further, they are 16% and 19% lower in cost as compared to microchannel and aluminum RTPF HXs, respectively, alternate HX technologies also commonly found in HVAC&R equipment. Additional cost savings due to reduced maintenance and refrigerant charge could also be realized. Besides the potential for refrigerant leakage, a reduction in unit cost is the major benefit of the proposed advanced SHX.

Overall, the advanced SHX is an extremely promising technology. Development work has demonstrated that this concept can achieve comparable efficiency to baseline HXs for multiple applications and for a much lower cost.

1. Introduction

Refrigerant leakage has a significant impact on heating, ventilation, air conditioning and refrigeration (HVAC&R) industries in terms of both greenhouse gas (GHG) emissions and lost efficiency of the systems themselves. According to the Department of Energy (DOE), "energy consumption increase due to refrigerant leakage can be as high as 30 TBtu over a 10-year span for a single market segment" (Miljkovic et al, 2019). One of the major causes of refrigerant leakage is braze joints within a vapor compression system. The brazing process of the return-bends (U-bend) is often inconsistent and almost always imperfect. As a result, braze joints are left vulnerable to leaks.

Conventional tube-fin heat exchangers (HXs), as shown in Figure 1, are manufactured using multiple bent tubes, called hairpins, inserted through a stack of fins. The tubes are then either mechanically or pressure expanded such that the tubes and fins make a tight mechanical bond. Once expanded, the open tube ends are then brazed to either a U-bend or a manifold connecting tube (Figure 2). All joints shown on the right-hand side of Figure 2 are brazed. This results in one brazed joint per tube (Figure 3a).

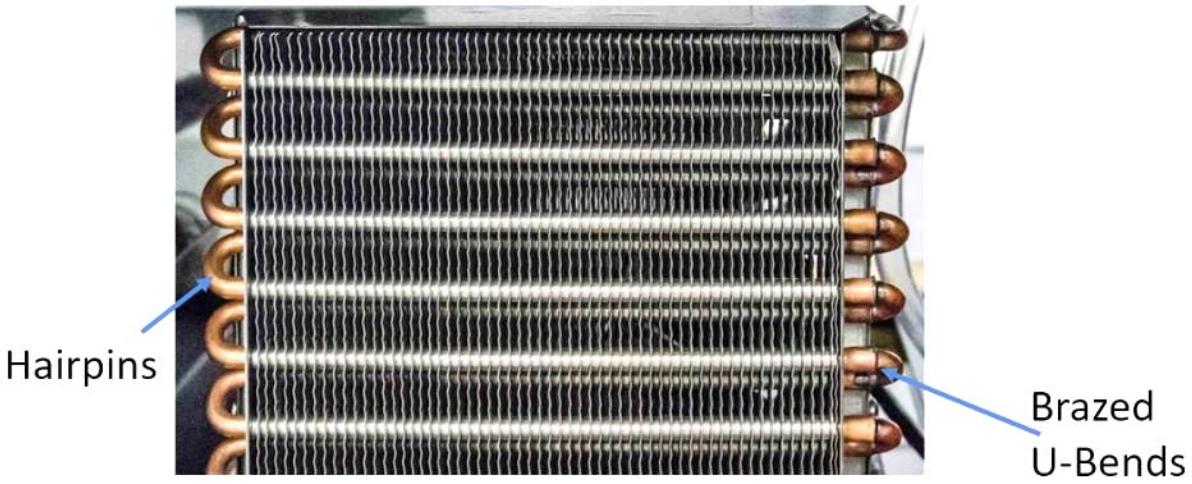

Figure 1: Conventional Tube-Fin Heat Exchanger

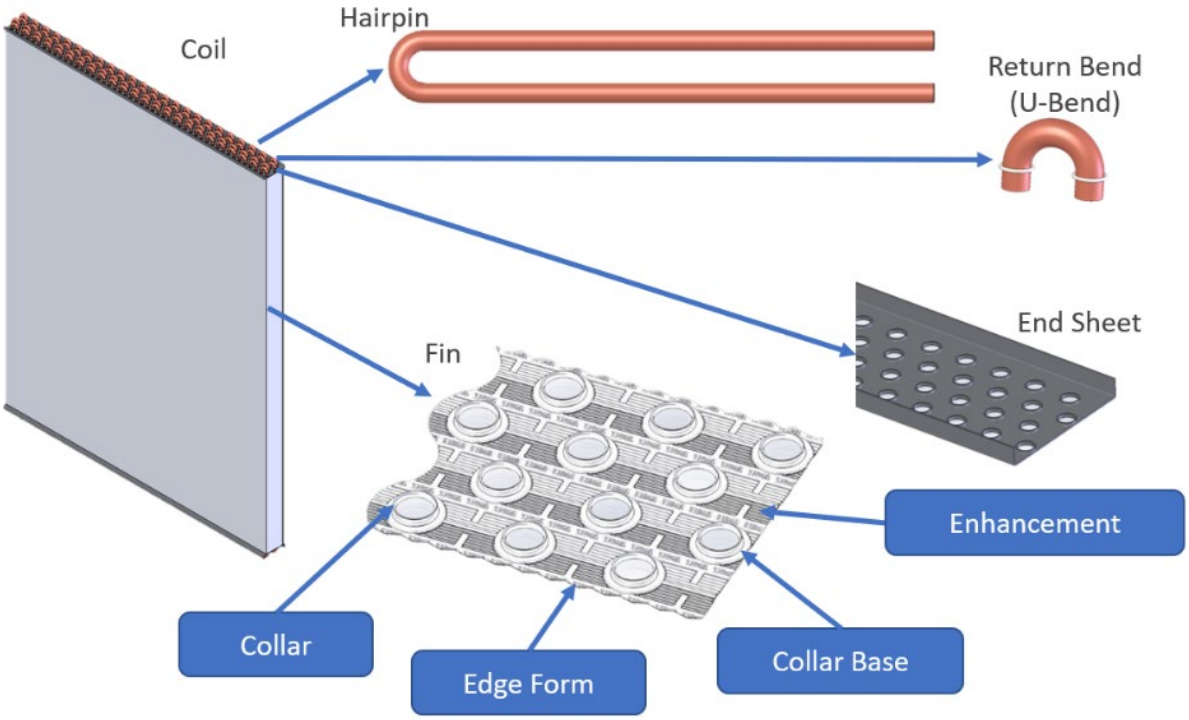

Figure 2: The Construction of a Conventional Tube-Fin Heat Exchanger

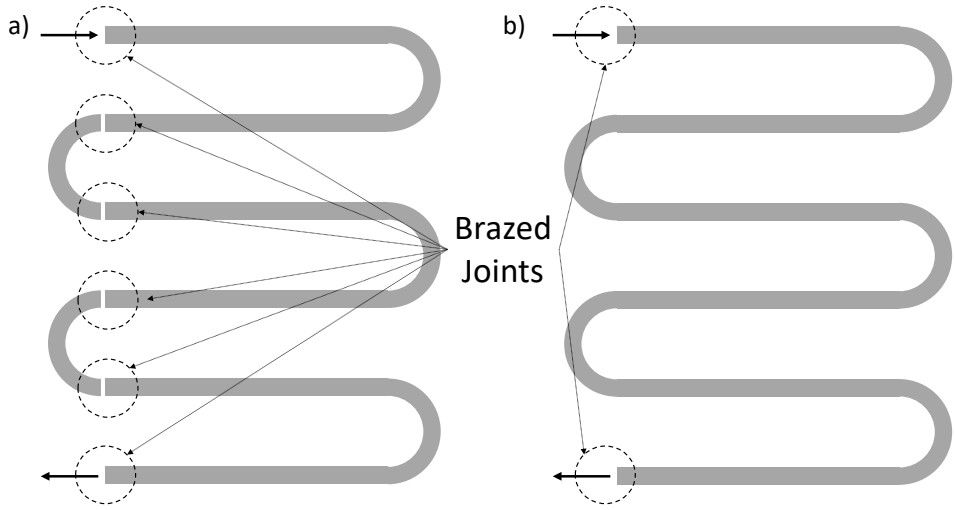

Figure 3: Heat Exchanger Tube Configuration for a) Conventional; b) Serpentine

An alternative to the conventional approach of using hairpins and U-bends is the use of a single continuous serpentine tube. Serpentine heat exchangers (SHXs), as depicted in Figure 4, unlike conventional tube-fin HXs, do not require braze joints to a U-bend or a manifold. Instead, the continuous tube is bent back and forth multiple times and is inserted into a fin pack that has an additional opening in the fin to allow

for the bent radius to enter. This open shape is often referred to as a "dog-bone" fin design given the shape it produces in the fin material. Because of this assembly method, SHXs do not require tube expansion, saving a manufacturing step as compared to their conventional counterparts.

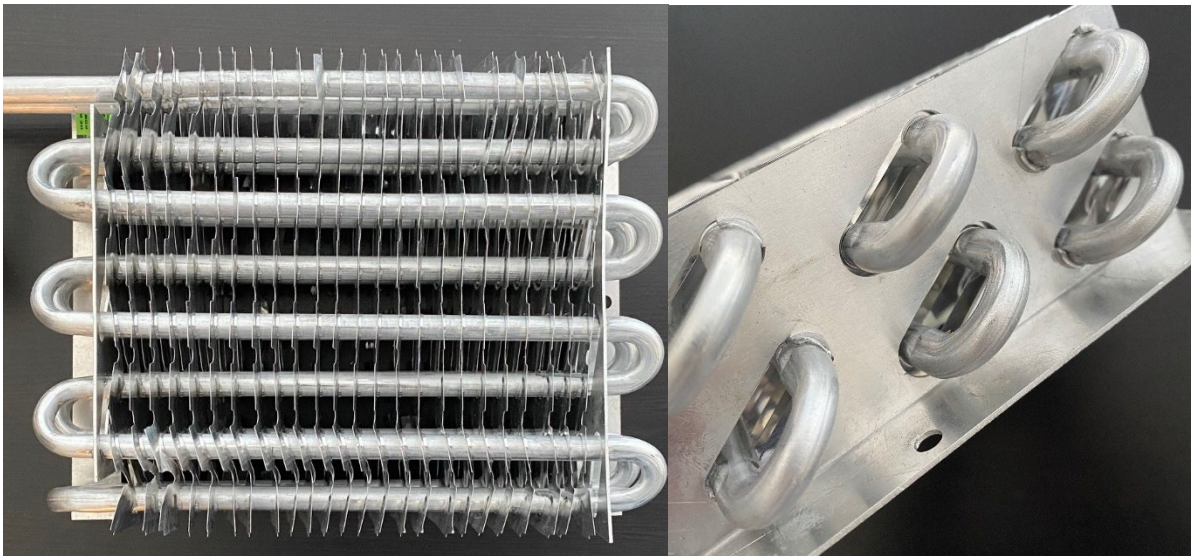

Figure 4: Example Serpentine Aluminum Heat Exchanger (Left) with "Dog-Bone" Fins (Right)

SHXs have only one inlet and one outlet, with a continuous tube connecting the two. Thus, their only brazed joints are to the inlet and outlet of the continuous serpentine tube. The total number of joints within a SHX is therefore proportional to the number of circuits by a factor of two (Figure 3b). The more tubes there are, the fewer brazed joints the serpentine heat exchanger has as compared to its conventional counterpart.

Serpentine HXs are currently widely used in small capacity refrigerators and coolers, such as those often found in supermarkets, as they are inexpensive, sturdy and remain reliable for long periods of operation. Furthermore, since they operate as evaporators, condensate or frost can fill voids between the fin and the tube, compensating for their poor tube-fin contact resistance relative to convention RTHXs. Current performance limitations, however, render them scarcely used for commercial and residential HVAC&R applications. As such, there is opportunity to improve on the existing SHX technology by improving the heat transfer to present a new HX solution that reduces the number of joints and continues to compete with conventional technology on the metrics of performance, cost, manufacturability, and durability.

This project investigated the potential for the use of novel SHX technology to minimize the number of joints in systems using conventional HXs. After establishing a baseline design, novel concepts were investigated for the dog-bone fin style, characteristic of SHXs. To account for lost fin surface area and to maximize effectiveness, fin enhancements were incorporated and, most crucially, fins and tubes were joined by brazing.

Once the design was established, it was integrated into multiple full-scale HX prototypes which were used to validate the concept as well as confirm manufacturability. Additional prototypes were then constructed and tested within the context of full systems. Three system applications were evaluated, all of which showed promising results for the ability of the proposed SHX to compete against its baseline tube-fin design.

As compared to conventional tube-fin HXs, the proposed SHX eliminates a significant majority of U-bend brazed joints, thus reducing refrigerant leakage, and competes with existing technology on a performance, cost and manufacturing basis.

1.1. Motivation

Refrigerant leakage plays an important role in energy consumption and global emissions. Residential and commercial air conditioning (AC) and heat pumping is expected to consume 4,522.8 trillion BTUs of energy in 2030, with residential AC systems alone accounting for 1,867.9 trillion BTUs (BTO Market Calculator). In addition, refrigerant leakage from HVAC&R equipment constitutes a small but significant source of GHG emissions due to their high global warming potential (GWP). In 2019, the EPA reported that HFCs in refrigeration and AC accounted for about 2.2.% of all GHG emissions in the US in 2017.

In addition to far-ranging environmental impacts, refrigerant leakage also has the potential for mild refrigerant poisoning (Fletcher, 2018). This can be a serious issue for homeowners, being hazardous to both personal health and the environment. The hydrofluorocarbons (HFC) in refrigerants can cause refrigerant poisoning, characterized by mild symptoms including irritation in eyes, ears, and the throat, nausea, vomiting, and headaches. More severe refrigerant poisoning can cause fluid buildup or bleeding in the lungs, burning sensations in the esophagus, and other more serious symptoms.

When leakage occurs and refrigerant is released, the total charge within the HVAC&R system is reduced. This has an additional negative impact by degrading system performance and increasing the systems associated energy consumption. If charge drops below 80-85% of the required value, the total cooling capacity can drop by as much as 17.7% (Goswami et all, 1997).

1.1.1. The Impacts of Brazing

According to Thurman and Scanlan (2007), welds and factory welds account for the greatest share of refrigerant leaks at 18.0%, as shown in Table 1. This classification is a misnomer as all joints in a copper- or aluminum-tube heat exchanger are brazed rather than welded. Therefore, it can be assumed that the "Welds/Factory Welds" category from this study either includes or directly refers to U-bend braze joints.

One strategy to reduce leaks in U-bend braze joints is by carefully controlling the temperature profile throughout the brazing process. In a study by Agba et al (1997), this was done by automatically adjusting process variables with a feedback control system. This approach significantly reduced the occurrence of heat exchanger leaks. The level of control employed in this study, however, is simply not accessible in industry. With torch brazing, temperature control is very difficult to implement due to the very high heat rate using required. In furnace brazing, the temperature control is very accurate but not extremely fast. "Autobrazers are normally operated by manually adjusting process variables with no automatic feedback of input variables" (Agba et al 1997). For example, the Dragon 15/20 Brazing Robot, a fully automated induction heating braze machine, is "programmed to move to each joint and apply power for a preprogrammed amount of time" (Dragon 15/20- Induction Brazing Robot, 2021). A preprogrammed amount of time at each joint leads to a much higher occurrence of leaks than with a feedback control system, yet such approach is accepted as industry standard.

Another strategy to improve U-bend braze joints is by reducing the time to complete a braze. Brazing must be done as quickly as possible to reduce annealing and subsequent grain growth in the base metal. "This allows the tube to retain more of the work-hardened strength imparted from swaging" (McCracken, 1998). One way to reduce brazing time is through induction heating (such as with the Dragon 15/20), which brazes about three times faster than an acetylene torch. Theoretically, zero braze time is needed to eliminate all grain growth in the base metal. Even the few

seconds taken to braze by induction heating reduces the strength of the base metal around the joint and creates the potential for leaks.

Additionally, a balance must be struck between temperature profile control and brazing as quickly as possible. This is because there is little margin for error between the activation temperature of a brazing material and the melting point of a base metal. If the temperature of the joint is too high during brazing, then the base metal will "burn through," creating holes from which refrigerant can leak. If the temperature is too low, then cold spots occur and the brazing material does not penetrate deep enough into the joint, increasing the potential for cracking and leaks (Somani, 2017). As an example of a standard brazing temperature range, Al 3003 (common in residential heat exchangers) has a melting point of 646°C and is commonly brazed with an Al-Si alloy with an activation temperature of 575°C.

Table 1: Refrigerant Leakage Causes / Sources (Thurman and Scanlan, 2007)

Cause	% frequency
Welds / Factory Welds	18.0
Caps / Cores	9.9
Packing	9.9
Flares	9.4
Evaporators	9.3
Gaskets	9.0
Levels / Top Off from Previous Repair	8.9
Vandalism / Other	5.7
Vibrations	5.3
Controls	4.6
Deterioration	4.0
Condensers	3.5
Compressor Change	1.6
Refrigerant Conversions	1.0
Heat Reclaim Tanks and Coils	0.8

Moreover, whenever separate tubes are joined by swaging, there is a possibility of a fitting defect. A fitting defect significantly increases the chances of a leak regardless of the technique employed during the subsequent braze.

To understand the susceptibility of U-bends or tube-to-tube braze joints, a joint study between the Air Conditioning and Refrigeration Institute[1] (ARI) and Copper Development Association (CDA) was conducted in 1997. Results showed that braze joints performed worse than straight tubing during cyclic vibration and pressure tests (McCracken 1997). Vibration fatigue tests were conducted to simulate handling damage and routine cyclic stress. Vibration caused braze joints to fail more quickly than straight tubing for two reasons. First, braze joints with poor penetration failed rapidly from cracking within the braze filler material even when the joint appeared to be sound and withstood pressure testing. Second, there is always a higher stress concentration at the fillet of the braze joint, this stress concentration becoming even greater the when the fillet radius is less than intended due to various manufacturing difficulties.

During high stress, short duration pressure fatigue testing, nearly every braze join sample failed. Samples would either fail at poor penetration joints or mechanical deficiencies at braze joints. The imperfections of braze joints were exposed during vibration and pressure testing, further demonstrating how braze joints present significant possibilities for leaks.

Ultimately, careful control of the brazing process is required to reduce the possibility of leaks. Temperature profile, brazing speed, tube fitting, joint penetration, fillet radius, and material selection must all be properly assessed to achieve the best braze joint possible. Even with extremely rigorous and exhausting manufacturing standards, braze joints are still weaker and more susceptible to leaks than straight tubing. The best way to reduce the probability of a leak is to reduce the number of braze joints altogether.

1.1.2. Potential of the Advanced Serpentine Heat Exchanger

Significantly reducing the number of joints in a system would, by definition, reduce the potential for leakage. Utilizing serpentine aluminum tubes in a HX, as opposed to a conventional round tube plate fin (RTPF) coil, has the potential to eliminate between 70% and 100% of joints in the HX, depending on coil type, size, and pressure drop allowances. This is achieved by significantly reducing the number of U-bend joints requiring brazing.

[1] In 2007, the Air Conditioning and Refrigeration Institute changed its name to the Air Conditioning, Heating and Refrigeration Institute (AHRI)

The potential for joint reduction is illustrated by considering a SHX of equivalent capacity as a conventional residential two-ton evaporator. A "standard" HVAC RTPF HX would have 132 brazed joints in the U-bends while an equivalent SHX made out of 3 sections would have only 19 joints, thereby eliminating 85% of all joints required. Joint reduction is even greater in refrigeration applications. A household refrigerator condenser replaced with a SHX has the potential of eliminating 100% of the joints, other than the inlet and outlet.

In addition to the significant potential in brazed joint reduction, and consequential refrigerant leakage, SHXs also possess several other advantages including:

- **No need to make U-bends nor braze them, thus eliminating additional manufacturing steps;**
- **Elimination of the tube expansion process, saving a manufacturing step, but also allowing for inner grooved tubes to remain undamaged, ultimately improving tube efficiency and overall heat transfer performance; and,**
- **Simple construction, with a one-step-brazing process to a complete finished product.**

These advantages offer direct manufacturing cost-saving potential. The proposed advanced SHXs are estimated to provide approximately a 76% cost savings over conventional copper RTPF HXs. They are further 16% and 19% lower in cost as compared to microchannel and aluminum RTPF HXs, respectively. Additional savings due to reduced maintenance and refrigerant charge could also be realized.

1.2. Target Market

The initial target market for the project was residential and light commercial HVAC, particularly targeting small capacity (1-3 ton) air conditioners and heat pumps. In 2020 alone, there were more than 9.3 million AC and HP purchases across the US (AHRI, 2020). Cooling-only sales were 5.9 million. Total sales were up approximately 10.1% over 2019 values and 36% over 2015 values with the expectation that they will continue to rise (AHRI, 2015). As of June 2021, the sales of ACs and air-sourced HPs has increased by 19.1% as compared to 2020 levels (AHRI, 2021). As reported in 2015, 87% of homes (100 million) in the US currently have an AC or HP system (EIA, 2015).

Designing for a residential AC or heat pump system, however, even if only on the order of 1.5 or 2-tons, still requires production of a relatively large condenser coil which is often bent in a "U" or "D" shape to achieve a small installed footprint. As is

described later in this report, several prototype challenges were identified that drove the team to explore additional target markets. In addition to ACs and HPs, domestic refrigerators and low- to medium-temperature reach-in freezers and refrigerators were identified as a viable market, primarily given their existing acceptance of conventional serpentine HXs. Adopting a new serpentine heat exchanger is not a large risk in these refrigeration markets and can provide for cost savings as well as the potential for leakage reduction.

Heat pump water heaters (HPWHs) were also identified as a suitable application given that the heat exchangers used are relatively small and the HPWH market is growing in popularity. Small system AC, such as window units and packaged terminal air conditioners (PTACs) and heat pumps (PTHPs) appear to be more viable, having relatively smaller HXs that are typically limited to a single, straight slab. These markets are the focus of the initial commercialization effort with refrigeration systems taking priority.

Each type of equipment within the HVAC&R industry has its own expected leak rate as shown in Table 2. Implementing the advanced SHX into any one of these markets would help to reduce leakage potential. As such, collaboration with additional project partners explored the potential use of the proposed SHX solution for an ammonia (NH_3)-based gas absorption heat pump water heater evaporator and a household freezer condenser. More detail on the market assessment and viability is outlined separately in the project commercialization report.

Table 2: Leak Rate by HVAC System Type (Goetzler, et al., 2015)

Equipment Category	Estimated Annual HFC Leakage Rates
Supermarkets and Other Retail	1-25%
Mobile Air Conditioners	2-18%
Cold Storage	15%
Residential Unitary AC	12%
Industrial Process Refrigeration	4-12%
Centrifugal Chillers	2-11%
Commercial Unitary AC	8-9%
Packaged Terminal AC / HP	4%

Refrigerated Appliances	1%

2. Goals and Objectives

The goal of this project was to develop prototype SHXs that use surface enhancements to achieve equivalent or better performance than current state-of-the-art air conditioning tube-fin HXs while reducing the potential for leakage. The design of optimized fin surfaces, aptness of fin-to-tube joining techniques, and development of tooling and manufacturing techniques were critical to achieve success in this project.

The original performance targets compared to a current state-of-the-art tube-fin heat exchanger were as follows:

1. Equal or greater air-side heat transfer.
2. Equal or lower air-side pressure drop.
3. Equal or lower heat exchanger cost.
4. Elimination of at least 90% of the joints

Upon initial analysis, as detailed in the Baseline Analysis section, the 90% joint elimination was reevaluated and determined to be prohibitive due to the refrigerant pressure drop and resultant number of circuits. With those performance constraints, the objectives were modified to an 85% reduction for the indoor coil, and 70% reduction for the outdoor coil. All other objectives remained the same.

The resulting HX designs could be mass produced to significantly reduce the direct and indirect impacts of refrigerant leakage in HVAC&R systems.

3. Project Summary and Major Accomplishments

The original plan for this project cast it as a three-year endeavor from October 2016 to October 2019. A no-cost extension was granted in May 2019 to extend the project through September 2021. The project was divided into three budget periods (BPs):

- BP1: October 2016 to August 2017 – Design through Simulation and Benchtop Testing
- BP2: August 2017 to December 2018 – Heat Exchanger Prototype Development

- **BP3: December 2018 to September 2021 – System Implementation and Commercialization**

Analysis conducted in BP1 focused on the use of computational fluid dynamics (CFD) and CoilDesigner®, a proprietary air-to-refrigerant heat exchanger design and simulation tool. Initial CFD simulations focused on establishing and analyzing the baseline, resulting in modifying the original 90% joint elimination target to 85% and 70% for indoor and outdoor coils respectively. Further simulations then focused on fin design, particularly different types of fin enhancements. An initial fin design emerged with a vertical dog-bone cut and sets of louvers on the top and bottom. With an initial concept established, a thorough optimization was conducted to refine the design. To address refrigerant side pressure drop concerns while still achieving joint reduction goals, a novel split-merge joint was developed and incorporated into the HX circuitry. The split-merge joint reduced both the pressure drop penalty and the number of joints in the system by combining feeding and discharging streams into one unified joint. Benchtop tests focused on the ability to braze the serpentine tubes to the newly optimized enhanced fins and the viability of the split merge joint itself. These processes were verified by microsection analysis and deemed ready to apply to full-scale HX prototypes.

Full HX prototype designs using the brazing methods, fin designs, and split-merge joint circuitry were rigorously optimized in preparation for prototyping in BP2. Final designs were then constructed with the support of project partners and vendors. Four prototypes were constructed with a full-cross counter flow design and straight serpentines. After construction, each prototype underwent performance testing in a temperature-controlled wind tunnel, while finite element analysis (FEA) and mechanical tests were conducted on sample individual split-merge joints. Only one prototype underwent accelerated life tests (ALT) to predict its real-time cyclic life. The most successful prototype had less than 1% non-brazed fins and a modified split-merge joint design.

Finally, once the HX concept had been proven, the project shifted focus to implementation within a full system. While the SHX design for a residential heat pump was promising, prototyping a full-size SHX and then bending it as would be typical to include in a residential condensing unit would be too risky and costly an application. As noted above, a change in scope and target market was approved such that the SHX concept could be evaluated for a novel heat pump system and a

household refrigerator. Simultaneously, work was done to evaluate the manufacturing concerns for mass producing these SHX designs, engaging in cost analysis, evaluating potential market barriers and technology risks up against market opportunities, and ultimately outlining a commercialization pathway. The results of all stages of work are described herein.

4. Establishing the Baseline

Prior to any novel HX technology development, a baseline was chosen to act as a comparative standard for the SHX designs. This baseline was based on the highest sales volume residential/light-commercial AC or heat pump system with a capacity of 1-5 tons, using R410A, with technical specifications provided by project partner United Technologies Research Center (UTRC). The high-level dimensions shown in Table 3 match a rated 2.5-ton system already in possession at the OTS lab (Figure 5), whose indoor and outdoor units served as the baseline HXs.

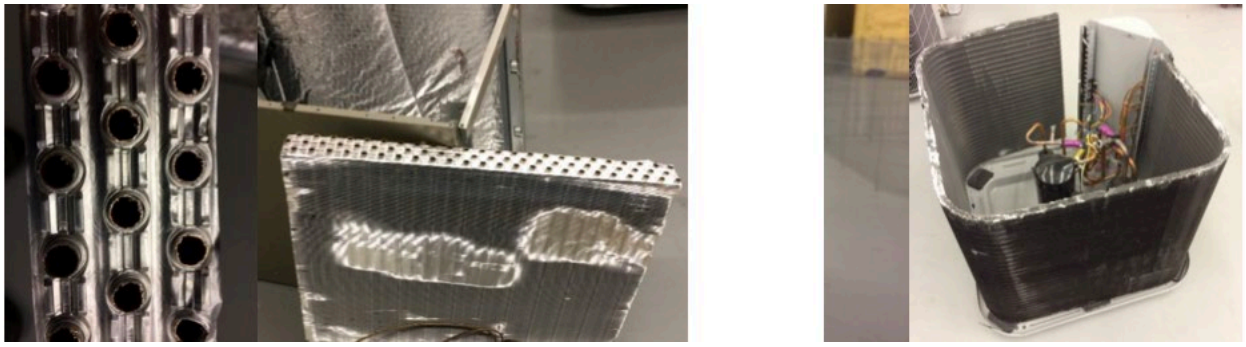

Figure 5: Baseline Heat Exchangers for a 2.5-ton heat pump; a) Indoor b) Outdoor

Table 3: Baseline AC/HP System (UTRC) Requirements

Parameter	Value
Indoor unit model number	FB4CNO036L
Outdoor unit model number	CH14NB036*0**B*
Rated cooling / heating capacity	33,000 / 33,800
SEER/HSPF	14/8.2
Refrigerant charge	7.60 lbm (15ft line sets)
Outdoor HX tube diameter	7mm (0.291" expanded OD)
Outdoor HX # tubes	28
Outdoor HX fin type	Lanced
Outdoor HX fin pattern and geometry details*	0.85" X 0.736"
Outdoor HX air flow rate	3167 CFM
Indoor HX tube diameter	3/8" (0.396" expanded OD)
Indoor HX # tubes	24
Indoor HX fin type	Lanced
Indoor HX fin pattern and geometry details*	1" X 0.75"
Indoor HX air flow rate	1200 SCFM
Compressor model number	APG031KA

4.1. Baseline Analysis

Baseline models for the HX designs presented in Table 3 were developed using CoilDesigner®. A full system model of the baseline heat pump system was developed using VapCyc®. CoilDesigner® is a coil simulation software developed by the Center for Environmental Energy Engineering (CEEE) at the University of Maryland (UMD) and originally released in 2002, which enables modeling different types of heat exchangers, performance evaluation, and highly customizable analysis. VapCyc® is an advanced vapor compression cycle and simulation tool, also developed by CEEE, used to evaluate components on a system-level. The assumptions for the baseline simulations are presented in Table 4, with the results in Table 5 and Table 6.

Table 4: Baseline Simulation Assumptions

Metric	Unit	Indoor		Outdoor	
		Specification	Used	Specification	Used
Airflow rate	m^3/s	0.564	0.564	1.489	1.489
Air inlet temperature	K	N/A	300	N/A	308.15
Air inlet RH	%		50		50
Superheating	K	N/A	4	N/A	N/A
Sub-cooling	K		N/A		5.5

Table 5: Baseline System Simulation Results, VapCyc®

Metric	Unit	Indoor	Outdoor
Capacity	kW	10.585	12.901
	Ton	3.010	3.668
Inlet Pressure (Ref.)	kPa	1083	2864
Inlet Temp. (Ref.)	K	283.002	345.694
Inlet Quality (Ref.)	-	0.248	-
Ref. flow rate	g/s	0.06591	
Ref. ΔP	kPa	18	25
Air h	$W/m^2.K$	99.97[2]	108.15[3]
Air ΔP	Pa	61.22[1]	12.12[2]

Table 6: Baseline HX Performance Testing Results, CoilDesigner®

Metric	Unit	Baseline	
		Indoor HX	Outdoor HX
Q	kW	10.24	12.96
AFR	m^3/s	0.564	1.48
	cfm	1200	3149
u	m/s	2.14	1.02
MFR	g/s	63.8	63.8
P	kPa	1150	2700
T_{in}	K	285	350
x_{in}	-	0.228	-
ΔP_{air}	Pa	45.8[1]	12.2[2]
h_{air}	$W/m^2.K$	101.3[1]	108.1[2]
η_o	-	0.81	0.76
UA_{air}	W/K	1383	3487
ΔP_{ref}	kPa	14.9	29.3

[2] *Wang, et al., 2001*
[3] *Wang, et al., 1999*

One of the earliest analyses done was a reality check as to whether the 90% joint reduction goal was feasible. In the study, the baseline HXs were used only altering the number of circuits, keeping the same number of tube banks and rows, but changing their connections to adjust the number of circuits. The indoor and outdoor coils had, respectively, 4 circuits (72 joints) and 5 circuits (28 joints) (Figure 6a). In order to achieve a 90% joint reduction with a SHX, the baseline indoor coil could only have up to 3 circuits, and for the outdoor coil, a single circuit only. Such a circuit arrangement, however, proved to have detrimentally high refrigerant side pressure drop. As can be seen in (Figure 6b), with a 90% joint reduction, the pressure drop increases by a factor of 2. For the outdoor unit, the mass flux would increase by a factor of 5, while the refrigerant pressure drop would potentially increase by a factor of 25 (ΔP α ~ṁ"²).

Based on these findings, the original project objectives were modified to at least an *85%* joint reduction for the indoor coil, and a *70%* joint reduction for the outdoor coil (Figure 6a).

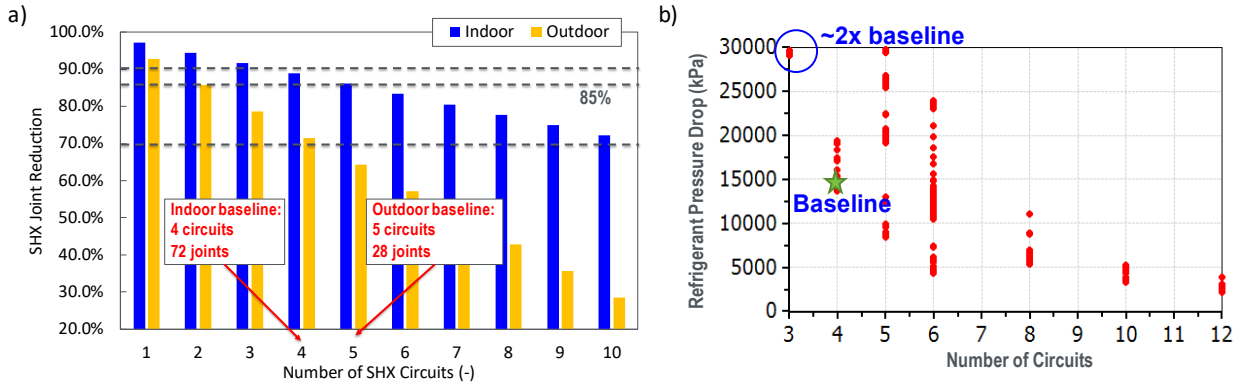

Figure 6: a) Joint Reduction vs Number of Circuits; b) Pressure Drop vs Number of Circuits

In addition to modeling in CoilDesigner®, the fin design used for the baseline heat pump HXs was modeled using CFD, as depicted in Figure 7. All initial CFD simulations were made using the Star CCM+ platform. The team later migrated to ANSYS v18.0 in late 2017, so the majority of CFD analyses conducted throughout the project used the latter. Details on the general CFD modeling approach and settings used are outlined in Appendix A: CFD Settings.

CFD model and simulation results for the actual baseline HXs are presented in Table 7. The purpose was to verify the CFD model against the correlations used in the CoilDesigner® files for the airside thermal-hydraulic characteristics prediction.

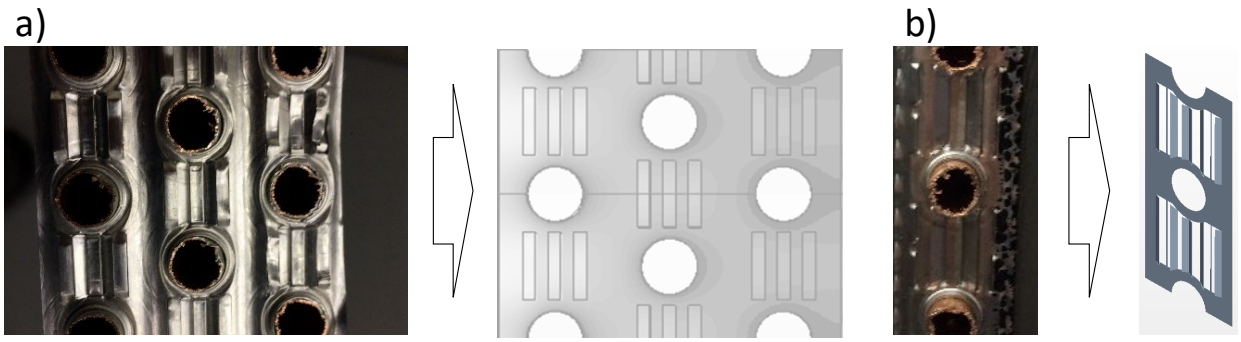

Figure 7: Fin models of baseline HX's: a) indoor coil; b) outdoor coil

The simulations were carried out with constant tube wall temperature. The data reduction for heat transfer coefficient was obtained using the UA-LMTD method (equations 1 and 2), while the heat transfer coefficient and fin effectiveness were iteratively solved using the conventional Schmidt method (1949) (Schmidt, 1949) (equation 3).

$$\dot{Q} = \dot{m} \cdot c_p \cdot \Delta T_{air} = \eta_o h \cdot A_o \cdot \Delta T_{ml} \quad (1)$$

$$\eta_o h = \frac{\dot{m} \cdot c_p}{A_o} \cdot \frac{\Delta T_{air}}{\Delta T_{ml}} = \frac{\dot{m} \cdot c_p}{A_o} \cdot \ln\left[\frac{T_w - T_i}{T_w - T_o}\right] \quad (2)$$

$$\eta_o = 1 - \frac{A_f}{A_o}(1-\eta), \eta = \frac{\tanh\left(0.5 m D_o \cdot h\right)}{\left(0.5 m D_o \cdot h\right)}, m = \left(\frac{2h}{k \cdot \delta}\right)^{0.5} \rightarrow \underbrace{h \leftrightarrow \eta_o}_{\text{Iteratively}} \quad (3)$$

The temperature profiles are shown in Figure 8; the CFD results showed good agreement with existing empirical correlations in terms of heat transfer coefficient (Table 7). The CFD pressure drop predictions had higher discrepancies where the indoor coil resulted in twice as much pressure drop as compared to the correlation. For the outdoor coil, the discrepancy was smaller (15%), and within the correlation uncertainty. The thermal performance agreed well, and the impact on the CoilDesigner® models using the CFD results was negligible. The results gave confidence in the CFD models, at least on the thermal perspective.

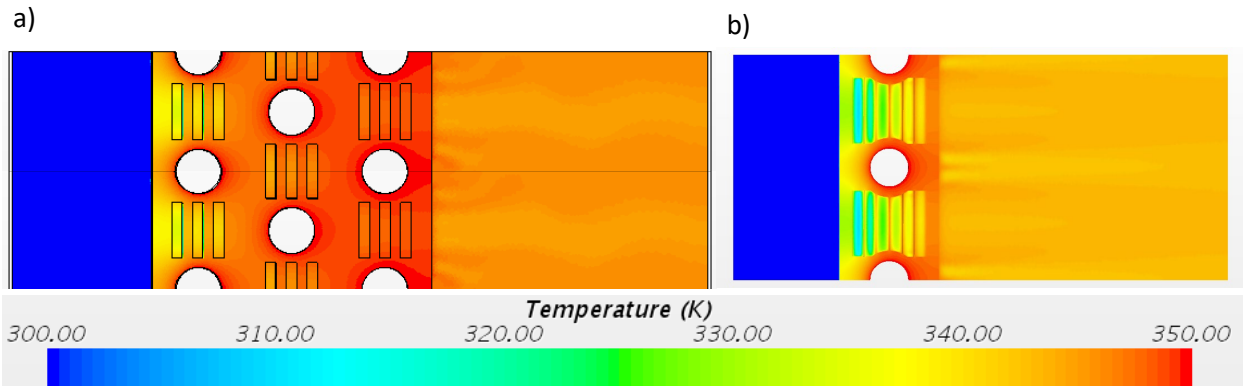

Figure 8: Temperature contour plots for the baseline HX's CFD model

Table 7: CFD vs. Correlations

HX	Indoor			Outdoor		
Metric	**Correlation**	**CFD**	**Rel. Diff**	**Correlation**	**CFD**	**Rel. Diff**
η_o*h (W/m².K)	82.05	80.18	-2.28%	82.24	79.2	-3.64%
η_o (Schmidt)	0.81	0.74	-9.01%	0.76	0.75	-0.53%
h (W/m².K)	101.3	108.8	7.39%	108.1	105.1	-3.12%
ΔP (Pa)	45.8	89.1	**94.5%**	12.2	14.1	**15.2%**

4.2. Dog-bone Fin Analysis for Baseline Designs

Following the initial round of baseline analysis, both the indoor and outdoor fins received modified fin designs. Modified fin designs (Figure 9) with dog-bone cuts were used for the baseline HX's that had enough airside conductance to maintain similar performance when compared to the original designs. For this study, the tube dimensions, configurations and circuits were kept constant while the fins were modified. For the indoor coil, the fin spacing was increased from the original 16 FPI.

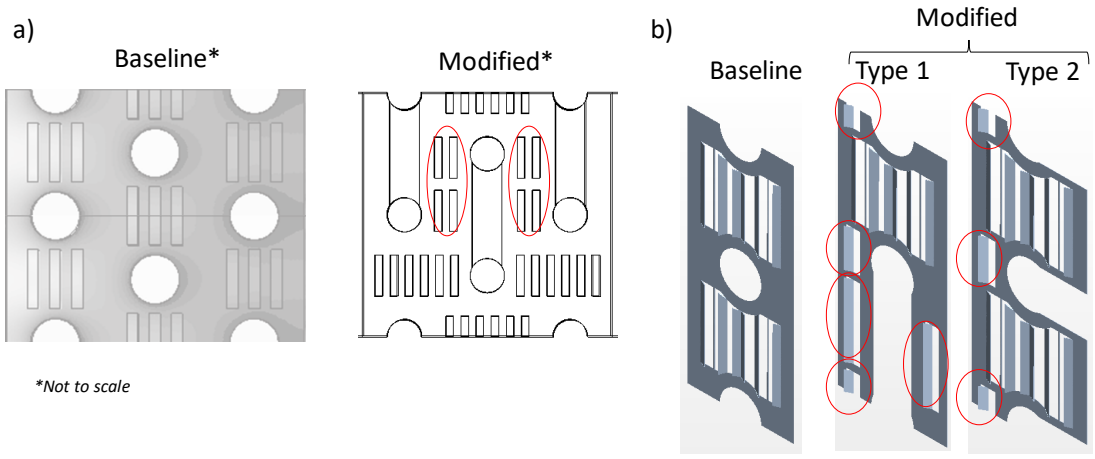

Figure 9: Modified baseline fin designs: a) indoor coil; b) outdoor coil.

The indoor coil fin with the vertical dog-bone cuts was modified so that six slits were placed in between the tubes, as opposed to only three used in the baseline, and four additional slits were added between the cut and tubes (Figure 9a). The baseline outdoor coil fin considered two modifications: Type I, with a vertical dog-bone cut, and Type II, with a horizontal dog-bone cut. For both, additional louvers were added near the leading edge of the fin (Figure 9b).

The three concepts in Figure 9 were modeled and simulated in CFD (Figure 10). The post-processed data was used to modify the HX models within CoilDesigner® and evaluate the overall HX performance (Table 8). The results showed that the modified designs, despite the loss of surface area, still achieved the baseline HXs capacity within less than 7%.

The modified airside indoor heat transfer coefficient was proven to be even higher than the baseline by 12% (Table 8), with a surplus that compensated for the area reduction. Additionally, the joint reduction would have been 89% if four circuits had been maintained.

The modified outdoor fins did not show as much improvement as the indoor fin, though the HX performance did adequately improve. However, the joint reduction was only 64%, rather than the desired 70%, since the number of circuits was kept constant and equal to 5. A supplemental analysis was conducted to evaluate the tradeoff if the number of circuits was reduced from 5 to 4, i.e., achieving the 70% joint reduction target. In this scenario, while capacity was still met and material

savings were realized, the refrigerant pressure drop was prohibitive, increasing by more than 100% over the baseline.

A similar outcome was observed for the indoor HX (Figure 6) when reducing the number of circuits from 4 to 3. Considering that the airside performance of the modified fins exhibited promising results, the potential for improvement was realized during the optimization phase of the project. That more in-depth analysis enabled close inspection of the trade-offs for the outdoor coil and identified whether a compromise was identified that will achieve acceptable pressure drop with the targeted joint reduction.

The data reduction for these modified fin designs used the Schmidt Method. This method, however, would have been accurate if the tube and fin had full contact on the tube perimeter. These new designs had a third less contact area, which meant the gradient temperature in the fins was higher. This was observed at the fins trailing edges; the fin temperature profiles depicted in Figure 10 shows much higher gradient than in Figure 8.

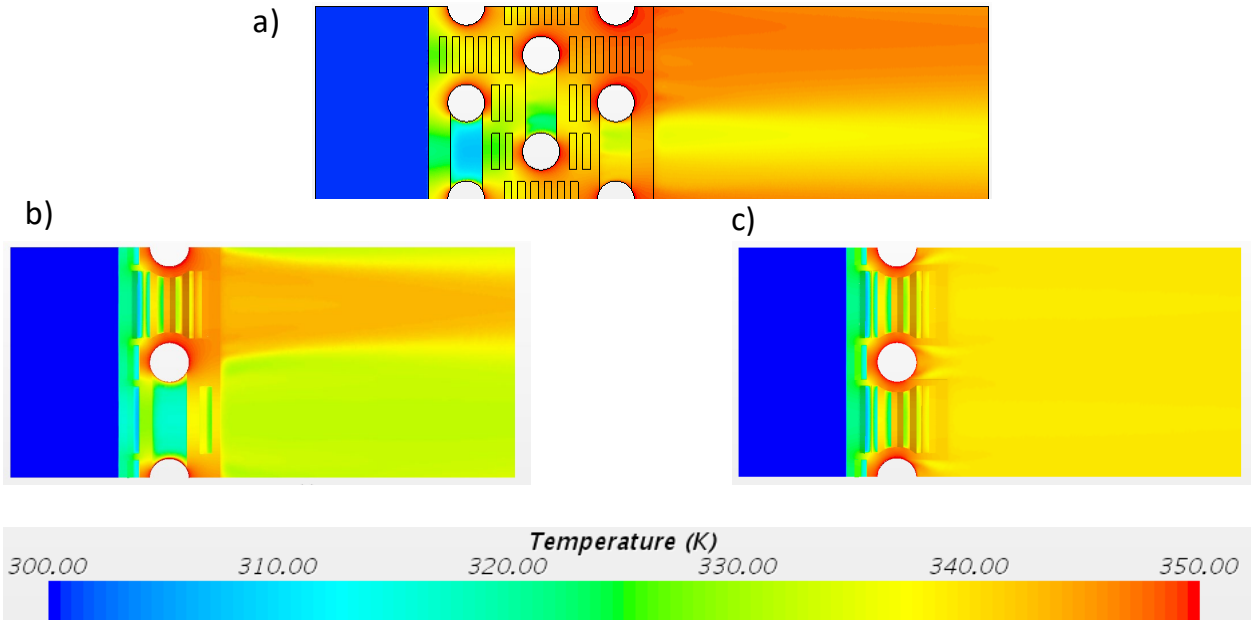

Figure 10: Temperature contour plots for modified fin designs: a) indoor HC; b) outdoor HX Type I; c) outdoor HX Type II

Table 8: Modified Baseline Indoor HX Overall Performance.

Metric	Unit	Indoor HX		
		Baseline	Modified	Rel Diff

D_o	m	0.0098	0.0098	0.00%
P_l	m	0.0190	0.0198	4.21%
P_t	m	0.0254	0.0254	0.00%
S_d	m	0.0229	0.0235	2.93%
FPI	m	16	16	0.00%
N_{banks}	-	3	3	0.00%
N_{rows}	-	24	24	0.00%
$N_{circuits}$	-	4	4	0.00%
Face area	m^2	0.26	0.26	0.00%
Joints	-	72	8	-88.89%
h_{air}	$W/m^2.K$	101.1[4]	113.3[5]	12.07%
A_o	m^2	16.85	14.24	-15.47%
ΔP_{air}	Pa	45.82[3]	49.69[4]	8.45%
Q	kW	10.40	10.20	-1.58%

Table 9: Modified Baseline Outdoor HX Overall Performance.

Metric	Unit	Outdoor HX				
		Baseline	Modified (Type I)	Rel Diff	Modified (Type II)	Rel Diff
D_o	m	0.00737	0.00737	0.00%	0.00737	0.00%
P_l	m	0.019	0.019	0.00%	0.019	0.00%
P_t	m	0.0217	0.0217	0.00%	0.0217	0.00%
S_d	m	N/A	N/A	N/A	N/A	N/A
FPI	m	21	21	0.00%	21	0.00%
N_{banks}	-	1	1	0.00%	1	0.00%
N_{rows}	-	28	28	0.00%	28	0.00%
$N_{circuits}$	-	5	5	0.00%	5	0.00%
Face area	m^2	1.46	1.46	0.00%	1.46	0.00%
Joints	-	28	10	-64.29%	10	-64.29%
h_{air}	$W/m^2.K$	108.5[6]	82.1[7]	-24.33%	91.3[6]	-15.85%
A_o	m^2	42.40	37.02	-12.70%	35.91	-15.30%
ΔP_{air}	Pa	12.20[5]	11.60[6]	-4.92%	14.20[6]	16.39%
Q	kW	12.90	12.00	-6.98%	12.30	-4.65%

The product of fin effectiveness and heat transfer coefficient remained unaltered (equation 4), validating the analysis. The actual values for the heat transfer coefficient in Table 7 were inaccurate for this very reason; i.e. the actual heat transfer coefficients should have been much higher while the fin effectiveness

[4] Correlation
[5] CFD + Schmidt Method
[6] Correlation
[7] CFD + Schmidt Method

should have been much lower than predicted by the Schmidt method. This insight lead to an additional analysis to evaluate the actual heat transfer coefficients and fin effectiveness of these dog-bone fins and discuss the importance of fin-tube contact.

$$h_{Actual} = h_{Schmidt} \cdot \alpha, \eta_{o,Actual} = \eta_{o,Schmidt} / \alpha \Leftrightarrow (\eta_o h)_{Actual} = (\eta_o h)_{Schmidt} = (\eta_o h)_{CFD} \quad (4)$$

Although the modified fins led to an indoor airside heat transfer coefficient higher than the baseline by about 12% (Table 8), as well as an increased outdoor airside heat transfer coefficient, the temperature profiles had a much larger gradient than the baseline, and the modified fin designs did little to alleviate the pressure drop. The indoor HX with the modified fin design achieved an 89% joint reduction, while the outdoor baseline could either achieve a 64% joint reduction with 5 circuits, or a 70% joint reduction with 4 circuits, but with a prohibitive pressure drop. While analysis results fell short of project targets, they were close enough to the targets to suggest that a full optimization would find a solution capable of achieving the desired heat transfer performance.

5. Enhanced Serpentine Heat Exchanger Design

After establishing the baseline condition and understanding the potential improvement without any optimization, focus was shifted to evaluating additional fin designs and preparing for a full SHX prototype. Work was conducted in two key stages: 1) computational analysis, extending from the initial baseline assessments; and 2) benchtop testing, in which the focus was primarily on material selection for the tubes and fins as well as the HX joining methods.

5.1. Fin Design and Optimization

5.1.1. Fin Analysis Accuracy Assessment

Following the initial CFD analysis conducted for the baseline configurations, further work was conducted to assess the accuracy of the methods and assumptions used for analysis. In this subsequent work, the actual values for heat transfer coefficient and fin effectiveness were evaluated using CFD simulations. Unlike the previous CFD simulation, where the fin wall had a temperature gradient (Figure 11a), the models were simulated again with the fin wall at constant temperature and equal to the tube wall (Figure 11b). If there is no temperature gradient in the fin wall, the fin efficiency is equal to unity and so is the fin effectiveness. Therefore, the heat

transfer coefficient was readily extracted from this simulation. The actual fin effectiveness was obtained by comparing the two simulations (equation 5).

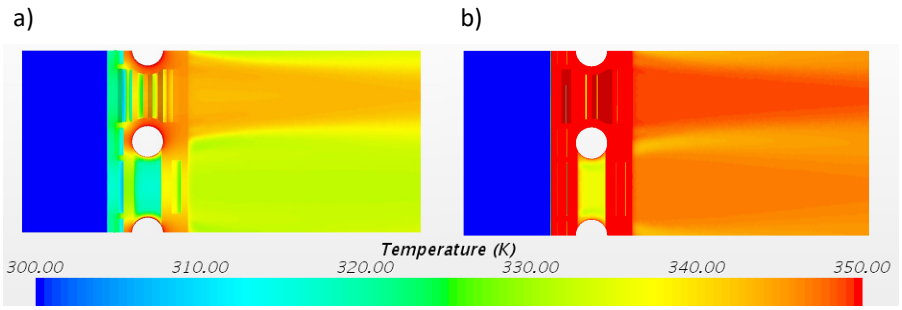

Figure 11: Fin temperature: a) Gradient; b) Constant.

$$\eta_{o,Actual} = \frac{(\eta_o h)_{fin\nabla T}}{(\eta_o h)_{finT_w}} = \frac{(\eta_o h)_{fin\nabla T}}{1.0 \cdot h_{Actual}} \quad \textbf{(5)}$$

Prior research of non-brazed (mechanical joint) serpentine tubes and dog-bone fins verified that the actual fin effectiveness is 30-35% lower than it would be for a conventional collared fin surrounding the whole perimeter of the tube. ElSherbini et al. (ElSherbini, et al., 2003) conducted an experimental investigation of contact resistance of collarless evaporators, i.e., serpentine heat exchangers with a half dog-bone cut. In their work, they compared a conventional collared fin brazed to the tube and the non-brazed serpentine version, under dry and frosting conditions. They reduced the data such that the airside resistance and the contact resistance were grouped into a single value, whereas tube wall and refrigerant resistances could be isolated and accurately determined.

Their findings showed that, under dry conditions, the air and contact resistance was twice as high in the non-brazed coil. The latter suggests that, if the brazed coil has ideal zero contact resistance, the non-brazed contact resistance is approximately the same value as the airside or, at least, the same order of magnitude. Furthermore, their results under frosting conditions did not follow the same pattern; instead, the non-brazed coil exhibited similar air and contact resistance of its brazed counterpart. This suggests that the layer of frost possibly filled existing gaps between the tube and the fin allowing better conduction to occur. This finding is important to the proposed design and implies the need and potential for improved performance with a brazed connection between the tube and fin.

The results for early-stage fin effectiveness analysis for the proposed design (Table 10) showed that using the Schmidt method only deviated by 6.9% for the baseline fin effectiveness, however, for the modified fins, the deviation was above 30%. The actual heat transfer coefficients for the modified fins were higher than the baseline as opposed to those presented in Table 5. This outcome was expected given the additional enhancements added to the fins. Furthermore, the dog-bone cuts provided additional leading edges where boundary layers develop, increasing the heat transfer coefficient. The fin effectiveness, however, went from 0.8 to 0.5, meaning the Schmidt method was not adequate for these fins.

Table 10: Fin Effectiveness Analysis for the Outdoor HX.

HX	Baseline	Type 1	Type 2
η_o*h (W/m².K)	79.2	65.3	71.1
h (W/m².K) – CFD + Schmidt	105.1	82.1	91.3
η_o (-) – CFD + Schmidt	0.75	0.80	0.78
h (W/m².K) – Actual	112.9	126.2	135.1
η_o (-) – Actual	0.70	0.52	0.53
η_o Deviation	-6.87%	-34.94%	-32.43%

This study assessed the thermal performance of these novel fins and highlighted the importance of the contact between tube and fin. The simulations assumed no resistance between the tube and fins, and the results showed that the effectiveness of these modified fins was only 50%, with potentially worse real performance. This lesson was carried forward when developing novel designs and manufacturing solutions.

5.1.2.Initial Fin Design

The most common enhancement methods for HX fins are slits (raised lances) (Figure 12a), louvers (corrugated lances) (Figure 12b) and winglets (turbulence generators) (Figure 12c). The last two were selected for study given their apparent potential for better enhancement. While slits, as shown in Figure 12a, can have as many leading edges as louvers, the first slits were more effective since they "see" a higher impinging air velocity, whereas the trailing edges caused flow disruption and reduced the velocity at the stagnation point on the subsequent slits. This assessment was purely theoretical and served only as a reasoning for selecting enhancement types; in no way is this meant to suggest that slits will perform worse than other enhancement methods, since they are widely used in many HXs.

Different concept ideas were investigated incorporating the various enhancements, however only two are presented here including the winglet/louver combination (Concept I, Figure 13a) and all louver (Concept II, Figure 13b). The latter refers to two types of louver: the "upper louver", which are the louvers filling the space between tubes that don't have the dog-bone cut; and the "lower louver" which are placed in the space adjacent to the dog-bone cut. The upper and lower louvers do not necessarily have the same dimensions and characteristics.

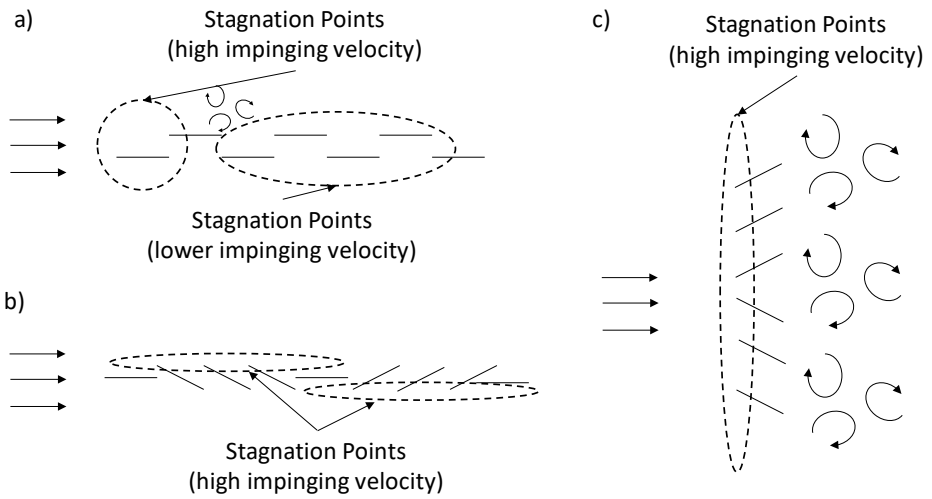

Figure 12: Enhancement types: a) Slits; b) Louvers; c) Winglets.

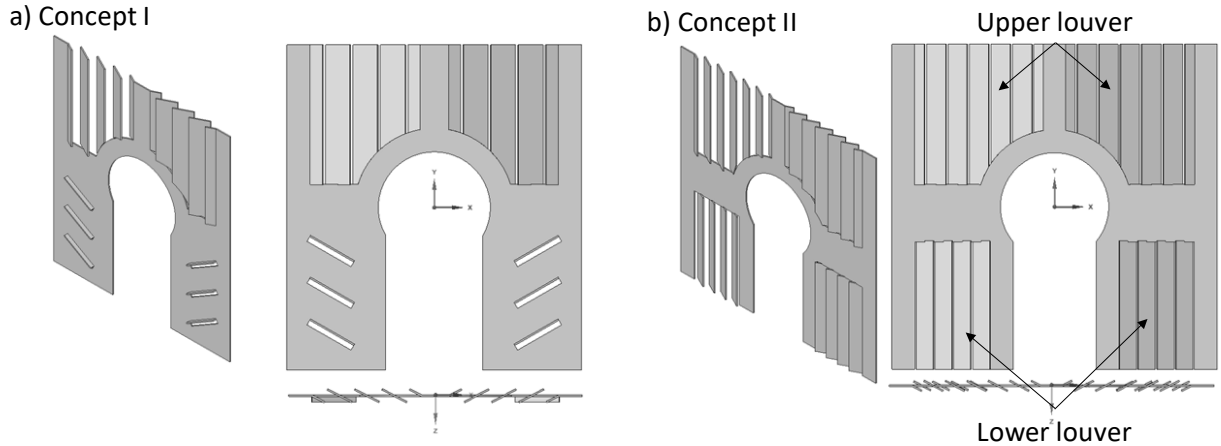

Figure 13: Concepts Investigated: a) Concept I: louvers and Winglets; b) Concept II: All Louvers.

As is outlined in Section 5.2.1, 7.1mm (close to baseline diameter) outer diameter (OD) tubes were obtained for preliminary testing and HX assembly. As such, designs were developed using such tubes with the intent of using the designs for sample HX prototypes. Design I (Figure 14b) uses Concept I (Figure 13a) where the diameter was reduced to 7.1mm while all other dimensions were proportionally reduced using the same baseline ratios. Design II (Figure 14c) is a result of modifications on both Concepts I and II where the diameter was reduced to 7.1mm, but the aspect ratios were changed such that the fin width and tube vertical spacing were three times the tube diameter. These modifications resulted in surface area compensation. Additionally, the number of louvers was increased so that higher average heat transfer coefficients were obtained.

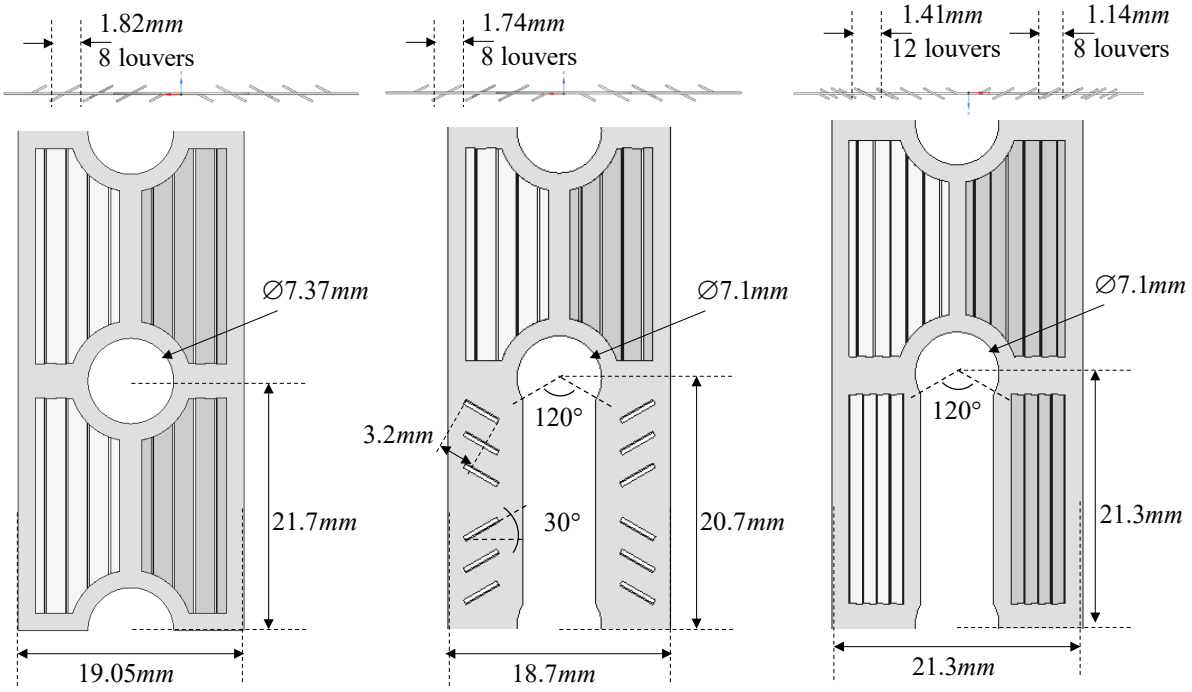

Figure 14: Fin designs: a) Baseline; b) Design I; c) Design II.

Each of the designs were analyzed using CFD simulations to evaluate airside heat transfer coefficient and pressure drop under the same velocities (the further analysis on full-scale HX assumed same face area).

A visual analysis on temperature profiles (Figure 15) showed distinct characteristics of the different enhancement types, as well as the impact of the dog-bone cut. The smaller distance between tubes resulted in both Designs I and II having slightly lower

temperature gradient in the "upper louver" portion compared to the baseline; the benefit was an incremental improvement in the fin effectiveness. Unfortunately, the dog-bone cut portion of the fins had a significantly higher temperature gradient than the new designs, which compensated for the previous effect and resulted in much lower overall fin efficiency. These results were expected; however, it was also shown that although Design II seemed to have higher temperature gradients, the overall heat transfer was more effective than Design I. This was observed by the air temperature contours where for Design I, there was a clear stream of lower temperature in the winglet session. Although additional optimizations could have been made, these results suggested that, of those evaluated, Concept II was the best option for the new designs.

While it was the best of the proposed solutions, Design II was clearly inferior to the baseline when it comes to overall heat transfer since the outlet air temperature in the baseline was higher than that for Design II. The major contributor was that the fin cut reduces tube-fin contact, thus reducing the fin effectiveness. A simulation using constant fin temperature on Design II revealed that the true heat transfer coefficient was 30% higher than the baseline due to the additional number of louvers. The fin effectiveness was, however, 40% lower. A general parametric study investigated minimizing the degradation due to lack of tube-fin contact.

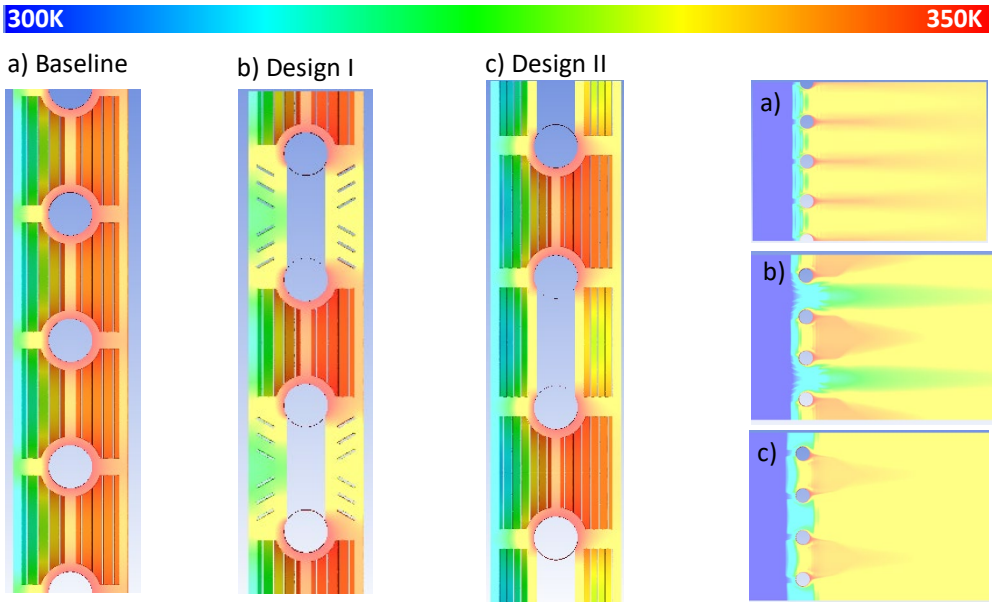

Figure 15: CFD Results, Temperature Contours

5.1.3. Impacts of the Dog-Bone Cut and Gap

The orientation of the tubes themselves is important to consider in confirming an appropriate fin design. The serpentine tubes can be bent in serpentine fashion, or oriented according to a corrugation angle (Figure 16). When the corrugation angle is 0° (straight), the serpentine covers each tube bank in series and the fin cuts are vertical. When the corrugation angle is different than 0° (slanted), the serpentine "zig-zags" back and forth in between two consecutive tube banks.

For multiple bank coils, either type of serpentine can be used. The straight type applies to Full-cross Counter Flow (Figure 17), while the slanted can be arranged for Semi-cross Parallel or Counter flows (Figure 17). On single bank coils, only straight serpentines are valid. Analysis revealed that each type of circuiting had an impact on the overall performance, however the full-cross counter flow was theoretically expected to be the best option.

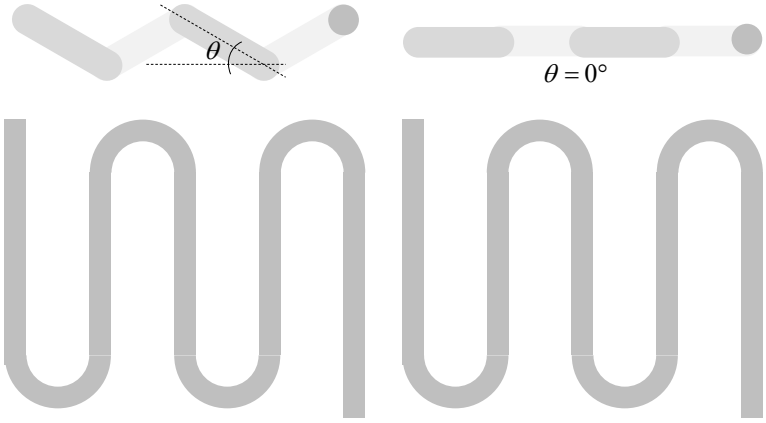

Figure 16: Serpentine Tubes

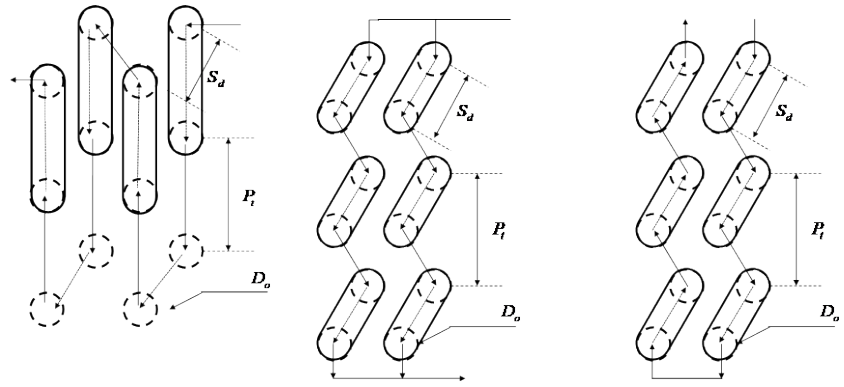

Figure 17: Multiple tube banks circuiting and fin options

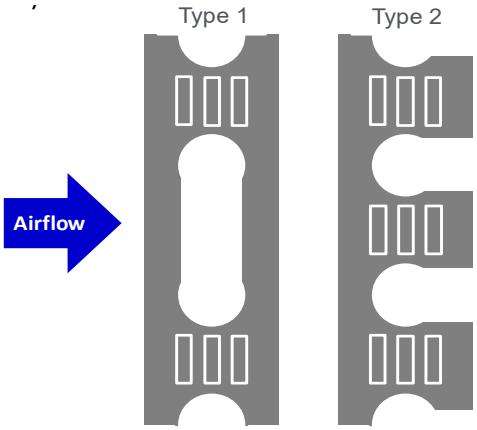

Figure 18: Single Bank Tube Cuts

In addition to establishing circuiting options, the serpentine type has a direct impact on the fin surface area since it determines how much material needs to be removed for the dog-bone cut. An investigation of the fin area reduction as a function of the tube pitches for the different types of serpentines was conducted. For multiple banks (Figure 19a), the diagonal cut was less sensitive to the tube pitches yielding area reduction of factors between 0.65 and 0.85. The vertical cut ranged between 0.6 and 0.9 but was much more sensitive to the tube pitches; the larger the transverse over the longitudinal pitch was, the less area was reduced. The vertical and diagonal were identical when the tube arrangement was equilateral (θ = 30°).

For single bank coils (Figure 20) the fin cut could, theoretically, be either vertical (Type I) or horizontal (Type II). Although Type I cuts result in less surface area reduction (Figure 19b), there are a few reasons Type II should still be considered; in particular, the vertical cut removes a valuable area for fin enhancements:

a) **50% less core enhancements;**
b) **The minimum free flow area has the highest air velocities, thus the highest heat transfer coefficients can be achieved; and,**
c) **The horizontal cut removes surface from the wake region, which has low flow velocities and no boundary layer developments, thus is less noble from a heat transfer point of view.**

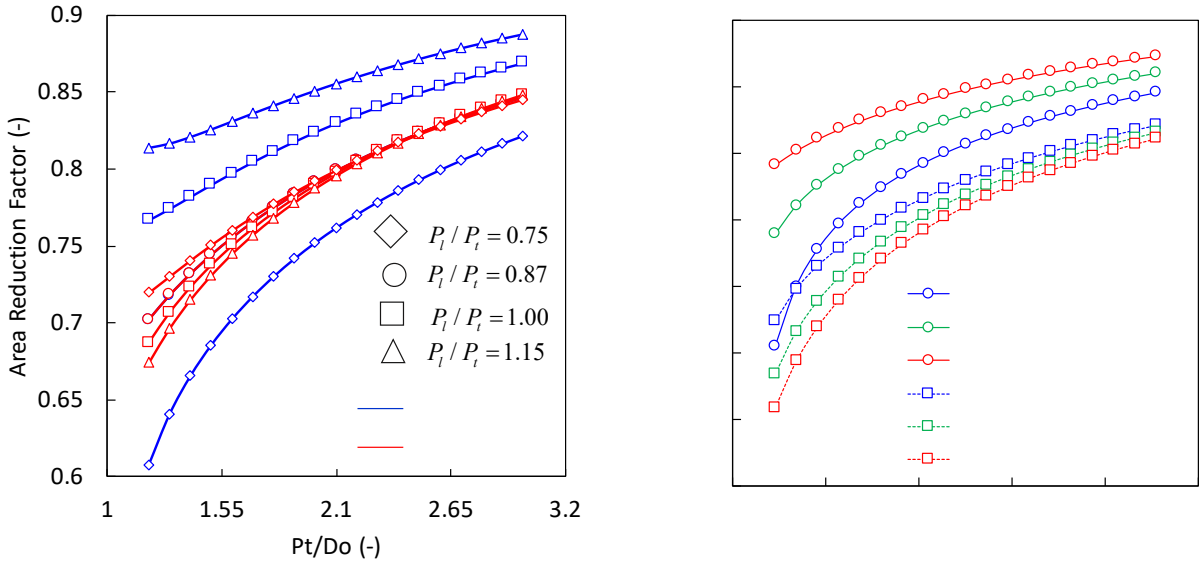

Figure 19: Fin area reduction: a) Multiple banks; b) Single bank.

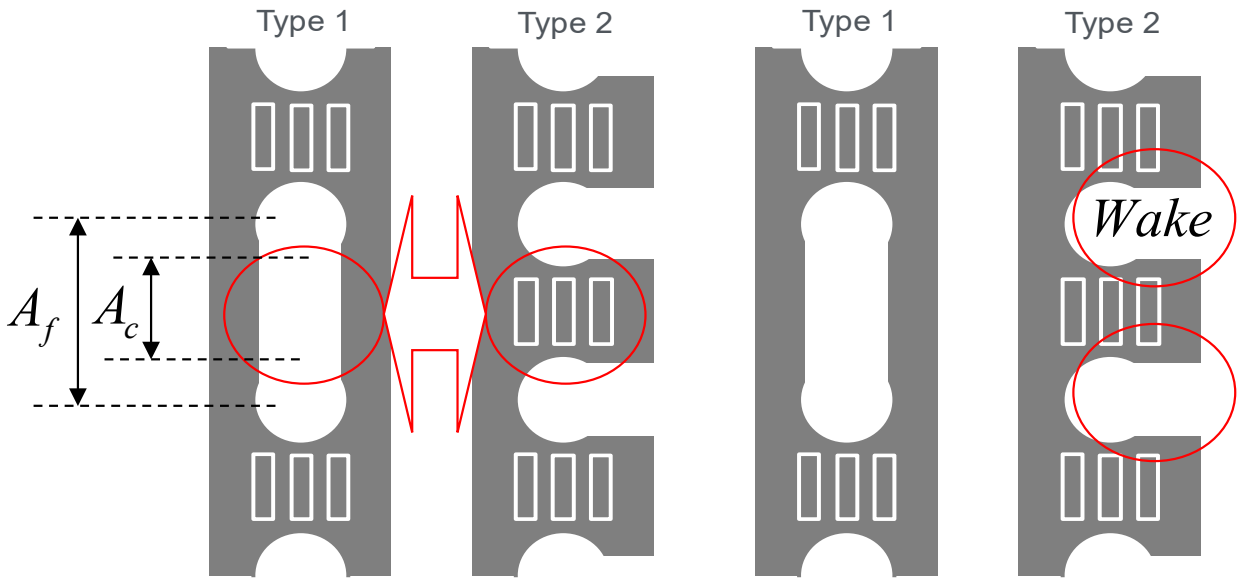

Figure 20: Single Bank Fin Cuts

Traditionally, the serpentine tubes are inserted through the fin stack in the transverse direction (z-axis) (Figure 21). For Type II, this kind of assembly cannot be done without modifications; Figure 21b illustrates the two possible ways of doing so: one would be lateral insertion of the fins (x-axis), while the other would be bending one of the serpentine tips so that it can move through transversally.

In addition to tube configuration, an analysis was conducted to evaluate how much of the gap of the cut could be reduced. The cost of doing reveals how much the serpentine elbow needs to be flattened in order to pass through the cuts (Figure 22).

The advantages of reducing the gap (or reducing the angle θ as shown in a) included larger surface area (equations 6-7), more room for placing enhancements near the dog-bone cut, and lastly, reducing the contact area penalty (equation 8).

The cut requires the elbow that is pushed through the fins to be flattened (Figure 23b, c). As the elbow flattens, its cross-sectional area reduces, thus increasing a local flow resistance. For this analysis, it was assumed that the cross-sectional shape flattened to an ellipsoid shape with the same perimeter as the original round tube (Figure 23).

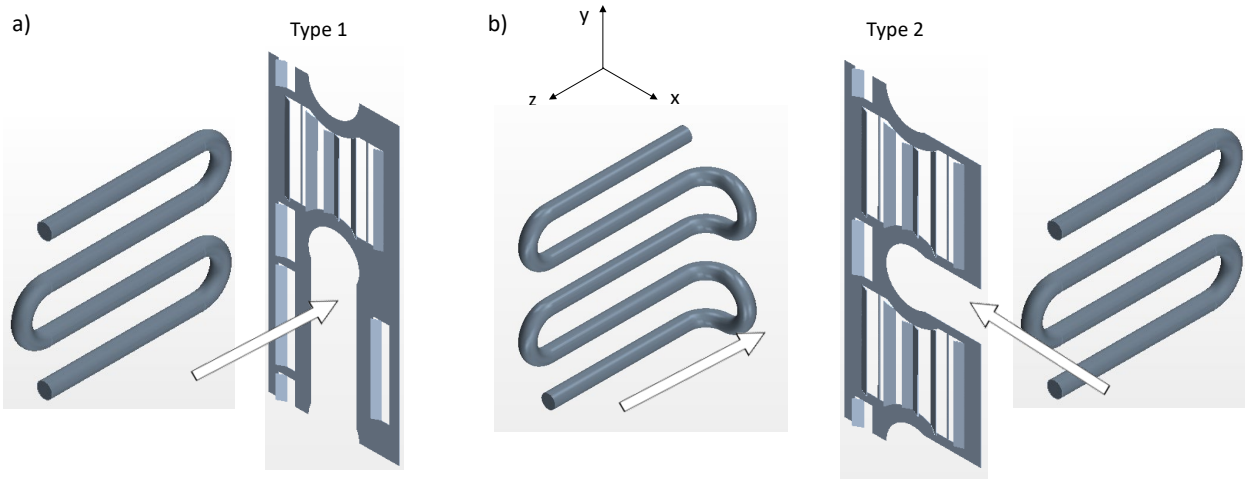

Figure 21: Single Bank Serpentine-to-fin Assembly.

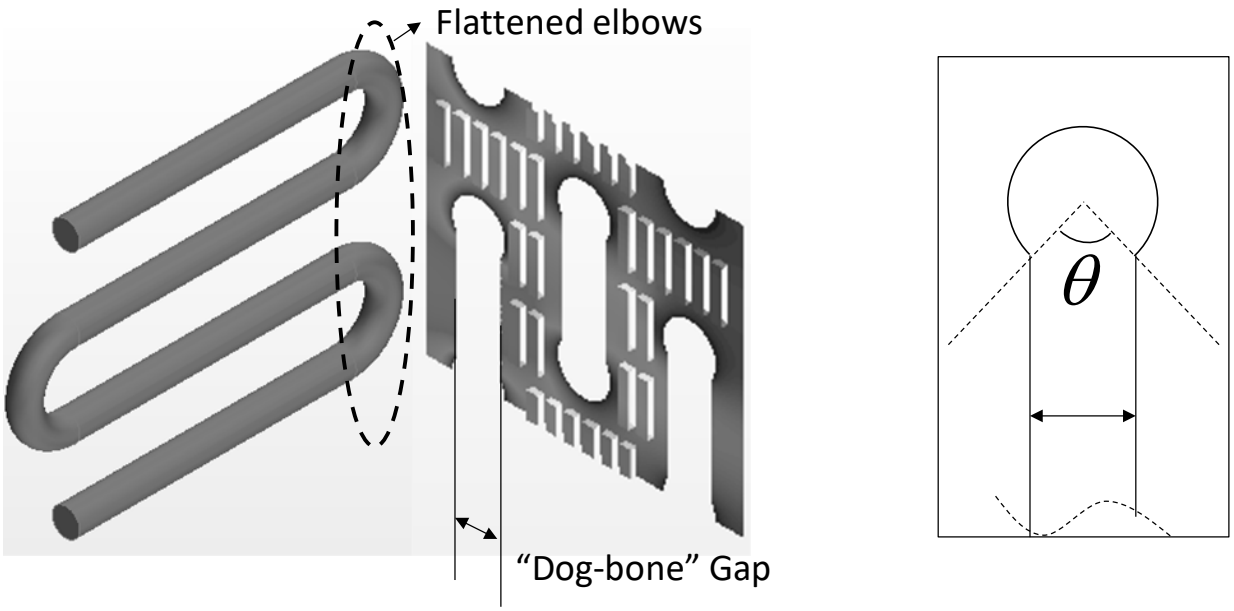

Figure 22: Serpentine – fin assembly.

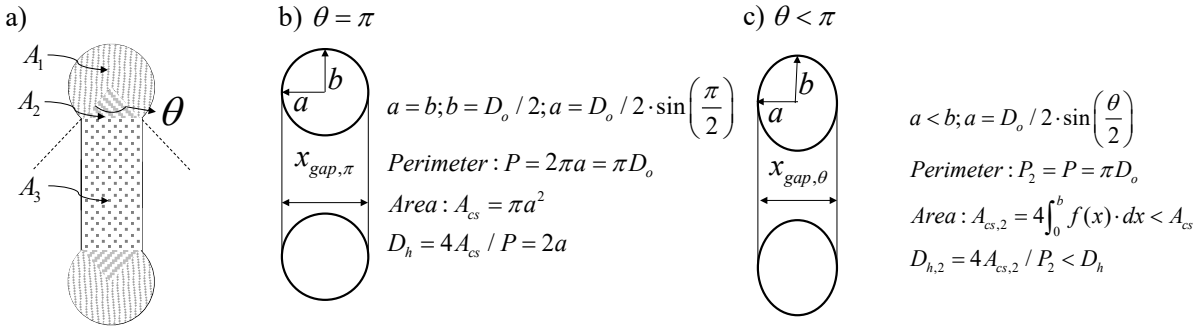

Figure 23: Dog-bone gaps

$$A_1 = \left(\pi - \frac{\theta}{2}\right) \cdot \frac{D^2}{2} \tag{6}$$

$$A_2 = \frac{D^2}{2} \cdot \sin\left(\frac{\theta}{2}\right) \cdot \cos\left(\frac{\theta}{2}\right) \tag{7}$$

$$A_3 = D \cdot \sin\left(\frac{\theta}{2}\right) \cdot \left[P_t - D \cdot \cos\left(\frac{\theta}{2}\right)\right] \tag{8}$$

$$A_{gap} = \sum_{i=1}^{3} A_i \tag{9}$$

$$\zeta_{contact} = \frac{2\pi - \theta}{2\pi} \tag{10}$$

The pressure penalty was not easily determined since the friction factor relates significantly differently to the Reynolds number depending on whether it is laminar or turbulent and has smooth or rough walls. However, for this analysis, since the perimeter was constant, the reduction of the hydraulic diameter was identical to the increase in velocity; therefore, the Reynolds numbers were always the same. With these considerations, the pressure drop penalty factor was estimated according to equations 11 and 12.

$$\Delta P = f \frac{l}{D_h} \frac{1}{2} \frac{\dot{m}^2}{\rho A_{cs}^2} \rightarrow \Delta P \propto \frac{1}{D_h \cdot A_{cs}^2} \tag{11}$$

$$P_f = \frac{D_{h,1} \cdot A_{cs,1}^2}{D_{h,2} \cdot A_{cs,2}^2} \tag{12}$$

The normalized (baseline: cut angle=180°) results of this analysis are shown in Figure 24. The results suggested that for angles below 100°, there is a significant impact with a pressure drop penalty factor of about 1.25.

An additional design, namely Design III, was created with the same general dimensions as Design II (Section 5.1.2), but with a cut angle of 100° (Figure 25). The cut angle also had a direct impact on the "lower louver" dimensions since there was more room for them.

CFD simulations of Designs II and III demonstrated that as the cut angle decreases, fin effectiveness increases. The latter is illustrated in Figure 26 where the temperature gradient on the "lower louver" for Design III was smaller than that for Design II. In fact, when doing the data reduction, the effective heat transfer coefficient (product of airside heat transfer coefficient by the fin effectiveness) was 7.8% higher.

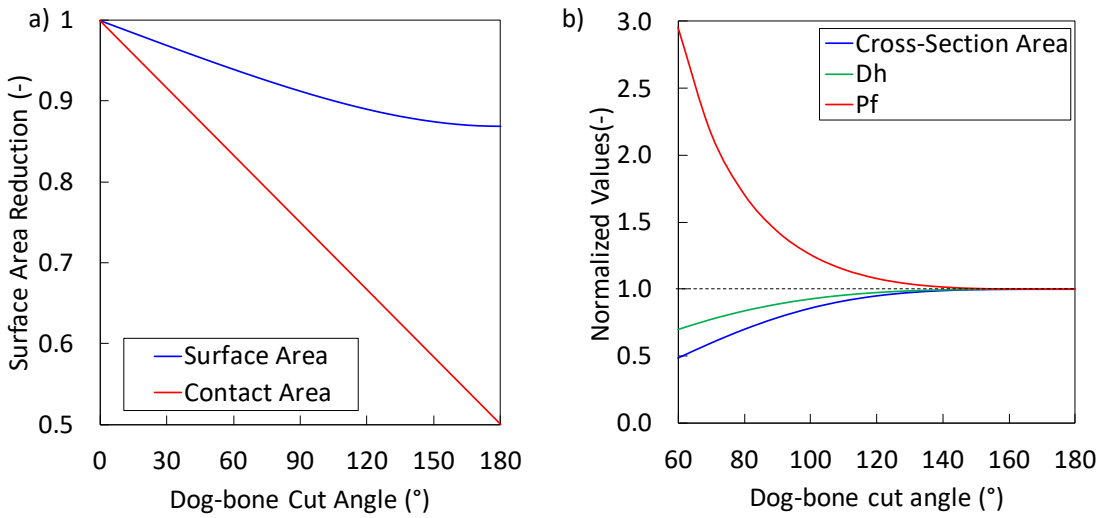

Figure 24: Cut Angle: a) Benefits; b) Drawbacks.

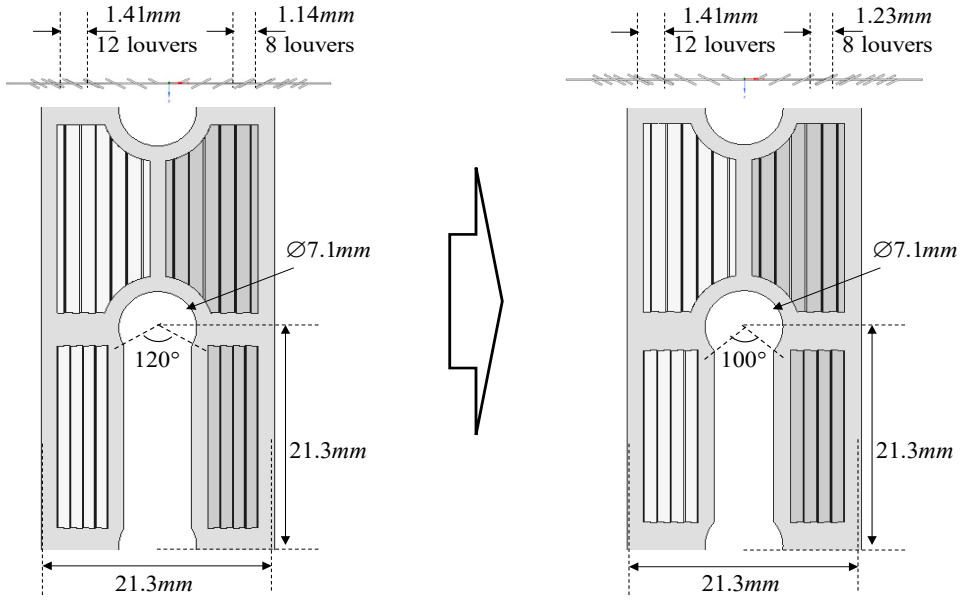

Figure 25: Fin Design a) II and b) III

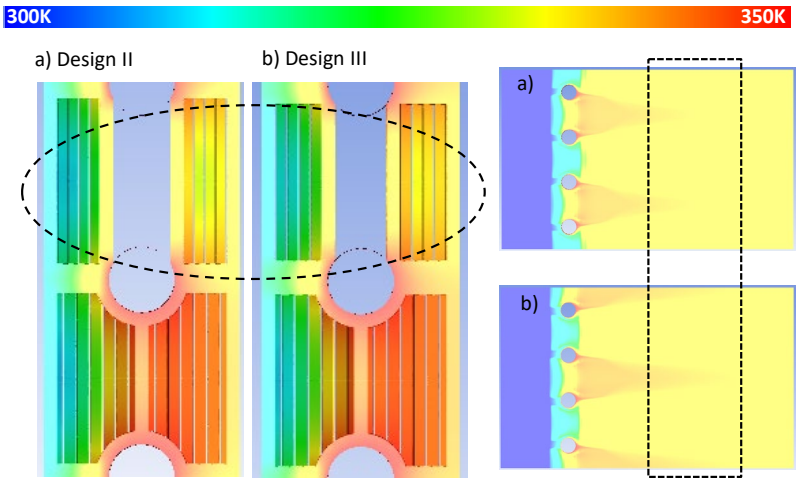

Figure 26: Temperature Contours for Fin Design a) II and b) III.

Further analysis evaluated the impacts when the air flowrate was allowed to change from the baseline with the constraint that the total pumping power (equation 13) should be equal or lower than the baseline.

$$\dot{W}_p = \dot{V}_{air} \cdot \Delta P_{air} \tag{13}$$

Designs II and III were simulated under the baseline velocity (1.02 m/s) and 1.2m/s. The latter is an arbitrary upper bound velocity for residential condensers. With two CFD results for each, a simple curve fit in a physical model (equations 14-15) was developed to allow finding pressure drop and heat transfer coefficients in that range of velocities (Figure 27). These curve fits were later used to evaluate the impact on overall HX performance. The plots in Figure 27 show, however, that for these designs, the pressure drop penalty starts occurring at around 5-10% higher air velocities, which gives less than a 2% heat transfer improvement. Better improvements were found during the optimization (Section 5.1.5).

$$\Delta P \propto \mathrm{Re}^b \rightarrow \Delta P \cdot \dot{V} = a \cdot u^{b+1}; a, b = \text{constants} \tag{14}$$

$$h \propto \mathrm{Re}^d \rightarrow \eta_o h = c \cdot u^d; c, d = \text{constants} \tag{15}$$

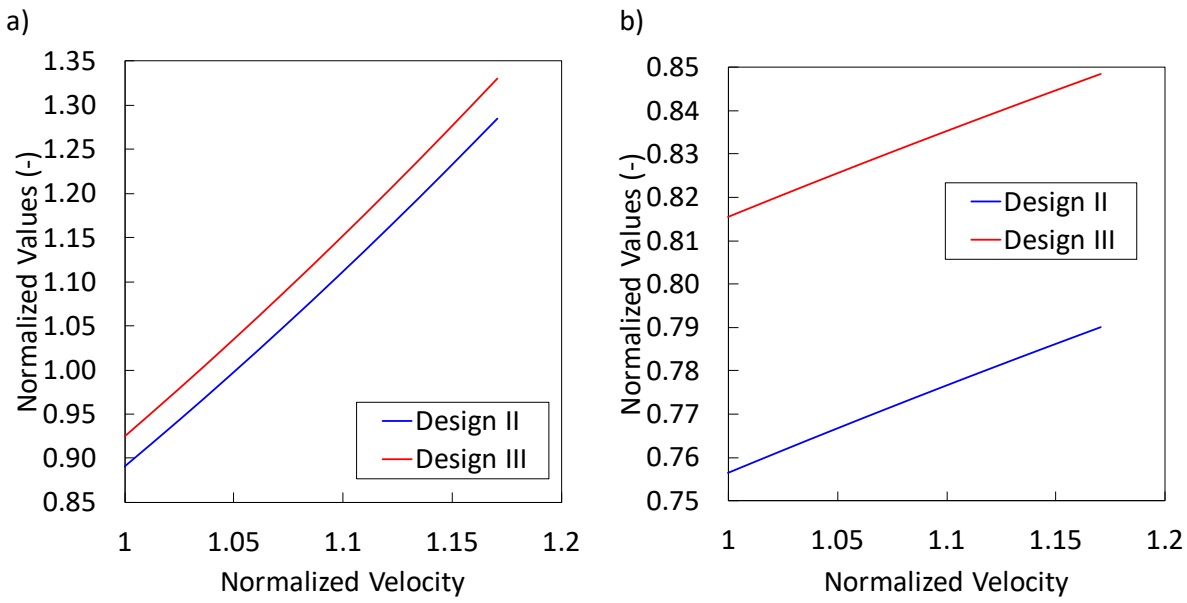

Figure 27: Curve fits: a) Pressure Drop; b) Effective Heat Transfer Coefficient.

5.1.4. Split-Merge Joint

The performance analysis study presented in Section 0 presented the dilemma of attempting to achieve the 70% joint reduction standard without imposing significant increases in pressure drop. One identified solution for this problem was combining feeding and discharging streams in pairs, i.e., feeding two circuits with a single connection, thus resulting in a single joint for two circuits. The conventional joining results in two joints per circuit (Figure 28a) – one feeding and one discharging (equation 16). The proposed idea was to split and merge streams (Figure 28b, c) such that the number of joints increases with circuits at a factor of one instead of two (equation 17**).**

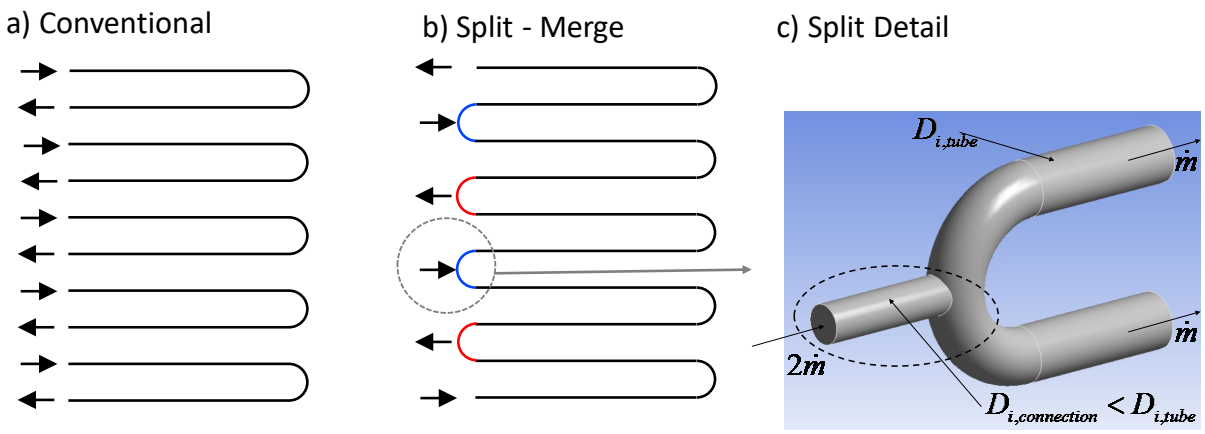

Figure 28: Circuiting Types.

$$n_{\text{joints,conventional}} = 2 \cdot n_{circuits} \quad \textbf{(16)}$$

$$n_{\text{joints,split-merge}} = n_{circuits} + 1 \quad (17)$$

The two major benefits from implementing such circuiting are: a) significant joint reduction per circuit; and b) potential for refrigerant pressure drop reduction. The first advantage is clearly demonstrated by equations 16 and 17**. For five circuits, for example, the number of joints with conventional joining is ten, while with split-merge it is six. If a baseline has 28 tubes (joints), thus 10 joints corresponded to a 64% reduction and 6 joints corresponded to a 78% reduction. Additionally, if it were possible to reduce the number of circuits down to 4, then the reduction would have been approximately 85%. The limiting factor was the refrigerant pressure drop. Figure 29 illustrates the difference between using the different circuiting approaches.**

This approach, however, has some important drawbacks to consider. The split-merge connections essentially became "bottle-necks". In these connections, the refrigerant flow rate needs to be two times the flow rate of a single circuit, and the connection diameter must be smaller than the tube itself. Both consequences would have significant impact on local pressure drop given the high fluid acceleration. For the latter, the feeding streams of a condenser are in vapor phase and if the connection was too restrictive, compressibility effects could take place, enhancing the negative impact on pressure drop. Moreover, there is potential for enhanced maldistribution. Conventional tube-fin HX distributers have an intrinsic maldistribution problem of

their own; once the flow is split in this fractal manner, there could be another source of maldistribution.

Although joining a connecting tube to the serpentine is a straight-forward process, making holes in the serpentine tubes can be a challenge with respect to tools, manufacturing order and shape and sizes. Four options for addressing such concerns are considered. Since conventional drilling is not possible due to the deposition of metal dust and specs inside the tube, techniques such as puncturing, piercing and cutting must be used.

The first method leverages the fact that the tubes for this HX need to be seamed and coated with clad material for the fin brazing described in the previous report. Here the holes would be cut in a semi-circle before rolling the metal sheets into tubes (Figure 30a). Although cutting the holes seem simple, this method requires the tube manufacturer to be involved and the coating would cover the tubes, making it harder to track them. This approach is very unlikely to work.

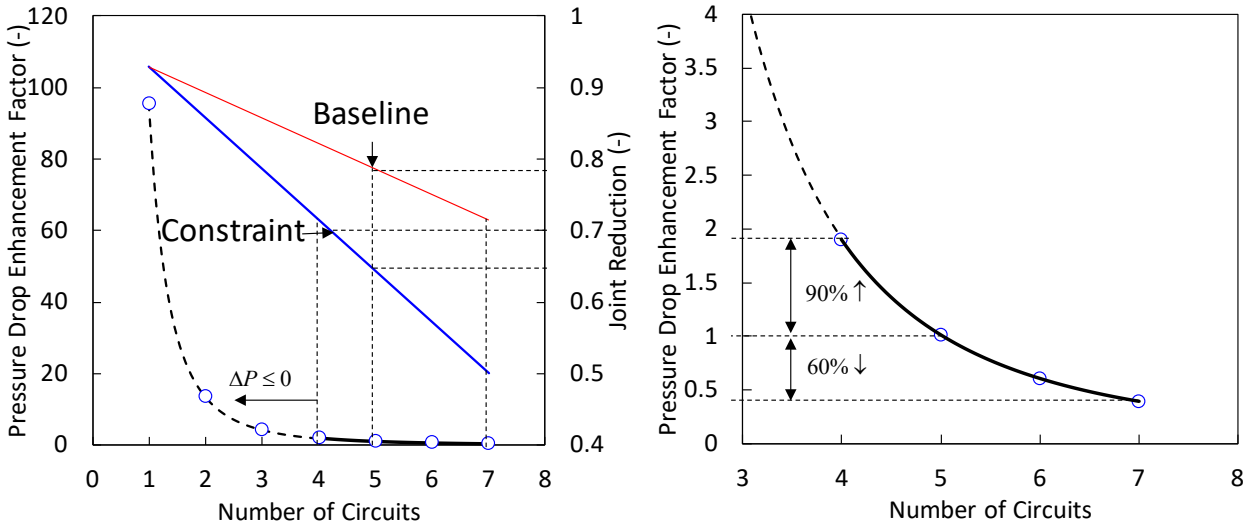

Figure 29: Split-Merge Impact

The second (Figure 30b) approach is puncturing a hole at the end of all other manufacturing processes. The idea is to puncture the hole on the elbows after brazing the fins to avoid hole tapping with clad material. The drawback is having a tool that could fit the small space between the inside of the elbow and the fins.

The third (Figure 30c) approach is puncturing a simple round hole on the tube straight before bending into a serpentine arrangement. Puncturing this kind of hole

should be relatively easy; however, when a round hole is punctured on the straight tube, it becomes an ellipse once bent for the serpentine arrangement. Additionally, the hole locations need to be precisely calculated to match the coil design.

The last idea (Figure 30d) is a variation of the previous, where the hole punched would be elliptical with a vertical orientation, as such that when the tube is bent, the hole becomes round. The challenge is to have the exact tool to puncture such a hole. Ultimately, this idea was not utilized since the U-bends were received from the supplier. The final prototypes also did not incorporate the split-merge joint. In general, the split-merge joint proved difficult to make and unnecessary to achieve the necessary level of performance and joint reduction.

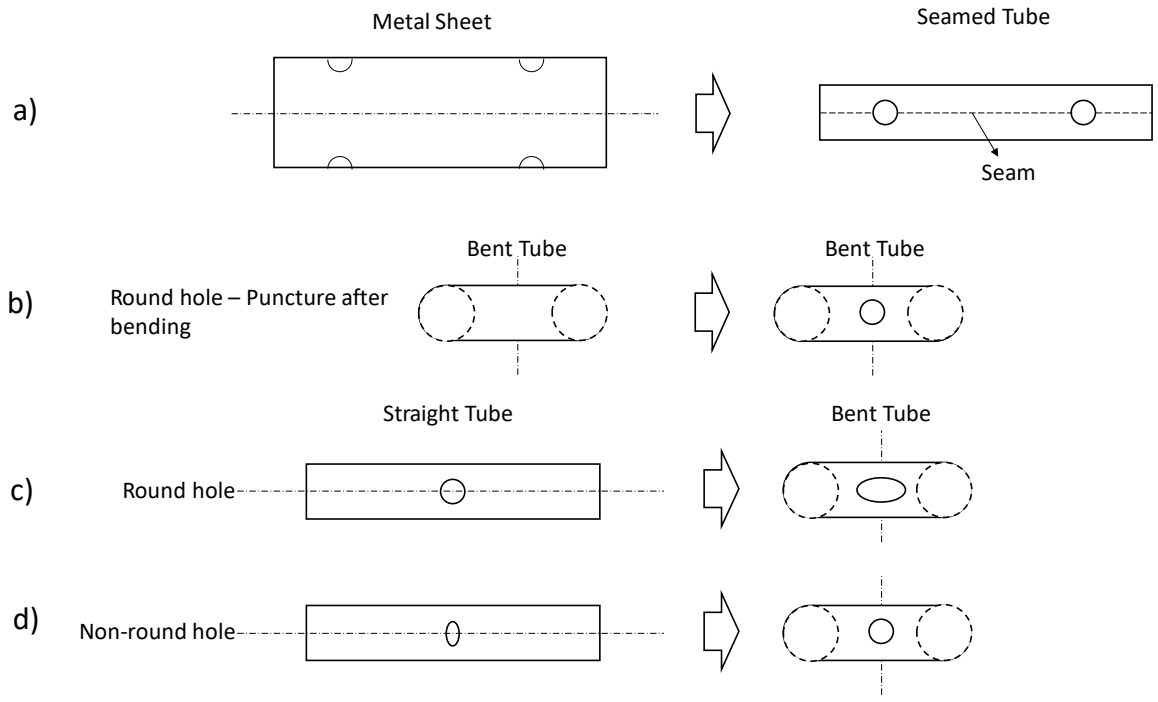

Figure 30: Feeding / Discharging Holes for the Split-Merge Concept

5.1.5. Optimization

Upon completion of preliminary analyses, a handful of potential enhancement designs for the dog-bone fins had emerged. A full optimization study was conducted to identify additional designs to enhance performance.

5.1.5.1. Methodology Overview

The framework for fin optimization can be broken into four parts as illustrated in Figure 31 and as outlined below.

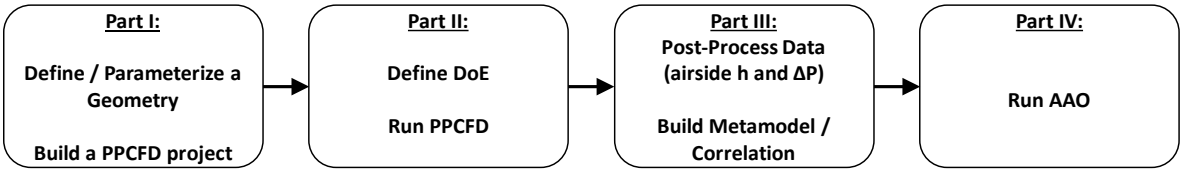

Figure 31: Design Optimization Framework

Part I: Geometry Definition and Parallel Parameterized (PP)CFD Project Development (Figure 32): This step in the optimization process is the most engineering time-consuming part, where the development of the modeling and simulation project involves program writing, debugging, repeatability and reliability testing and automation.

When evaluating a large number of parametrized geometries, CFD can often become computationally expensive and time-consuming. PPCFD involves automating the CFD simulations, allowing the shape and topology to change during the runtime, saving significant engineering time.

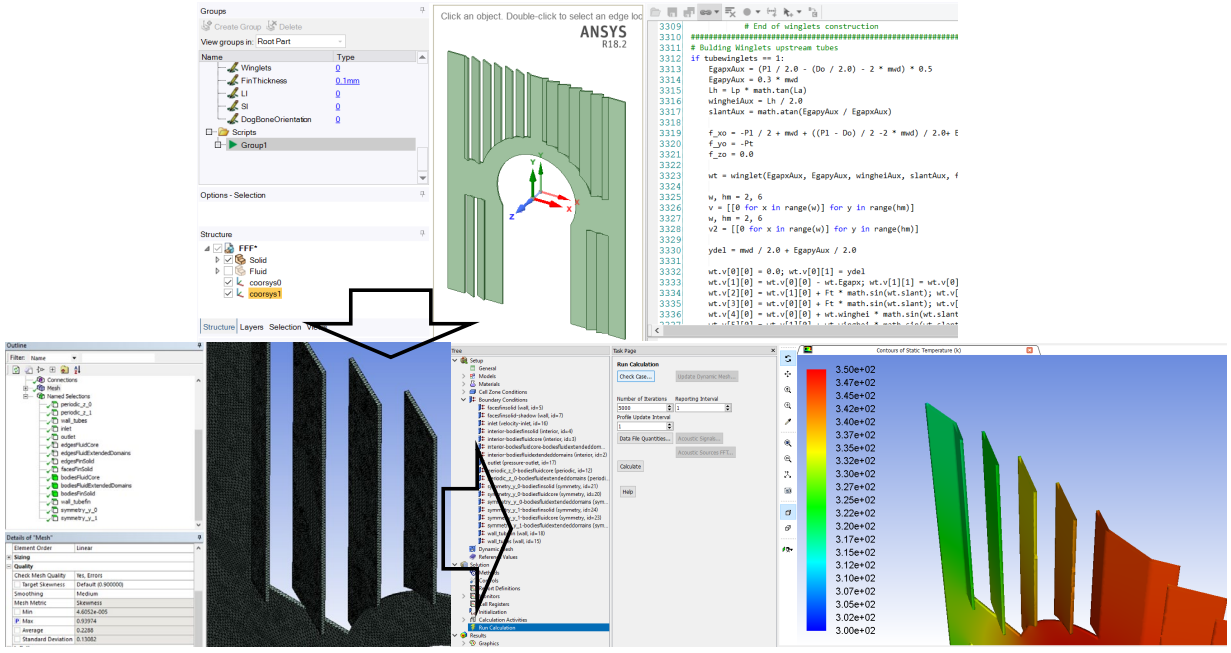

Figure 32: Design Optimization: Part I (Illustration Only)

Part II: Design of Experiments (DoE) and Simulation Runs (Figure 33): This part of the optimization is the most computationally- intensive part of the project, since it involves simulating a large design of experiments (DoE) in CFD. The DoE was generated using the Latin Hypercube Sampling (LHS) method, however the precise

number of design variables was defined beforehand. The number of design variables also determined the size of the DoE. There is no formal rule as to the definition of the DoE size, however it can be estimated using equation 18. The power term in the equation represents the combination of all the upper and lower bounds for each design variable, plus one (1). The latter represents the middle point of all design variables. The linear term (K is constant) represents the designs from the LHS; the value of K is "arbitrary", however a value of 50 has been used successfully in previous studies.

The original optimization problem identified 10 variable parameters (assuming the tube diameter is fixed), which would result in a DoE containing 6,025 designs. Given the large number, it is paramount that the preceding processes are revised thoroughly to avoid having to repeat this step.

$$N_{DoE} = 2^{N_{dv}} + 1 + K \cdot N_{dv} \quad \textbf{(18)}$$

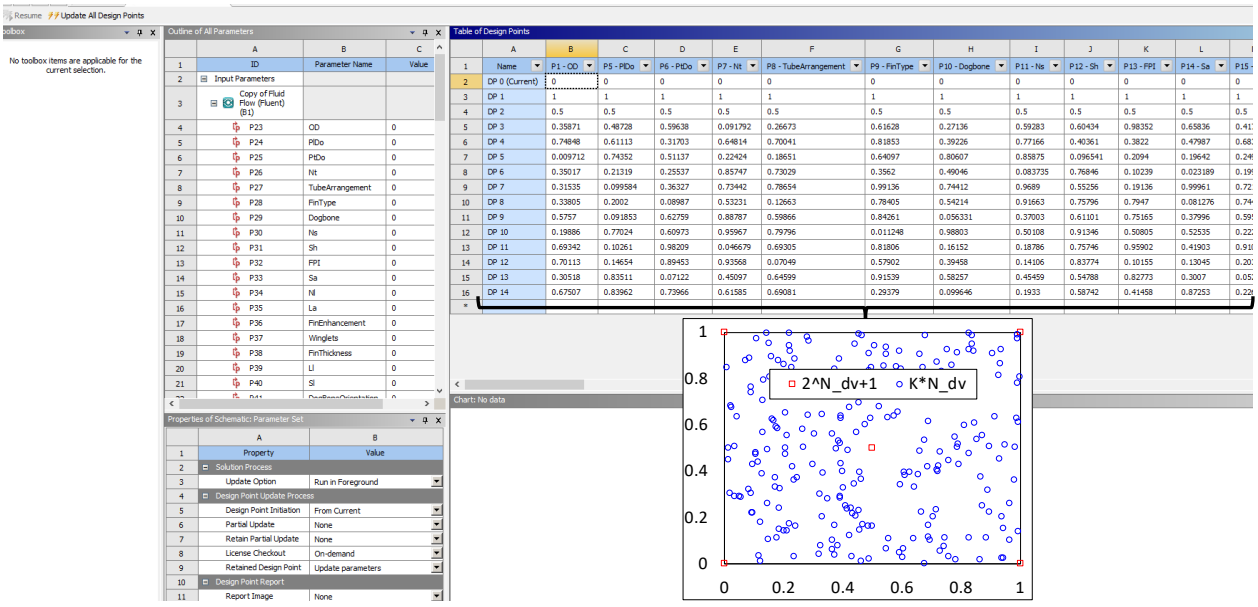

Figure 33: Design Optimization: Part II (Illustration Only)

Part III: Post-Process Data and Metamodel Development (Figure 34): The third step of the optimization is neither computationally nor engineering intensive, unless there is no good fit (the deviation between prediction and actual output is too large) between input parameters and outputs. The biggest risk is having to revise the DoE and repeat the PPCFD by performing additional CFD simulations.

x1	x2	x3	x4	x5	y1	y2
0	0	0	0	0	138	44
1	1	1	1	1	67	195
0	1	1	1	1	132	218
1	0	0	0	0	103	275
0.5	0.5	0.5	0.5	0.5	113	34
0.803	0.606	0.800	0.173	0.964	65	473
0.221	0.965	0.882	0.898	0.617	192	458
0.954	0.756	0.474	0.000	0.988	190	311
0.231	0.608	0.828	0.634	0.461	68	284
0.917	0.119	0.157	0.339	0.149	128	299
0.230	0.431	0.628	0.679	0.563	193	399
0.496	0.433	0.967	0.191	0.473	198	394

$$\hat{y}_1(\underset{\sim}{x}) = y_1(\underset{\sim}{x}) + err$$
$$\hat{y}_2(\underset{\sim}{x}) = y_2(\underset{\sim}{x}) + err$$

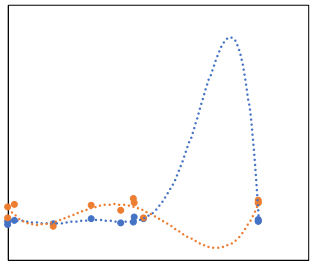

Figure 34: Design Optimization: Part III (Illustration Only)

Part IV: Run Approximation Assisted Optimization (AAO) (Figure 35): The optimization itself was straightforward and the computational intensity was much less than Part II since it didn't require CFD simulations. That is the advantage of using Metamodels (Part III) to approximate CFD solutions. This part did entail program writing and debugging for the proper functioning of the optimization code, which is customized for every application.

$$\hat{y}_1(\underset{\sim}{x}) = y_1(\underset{\sim}{x}) + err$$
$$\hat{y}_2(\underset{\sim}{x}) = y_2(\underset{\sim}{x}) + err$$

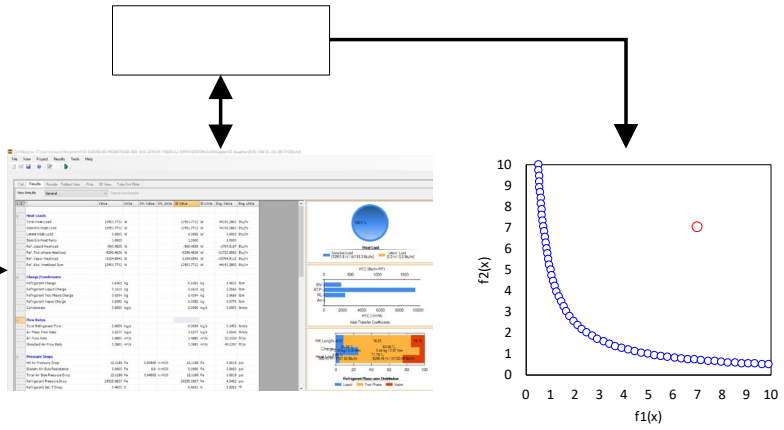

Figure 35: Design Optimization: Part IV (Illustration Only)

5.1.5.2. Execution

Throughout the optimization process, the ANSYS software used for CFD simulations presented some challenges, which were eventually circumvented using the Direct Optimization (DO) tool available in the ANSYS Workbench. This tool consisted of performing a direct CFD optimization using a Multi-Objective Genetic Algorithm

(MOGA). Although the end objective was to optimize the HX, the CFD DO was also used to generate the DoE required for the AAO methodology (Figure 35) The initial genetic algorithm population consisted of nothing less than a Latin Hypercube Sampling DoE, which was necessary for the metamodel development.

The design space was reduced from ten to six design variables, and the range of each design variable was relatively narrow (Table 11). As such, the required number of data points for an accurate metamodel could be reduced, thus reducing computational time. There was no need for additional simulations as the metamodels maintained their accuracy.

Table 11: PPCFD Design Space and Fixed Parameters

Design Variable	*Description*	*Unit*	*Type*	*Range*
P_t/D_o	Vertical Spacing to Diameter Ratio	-	Variable Continuous	2.96 - 4.0
P_l/D_o	Horizontal Spacing to Diameter Ratio	-	Variable Continuous	2.96 – 3.5
N_{ul}	Number of "Upper Louvers"	-	Variable Discrete	5 – 8
N_{ll}	Number of "Lower Louvers"	-	Variable Discrete	4 – 6
FPI	Fin Density	in^{-1}	Variable Continuous	18 – 24
u	Frontal Velocity	m/s	Variable Continuous	1.025 – 1.5
D_o	Tube Diameter	mm	Fixed	7.1
θ_{lca}	Louver Corrugation Angle	°	Fixed	27
N_r	Number of Rows	-	Fixed	1
δ_f	Fin Thickness	mm	Fixed	0.114
δ_m	Minimum Wall / Edge Distance	mm	Fixed	2.0
θ_{db}	Dog-bone cut angle	°	Fixed	120

A population of 100 designs and 65 new designs created by MOGA were simulated. A metamodel was developed with the 100 initial designs and was tested with the 65 new designs for accuracy verification purposes. The accuracy of a metamodel was quantified using the Maximum Acceptance Score (MAS), which is the percentage of points that fall within a determined deviation. For the metamodel to be acceptable, the MAS must be greater than or equal to the difference between unity and an arbitrary deviation threshold (e.g. 10% → $MAS_{10\%} \geq 90$). In this study, the heat transfer coefficient metamodel had an acceptable MAS of 10%, while the pressure drop had a MAS of 12%-13% (Figure 36). The latter is typically more difficult to achieve equivalent accuracy than as for the former. The worst predicted points mostly coincided on both metamodels, which made it easier to identify a potential "bad" design in the optimization.

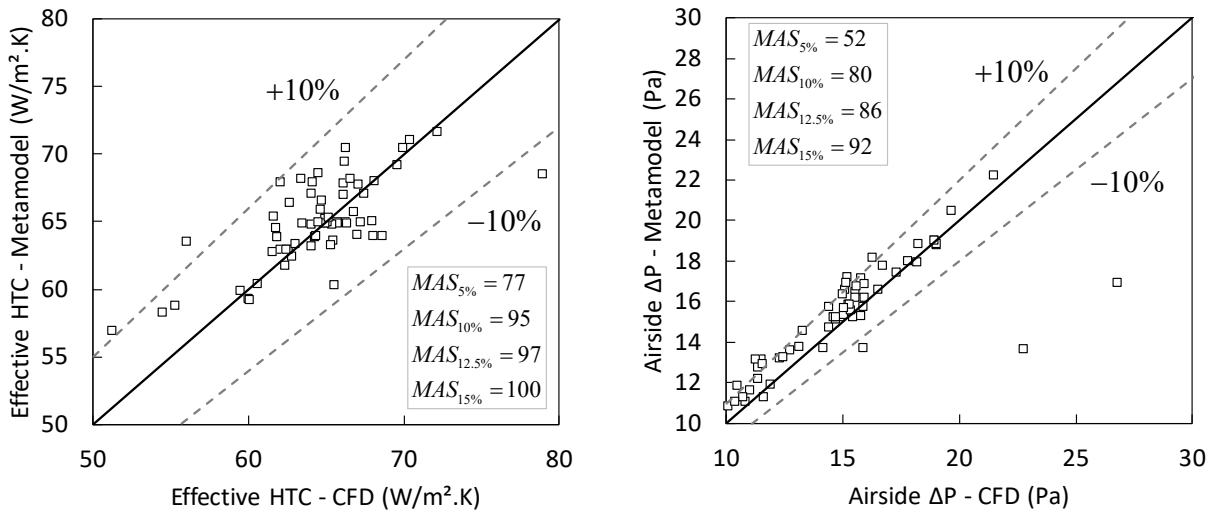

Figure 36: Metamodel Results

Two optimization studies (Table 12) were evaluated using the same objective functions. One allowed the airflow rate to change while keeping the same face area as the baseline. The other kept the same airflow rate as the baseline and the face area was constrained to remain smaller than the baseline. Five inequality constraints were considered; one of them was minimum joint reduction. Prior analyses, presented in Sections 0 and 5.1.4, indicated that to achieve the minimum 70% joint reduction target for the outdoor coil while respecting the performance constraints, the split-merge is the only approach (equation 17) that will enable feasible designs. A few optimization runs using the conventional serpentine joining (equation 16) were attempted, and the optimizer returned no designs because they could not satisfy both the refrigerant pressure drop and the joint reduction constraints. The design space for the optimization is detailed in Table 13.

Table 12: Optimization Studies Formulation

	Optimization I	***Optimization II***
$f_1(\bar{x})$	$\max \dot{Q}$	
$f_2(\bar{x})$	$\min \dot{W}_{fan}$	
s.t.		
$h_1(\bar{x})$	$\dot{Q} \geq \dot{Q}_{baseline}$	
$h_2(\bar{x})$	$\dot{W}_{fan} \leq \dot{W}_{fan,baseline}$	
$h_3(\bar{x})$	$\Delta P_{ref.} \leq 1.2 \cdot \Delta P_{ref.,baseline}$	
$h_4(\bar{x})$	$1 - \left(N_{joints,split-merge}/N_{joints,baseline}\right) \geq 70\%$	
$h_5(\bar{x})$	**N/A**	$A_{face} \leq A_{face,baseline}$
$g_1(\bar{x})$	$A_{face} = A_{face,baseline}$	$\dot{V}_{air} = \dot{V}_{air,baseline}$

Table 13: Optimization Design Space and Fixed Parameters

Design Variable	*Description*	*Unit*	*Type*	*Range*
$x_1 = P_t/D_o$	Vertical Spacing to Diameter Ratio	-	Variable Continuous	2.96 - 4.0
$x_2 = P_l/D_o$	Horizontal Spacing to Diameter Ratio	-	Variable Continuous	2.96 – 3.5
$x_3 = N_{ul}$	Number of "Upper Louvers"	-	Variable Discrete	5 – 8
$x_4 = N_{ll}$	Number of "Lower Louvers"	-	Variable Discrete	4 – 6
$x_5 = FPI$	Fin Density	in^{-1}	Variable Continuous	18 – 24
$x_6 = u$	Frontal Velocity	m/s	Variable Continuous	1.025 – 1.5
$x_7 = N_t$	Number of Tubes	-	Variable Discrete	24, 25, 27, 28, 30, 32, 35, 36
$x_8 = N_c$	Number of Circuits	-	Variable Discrete	N/A[8]
D_o	Tube Diameter	mm	Fixed	7.1
θ_{lca}	Louver Corrugation Angle	°	Fixed	27
N_r	Number of Rows	-	Fixed	1
δ_f	Fin Thickness	mm	Fixed	0.114
δ_m	Minimum Wall / Edge Distance	mm	Fixed	2.0
θ_{db}	Dog-bone cut angle	°	Fixed	120

5.1.5.3 Results

The optimization shown in Figure 37 resulted in considerable improvement from the first hand-design concept-to-proof (Design II). The challenge of achieving greater or equal heat load from baseline while avoiding prohibitive penalty on pressure drop on both working fluids had been achieved. The two constraints imposed on the optimization – fixed face area and fixed air flowrate – resulting in two pareto fronts of optimized design solutions. The designs where the air flowrate was allowed to increase (fixed face area, diamond points in Figure 37) exhibited the largest margin

[8] The number of circuits is determined by an algorithm that factors the number of tubes and calculates the product of a combination of these factors that can have 1,2 or 3 factors.

in heat load improvement (2.1%) and fan power reduction (10%). The designs with fixed flowrate (triangle points in Figure 37) had 0.6% heat load improvement and 3.5% fan power reduction.

It is important to note that the performance differences shown in Figure 37 were marginal; i.e. they are within the level of uncertainty. A group of 10 optimum designs from both Pareto fronts were selected for CFD verification. These designs were carefully picked from different regions in the Pareto fronts; i.e. compensating designs (end points) and non-compensating designs (middle points). The metamodel predictions consistently exhibited an *overestimate in HTC of up to 5%* and an *overestimate in pressure drop between 3% and 10%* (Figure 38). The fact that the prediction deviations were somewhat constant suggested that, with simple correction factors, the accuracy of the metamodels could have been improved. The results, however, were satisfactory from a metamodel accuracy standpoint; they were within expected uncertainty, thus there was no need for further development.

The selected designs exhibited an average 5% higher HTC. The impact on overall HX performance was of the order of 1-1.5%, thus reducing the 2.1% margin originally observed (Figure 37) by nearly half. Nevertheless, the designs were still competitive and better than Design II. The pressure drop, on the other hand, was overpredicted by 5% on average, thus stretching the margin of fan power reduction from 10% to 15%.

Although there were seemingly a wide range of optimum alternatives, the design differences were subtle. Every optimum design had practically the same tube vertical spacing, which corresponded to the minimum bending radius for the serpentine forming.

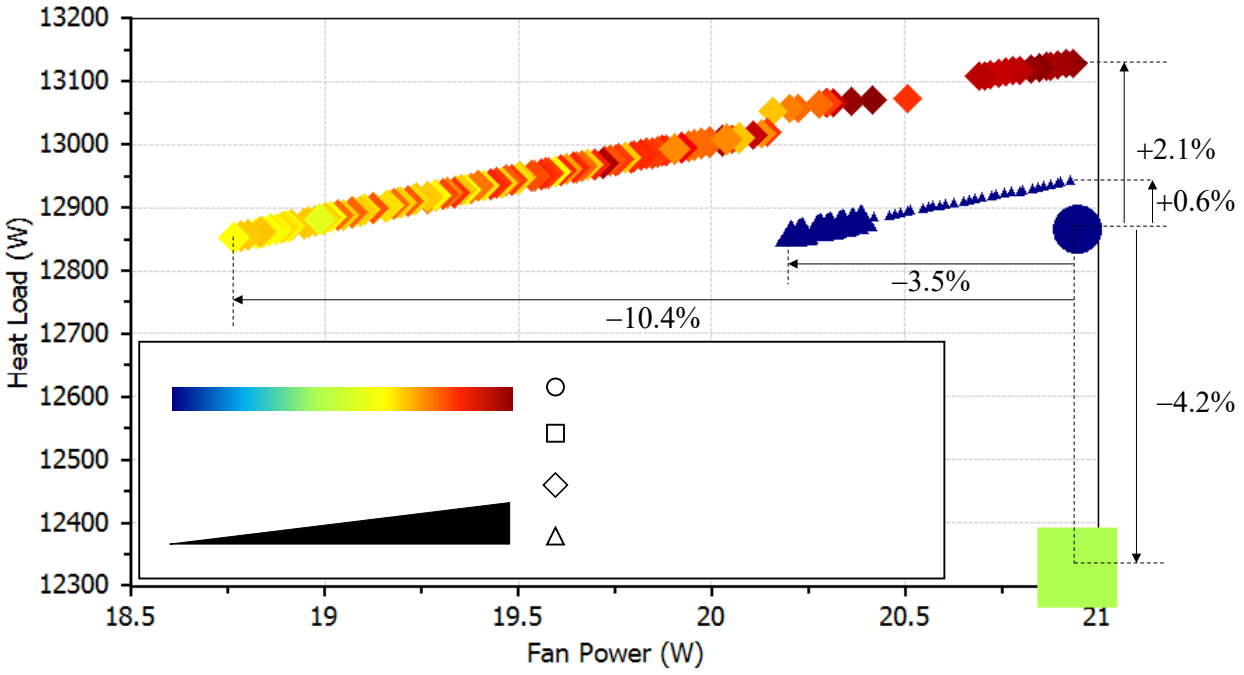

Figure 37. Optimization Results.

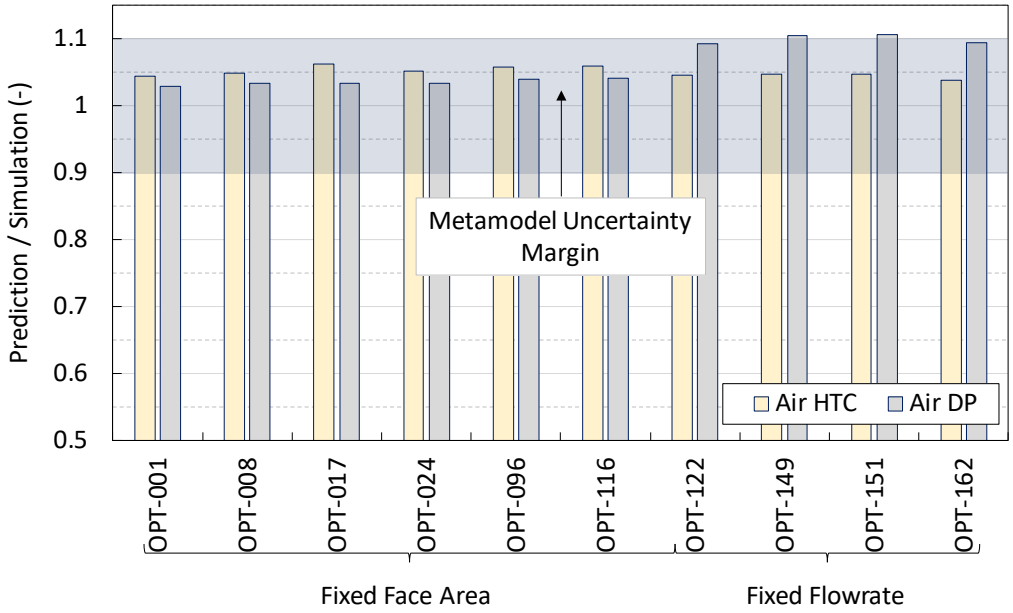

Figure 38. Metamodel Verification for Selected Optimum Designs.

This was anticipated since the dog-bone fin has a lack of surface area and lower fin efficiency; to maximize the heat transfer coefficient, the minimum free flow area must result in the highest flow acceleration possible. The dog-bone design

fortunately offers less flow resistance; therefore, one could obtain relatively low pressure drops at higher air velocities enabling achieving higher thermal performances.

Other differences in design that had a relevant impact on performance were fin width and fin density. The latter was primary responsible for the trade-off shown in the Pareto fronts. For the designs with variable flow rate, the air velocity played an important role as well. Other secondary design parameters included the number of louvers, which didn't seem to affect the results considerably.

The number of circuits was increased to satisfy refrigerant pressure drop constraints; the optimum designs had at most *30% less refrigerant pressure drop than the baseline*. If using the *split-merge* circuiting, the optimum designs had *71% to 78% joint reduction*; with *conventional serpentine* circuiting, however, this range was reduced to *50% to 60%.* The total internal volume of the optimum designs was approximately 5% less than the baseline, indicating marginal potential for charge reduction.

5.2. Benchtop Testing

Benchtop testing was conducted in parallel with much of the computational analysis and optimization tasks to select appropriate materials and evaluate joining methods in preparation for prototype development. Tasks included:

- **Assessing proper material selection.**
- **Identifying the best methods of brazing these structures together to achieve high quality, resilient brazed joints.**
    - **Developing tools to form fin collars.**
    - **Assembling and evaluating various tube and fin structures to determine fin collar fit.**
- **Evaluating brazed joint quality and uniformity**
    - **Joint microstructure analysis**
    - **Torsion, twist, bending, and tearing (peel) tests**
    - **Split-Merge joint assessment**

5.2.1. Materials Selection

The two materials most commonly used for HVAC applications are aluminum and copper due to their relatively high thermal conductivity and low cost compared to

other metals. Given this trend in the industry, an initial analysis was conducted to evaluate the baseline HXs and the new concepts using aluminum and copper for both the fins and the tubes.

The fin material was more sensitive to the performance since the thermal conductivity is crucial for obtaining high fin efficiencies. Copper fins can increase the fin efficiency by approximately 10% (Table 14, Table 15) compared to aluminum fins, however, the overall heat load was marginally changed. The main disadvantage of copper, in general, is the increased weight; it is three times heavier than aluminum. Copper is also significantly more expensive than aluminum, though the pricing differences frequently changes with the market.

The analysis presented in Section 4.2 showed that the Schmidt method did not accurately predict the fin efficiency for the dog-bone fins. However, based on the above analysis, the fin efficiency for the new concepts was expected to increase when moving from aluminum to copper.

In addition to traditional aluminum and copper, there was also an interest in considering non-metal materials for fins aiming, amongst other goals, to reduce fouling, weight, and corrosion resistance. Currently, the most common non-metal materials used in heat exchangers are polymers (Table 16).

Table 14: Outdoor Baseline HX's using Aluminum and Copper.

Parametric Case		Baseline	Case 1	Parametric Case	Baseline
Fin Material	-	Aluminum	Fin Material	-	Aluminum
Fin Conductivity	W/mK	237	Fin Conductivity	W/mK	237
Fin density	kg/m^3	2700	Fin density	kg/m^3	2700
Fin effectivenss	-	0.758	Fin effectivenss	-	0.758
Fin Mass	kg	6.18	Fin Mass	Kg	6.18
Tube Material	-	Copper	Tube Material	-	Copper
Tube Conductivity	W/mK	380	Tube Conductivity	W/mK	380
Tube density	kg/m^3	8900	Tube density	kg/m^3	8900
Tube Mass	kg	6.517	Tube Mass	kg	6.517
Heat Load	W	12.96	Heat Load	W	12.96
Total Mass	kg	12.697	Total Mass	kg	12.697

Table 15: Indoor Baseline HX's using Aluminum and Copper

Parametric Case		Baseline	Case 1	Case 2	Case 3
Fin Material	-	Aluminum	Copper	Aluminum	Copper
Fin Conductivity	W/m.K	237	380	237	380
Fin density	kg/m^3	2700	8900	2700	8900
Fin effectivenss	-	0.81	0.8698	0.81	0.8698
Fin Mass	kg	2.808	9.26	2.808	9.26
Tube Material	-	Aluminum	Copper	Copper	Aluminum
Tube Conductivity	W/m.K	237	380	380	237
Tube density	kg/m^3	2700	8900	8900	2700
Tube Mass	kg	1.096	3.613	3.613	1.096
Heat Load	W	10.24	10.4	10.4	10.4
Total Mass	kg	3.904	12.873	6.421	10.356

The biggest challenges with polymers are the low thermal conductivity and the mechanical strength. Hussein et al. (Hussein, et al., 2017) published a comprehensive review of the literature on polymer heat exchangers with a focus on thermal

conductivity. Carbon based and ceramic fillers are potential candidates to improve polymers' thermal conductivity (Figure 39, Hussein et al, 2017).

a)

Material	K (W/m K)
Carbon black	6–174
Carbon fiber (PAN)	8–70
Carbon fiber (Pitch)	530–1100 (axis)
Carbon nanotubes	2000–6000 (axis)
Graphite	100–400 (on plane)
Graphene	5000–6000

b)

Material	K (W/m K)	CTE (10^{-6}/C)	Density (g/cm^3)
Aluminum nitride	320	4.5	3.3
Beryllium oxide	260	6	3
Boron nitride	320	2.9	2.10
Silicon carbide	270	3.7	3.3

Figure 39: (Hussein et al, 2017): Fillers: a) Carbon based; b) Ceramic

The most important aspect of material selection for development of an enhanced SHX is in improving the tube-fin contact, which is best established using brazing materials. Copper brazing is more technically challenging and requires closer gap tolerances than with aluminum. As such, aluminum was selected for both the fins and tubes.

Table 16: Non-Metal Heat Exchangers

Material (HX type)	Advantages/Disadvantages	Manufacturing
PTFE or Teflon (small diam. tubes)	- eliminated need for conventional tube sheet (Cevallos, et al., 2012) - cooling of acids, partial condensing, evaporative air-water cooling, and water/water heating - not subject to UV degradation	- suspension polymerization - dispersion polymerization
PFA or Perfluoroalkoxy (tubes, coils)	- Good corrosion resistance; not as strong as PTFE at elevated temperatures - not subject to UV degradation	melt-processing technique
PEEK (plate)	- At 100 µm thickness, exhibits high tensile properties exceeding most thermoplastics - excellent creep properties	- injection molding - extrusion methods
PVC (plate)	- can handle airflows with sensible and latent heat exchange - temp (-15 °C to 60 °C) - max pressure 1 kPa	- suspension polymerization - emulsion polymerization -bulk polymerization
PVDF & PP (plate, coils, shell & tube)	- heat transfer between corrosive fluids - PVDF can withstand 600 kPa at 100 °C	- melt, solution and/or film casting - spin coating - injection molding (pp)
Extruded PP Sheets (plate)	- ventilation, humidifying, electronic cooling, wet flue gas, recuperation - sheet thickness from 2-5 mm - Temp -40 to 90 °C	--

Material (HX type)	Advantages/Disadvantages	Manufacturing
Thermoformed Plastic (plate)	- corrosive liquid cooling	thermoforming

5.2.2.Brazing Connection

To assess the feasibility of the brazing connection for the SHX concept, several benchtop brazing tests were conducted. These were done using several different tube types, as outlined in Table 17.

Table 17: Tube Samples for Preliminary Brazing Tests

Sample Reference #	Tube Outer Diameter (OD)	Material	Notes
1	7.2mm	Aluminum	Initial sample
2	8mm	Aluminum	
3	8mm	Copper	Used for testing mechanical (non-brazed) joint

The preferred brazing technology method was similar to that currently used in the Nocolok®[9] process for making automotive aluminum heat exchangers. This manufacturing process has been established for many years and removes any need to re-invent the process. Either cladded tube or cladded fins are needed for bonding during the brazing process, but not both.

By brazing the round tubes to the fins, the tube-to-fin thermal contact resistance of the SHX can be dramatically improved. Also, when brazed, the dog-bone-shaped fin collars do not require an interference fit to the tubes and are thus easier to introduce onto the tube. Brazed tube to fin joints significantly increase the structural integrity of the heat exchanger. Joint strength is improved to such a degree that the SHX size could be substantially increased.

The source of the braze alloy was the tube itself, which had an outer layer consisting of a 4000-series aluminum-Silicon alloy. A typical alloy will have about 10-12% Silicon aluminum by mass, but values may be as low as 8%. A common clad layer thickness as part of overall material or wall thickness is 10%.

[9] "NOCOLOK® flux is non-hygroscopic and only very slightly soluble in water (0.2 % to 0.4 %). The shelf and pot life of the flux is therefore indefinite. The flux does not react with aluminum at room temperature or at brazing temperature and only becomes reactive when molten (at least partially molten). The flux leaves a mainly water insoluble residue which need not be removed."

The actual brazing process included several steps to create the sample prototypes, followed by several brazing tests:

Sample making: The tubes were received and assembly, brazing and analyzing tube-fin structures began. A forming tool (also known as T-Drill) was used to make holes with collars in flat fins for insertion by short lengths of clad tube.

Fluxing: Fluxing of the heat exchanger (Figure 52a, b) can be performed using a few methods. One method is mixing the flux powder with isopropyl alcohol. While it is stirred to keep the flux in suspension, the mixture can be sprayed on the part. Another method is to mix the flux with water and have the heat exchanger pass under a waterfall of this mixture. After any fluxing technique with the purpose of depositing a small amount of flux on the part, the part is dried either by using hot air or in a drying section in the furnace. Standard aluminum brazing flux was used.

Brazing: These simple tube-fin assemblies had flux sprayed on and were then brazed under nitrogen atmosphere in a Fisher-Scientific 10-550-58 inert atmosphere laboratory furnace. In the case of an inert gas furnace, Nitrogen is utilized to displace the air around the part, preventing it from oxidizing which would otherwise prevent a braze. Such furnaces are commonly used in the brazing of automotive aluminum heat exchangers.

In order to heat and cool the samples to be brazed at rates similar to a production furnace, a retort box was used. The box allowed rapid heating and cooling by inserting the box into the already hot furnace, and then removing it from the furnace once the appropriate temperature was achieved for cooling. Recommended heating for the Nocolok® process is a minimum of 20°C/minute. Nitrogen gas was conveyed by copper tube into a small stainless-steel retort box to maintain the inert atmosphere around the sample required for proper brazing. Similar atmosphere exists in production furnaces.

When in the furnace for brazing, the temperature profiles consist of a rapid temperature increase up to the point where the flux can melt. The flux removes the oxide layer from the surface of the tube and allows the outer clad layer to properly flow and wet the surfaces to be joined by the molten clad layer. The part temperature continues to rise up to the liquidus temperature of the clad layer, which is the filler metal. Tube-to-fin joints were created as the clad layer flowed to create the required fillets. The creation of the joint fillets was also aided by capillary

action of the gap between the tube and fin. For best practice, this gap was no larger than 0.1mm or complete fillets may not be created if there is lack of available filler metals at that point. The part is best held at the liquidus temperature for a few minutes, depending on part size and how homogeneous the temperature distribution of the furnace is. Afterwards, the part was removed from the brazing chamber or section to a cooling zone where it was cooled down before exiting the furnace.

Initial brazing tests: Several testing iterations were performed with both sets of tubes with varying furnace cycle time, peak temperature, and nitrogen flow rate. Table 18 summarizes these testing conditions. For each test, tube sections inserted into a fin sample were placed inside the retort box, nitrogen was turned on to the retort box, which was purged for several minutes to eliminate air, and then the retort box was placed inside the furnace, pre-heated to 690°C. The samples were left inside the furnace for a set cycle time, then removed from the furnace and air cooled to room temperature.

The first two tests resulted in little or no brazing for both the 7.2mm OD tubes with traditional fins, and the 8mm OD tubes with dog-bone fins, due to leaking of air into the retort that compromised the nitrogen atmosphere (Figure 40).

Table 18: Brazing Tests

Test #	Tube OD (mm)	Furnace Cycle Time (minutes)	Sample Peak Temperature (°C)	Nitrogen Flow Rate (lpm)	Results	Modifications Made
Test 1	7.2	6.5	609	10	No brazing or partially brazed joint	New stainless-steel retort box procured
Test 2	8	6.5	Unknown	10	Dull color, crusty tube surface, no brazing	New stainless-steel retort box procured
Test 3	7.2	6.5	609	5	Good brazing	Fin collar improvements
Test 4	8	6.5	609	5	Good brazing	More tubes and fins added
Test 5	7.2	6.5	615	5	Bad braze profile	Furnace braze profile parameters changed
Test 6	7.2	6	605	5	Good brazing	
Test 7	8	5	609	5	Good brazing	Upgrade to 8 tube and 24 fin sample
Test 8	8	5	594	4	Good brazing	

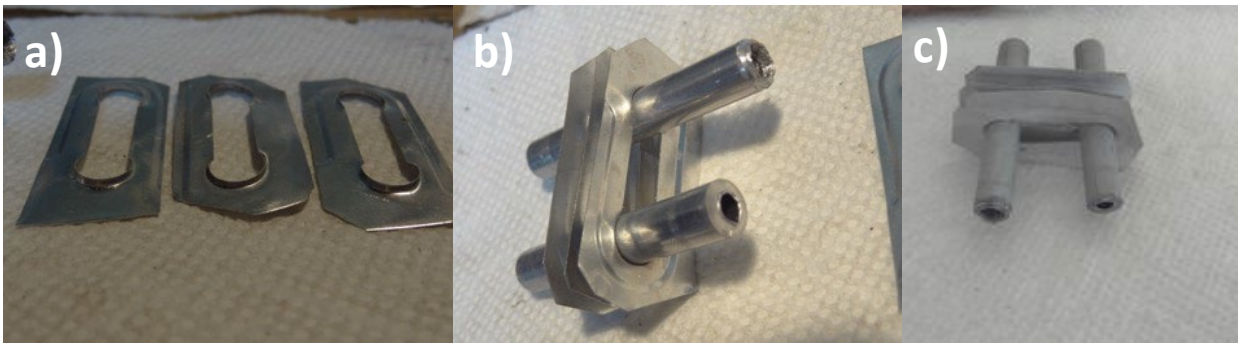

Figure 40: Results of Tests 1 and 2: a) Dog-bone collars; b) Sample with bad braze; c) Sample with bad braze.

Tests 3 and 4 with the new stainless-steel retort box (Figure 42a, b) resulted in successful brazed joints as shown in Figure 41 and Figure 42c. Microsections of brazed joints reveal good brazing had occurred, seen below in Figure 41b and Figure 41c.

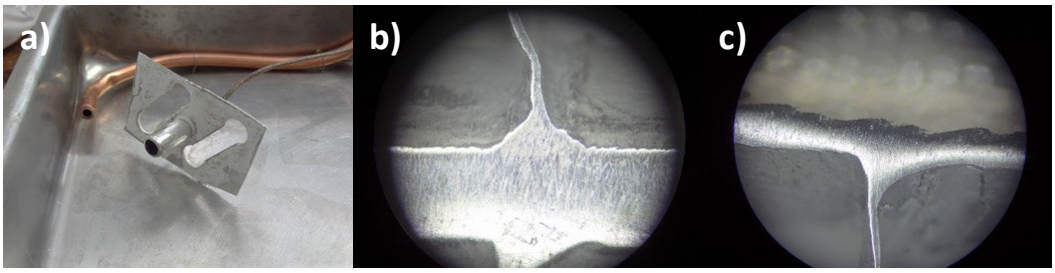

Figure 41: Results of Test 3; a) Sample tube-fin assembly in steel retort; b) and c) Microsections showing good brazed joints

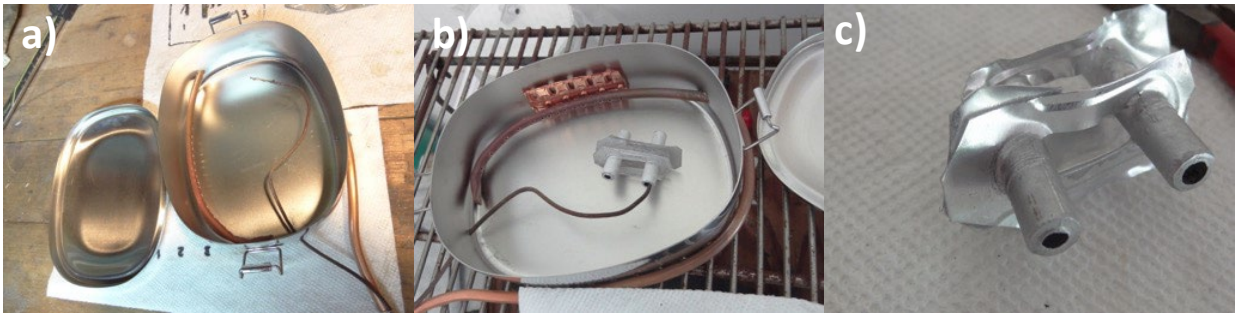

Figure 42: Result of Test 4; a) New stainless retort; b) Fluxed sample in retort ready for brazing; c) Resulted in good braze joints tube with nitrogen feed

Test 5 incorporated further work on improving the fin collars for the 7.2mm tube. Fins for the 7.2mm tube (Figure 43a) were made and small test sections built (Figure 43b). Furnace braze after fluxing (Figure 43c, Figure 44a) provided a homogeneous and sturdy braze joint (Figure 44b, Figure 44c). The sample was cut in half to inspect joint quality (Figure 45).

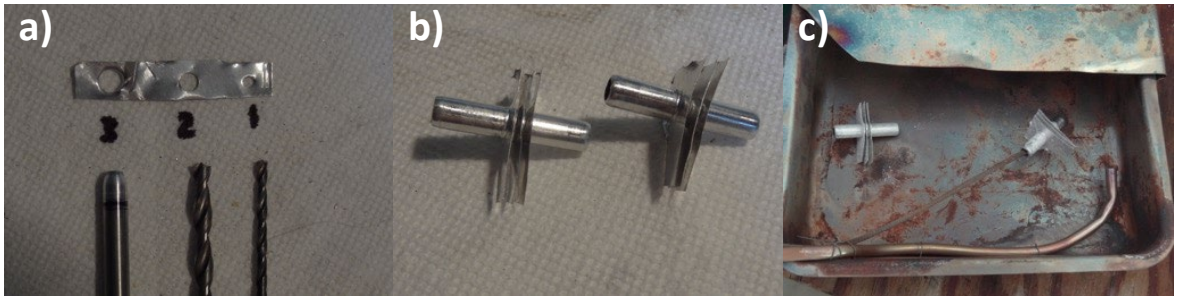

Figure 43: a) Tool making for 7.2mm fin collars; b) Small test sections built; c) Fluxed assembly prior to brazing

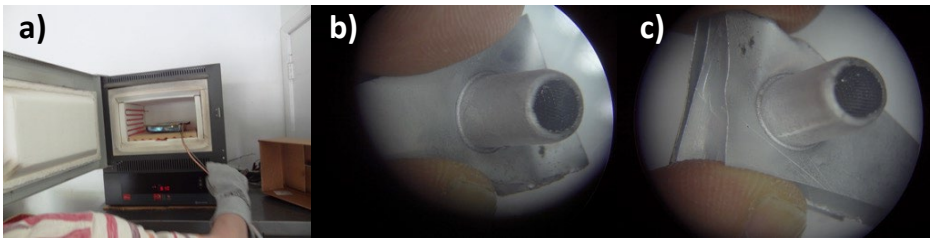

Figure 44: Result of Test 5: a) Inserting a retort into furnace; b) Good brazed joint; c) Another good brazed joint

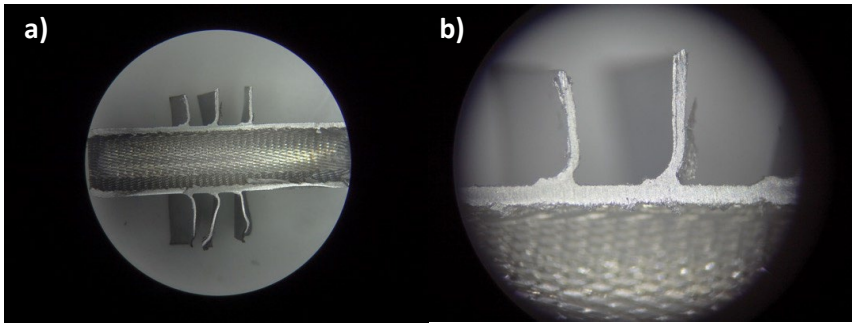

Figure 45: a) Cut in half to observe joint quality; b) Cut out zoom to see joint quality.

An early furnace brazing profile for Test 5 is shown in Figure 46. Part temperature reached 577°C after 5 minutes then the phase-change where the clad alloy melts can be seen as a flat line, and then the part peaked at 615°C. The part spent two minutes over 590°C.

This early braze profile was not ideal since the part temperature was too high and the part was at that high temperature for too long. The liquidus temperature of the 4045-clad alloy is in the range of 574-599°C. When parts are kept at too high of a temperature and too long, silicon from the clad alloy can erode the base metal in a process called silicon erosion, and pinholes can occur. Therefore, with every subsequent test, the furnace braze profile parameters were changed to reduce the temperature and also reduce the time spent above 590°C.

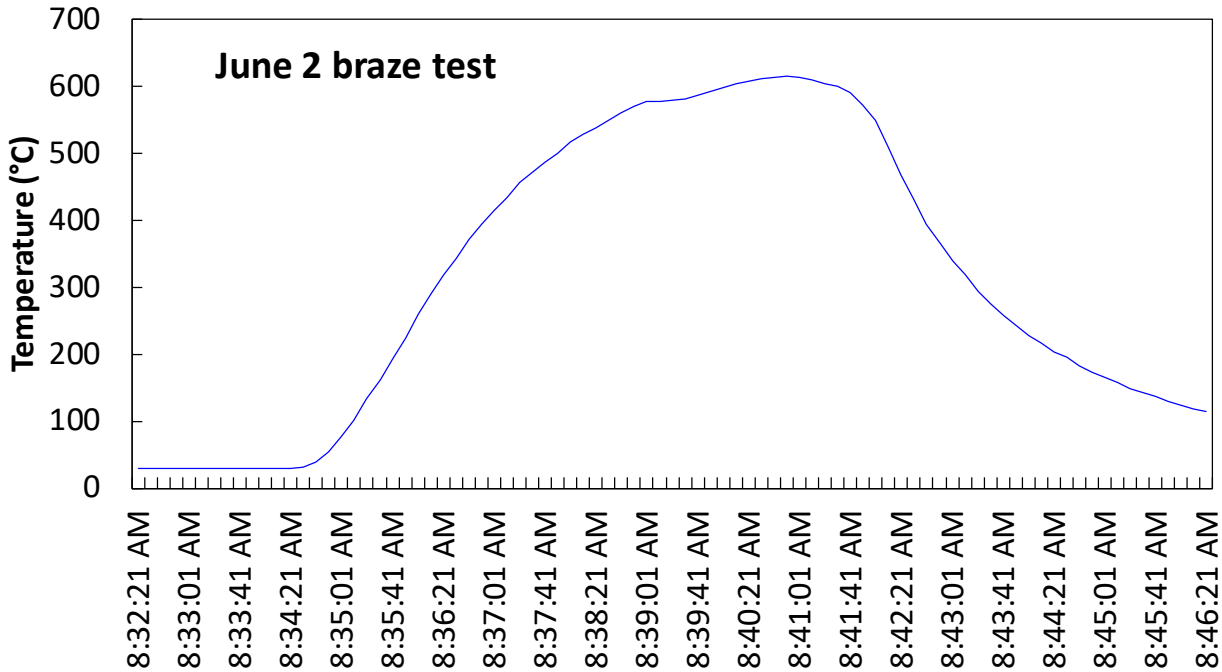

Figure 46: Furnace brazing temperature profile- 06/02/2017

For Test 6, samples with more fins were assessed (Figure 47a) and very good brazing results were produced repeatedly (Figure 47b). A preliminary analysis of microsections showed very good joints (Figure 47c, Figure 48). Further microsection analyses were conducted and are detailed in the Microsection Analysis Section.

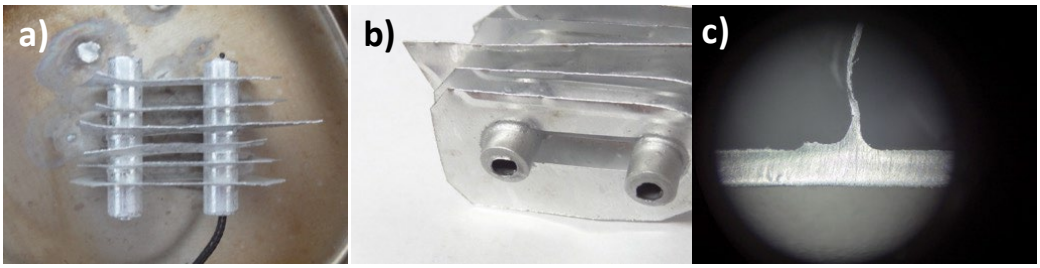

Figure 47: Result of Test 6 a) Larger sample fluxed for brazing; b) Larger sample with good braze joints; c) Microsection of good braze joint, view 1

Tests 7 and 8 focused on the 8mm OD tubes in increasingly large sample configurations. Test 7 first tested 2-tube and 4-tube samples of stacked fins where the fins were stacked with no gaps between them in order to test whether flux would penetrate into the joint even if the stacked collars covered the tube. This test showed that a good braze can be achieved even when all the collars touched each other, covering the tubes and leaving only a small section where the dog-bone is

open for the flux to penetrate (Figure 49a). A good braze resulted with good fillets inside each fin (red arrow) (Figure 49b).

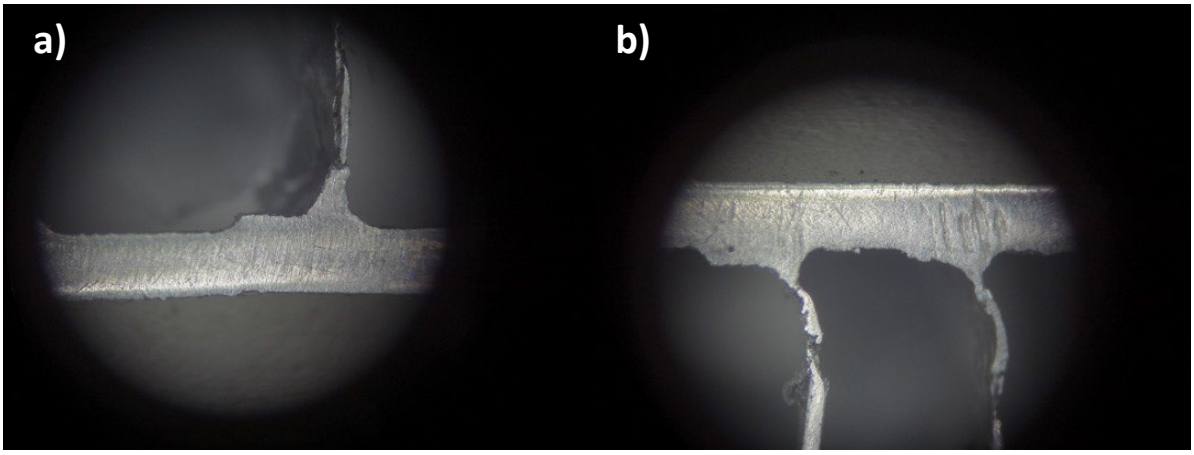

Figure 48:Result of Test 6 a) Microsection of good braze joint, view 2; b) Microsection of good braze joint, view 3

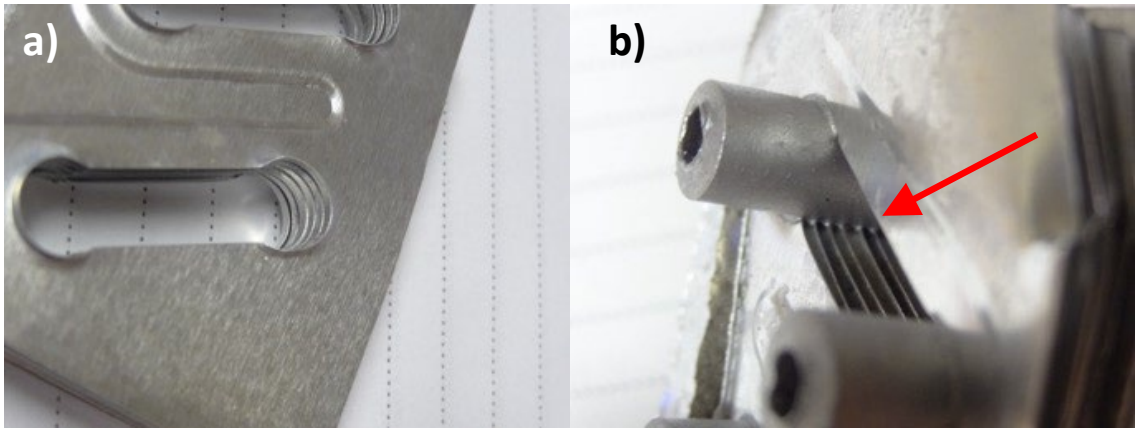

Figure 49: Result of Test 7; a) 3186- Stacked fins in sample assembly; b) 3207-Good brazed joints with fillets inside each fin.

Larger samples were then produced for Test 8: 8-tube with 24-fins sample (Figure 50). The braze profile was further improved to the part having maximum temperature of 594°C and only 30 seconds above 590°C (Figure 51).

Figure 52c shows the nice fillets formed around each tube during Test 8. A closer look revealed nice fillets deep inside the core. Flux residue is inert under 400°C, but for aesthetic reasons, if removing the white flux residue is desired, the part can be washed for a clean look as shown on bottom photo. For larger size heat exchangers, multiple tube bundles can be introduced into a single fin stack as an example. These multiple tube bundles were part of the circuitry design for a specific application.

Figure 50: Result of Test 8: a) Sample with 8 tube-24 fins prior; b) Good braze joints; c) Good braze joints across

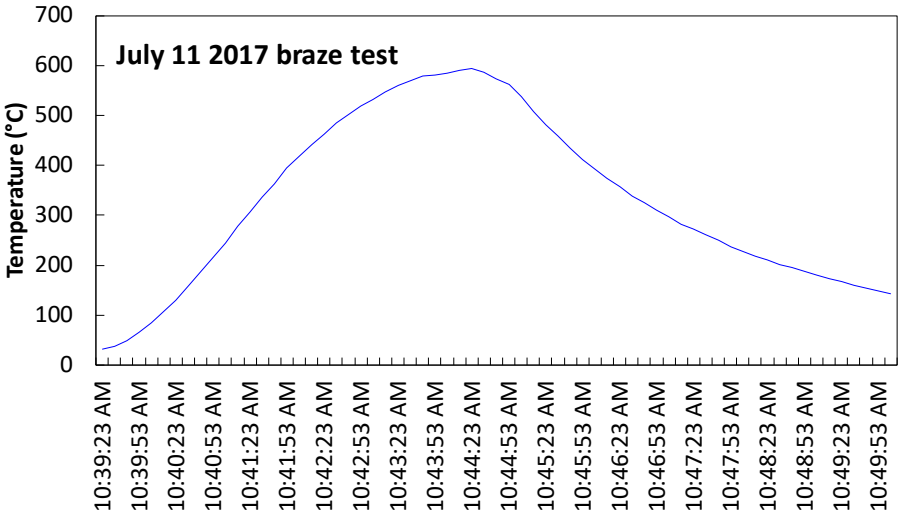

Figure 51: Furnace brazing temperature profile

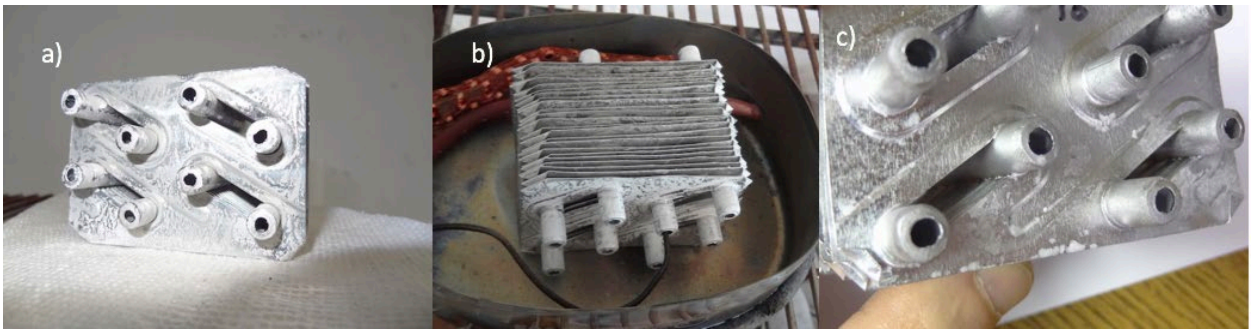

Figure 52: Heat Exchanger Flux a) Front view; b) Top view; c) Fillets

5.2.3.Microsection Analysis

After the successful brazing of the serpentine tubes to the dog-bone fins, the connection formed during Test 8 was examined at the microsection level by UTRC. UTRC provided evaluation of the braze connection by taking high resolution images

of microsections of a conventional non-brazed serpentine heat exchanger and the samples provided by HTT using the brazing method described in the Brazing Connection section. Without the braze (Figure 53), there was a visibly clear gap between the tube and the fin, which can be larger than the fin thickness. In the brazed version (Figure 54), on the other hand, these gaps were completely filled. Moreover, for points where the gap between the fin and the tube were large, the brazing material could bridge them regardless of the distance.

Lastly, the braze established a much wider contact area (Figure 53a and Figure 54a) that extended from beyond the tip of the "pseudo-collar" to the tip of the filling between the tube and the "elbow" of the "pseudo-collar".

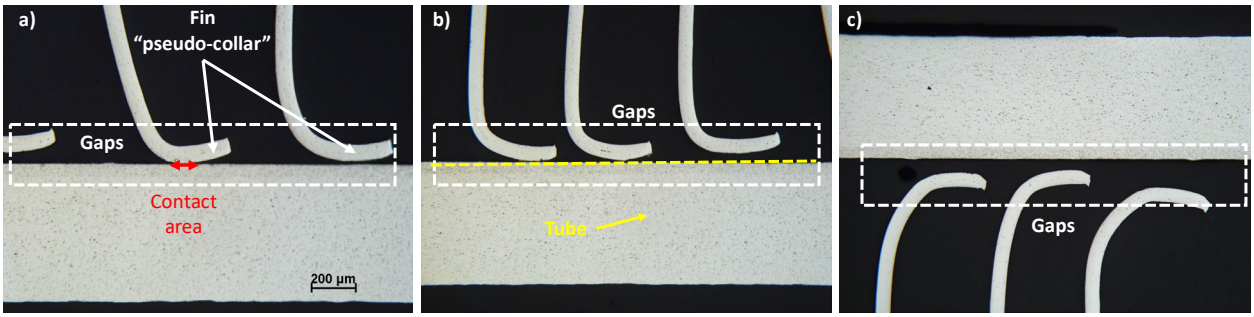

Figure 53: Microsections of conventional non-brazed serpentine tube and dog-bone fins.

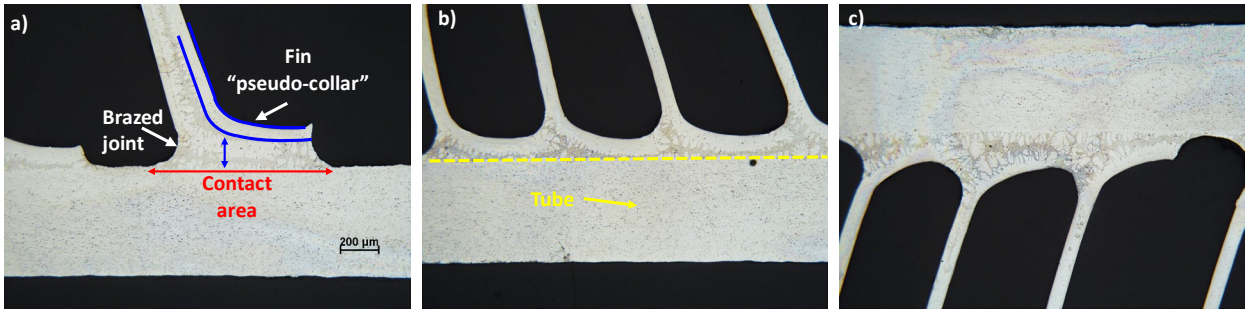

Figure 54: Microsections of brazed serpentine tube and dog-bone fins.

5.2.4.Torsion, Twist, Bending and Tearing Benchtop Testing

The successful 8 tube -24 fin brazing samples presented at the end of the Brazing Connection Section underwent some basic torsion, twist, bending, and tearing (peel) tests to further evaluate their quality. The result of a torsion test is shown in Figure 55. The sample assembly (Figure 55a) was put under torsion load as shown in Figure 55b with results of the test in Figure 56a. The tear test is shown Figure 56b.

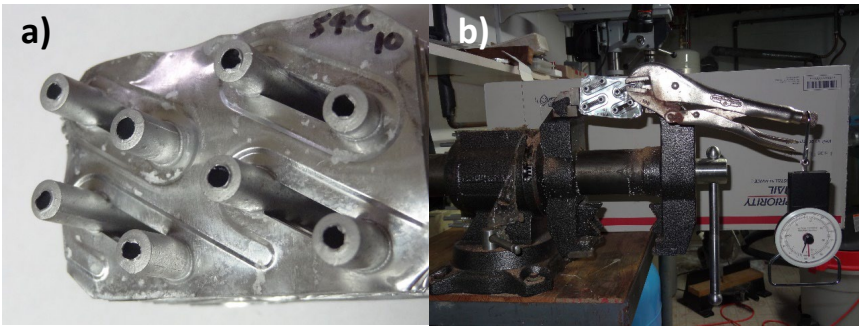

Figure 55: a) 8 tube- 24 fin assembly prior to torsion testing; b) 8 tube-24 fin assembly in torsion test

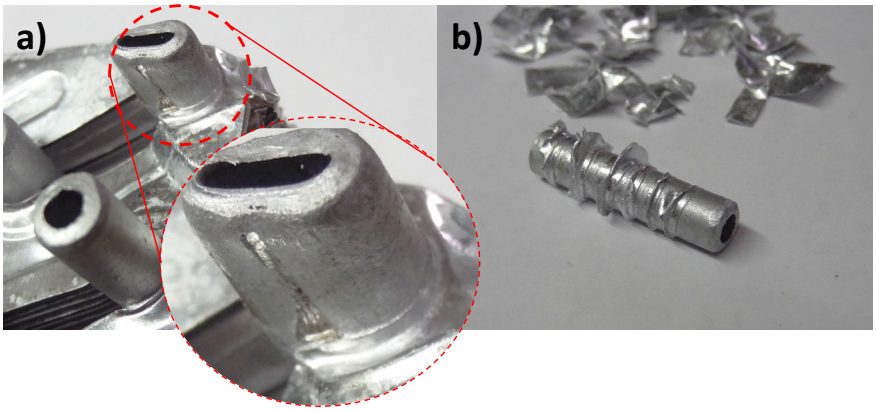

Figure 56: a) Assembly after torsion test showing no damage; b) Tear test result on a brazed tube-fin assembly to brazed joints.

This test showed:

1. **The force required to twist one tube brazed to 24 fins was quite high (2kg x 203mm is 0.406kg-m or 2.93lb-ft).**
2. **In comparison, the baseline serpentine heat exchanger tube would twist in the core without much force (not measurable) and would not twist the fins.**
3. **Although the tube was twisted from one end only, it twisted all 24 fins to the other side evenly, showing all the fins were brazed well to the tube.**

The test piece could not be bent or twisted by hand at all while holding it from both ends and felt like a solid even though it measured only 75 x 48 x 45mm. (75 x 48mm is the fin dimension.) The sample test piece had 24 fins over 45mm, thus the fin density was a typical 14fpi. The assembly showed no damage to any brazed joints under torsion testing. In further testing by twisting and bending, the assembly behaved like a solid without any deformation, unlike the baseline case (regular serpentine heat exchanger) where tubes could freely move in the collar.

Tear testing indicated no damage to any brazed joints; only the fins were torn off in pieces, but still adhered at the brazed collar-tube interface (Figure 56b).

5.2.5.Split-Merge Joint Testing

Once the split-merge concept discussed in the Split-Merge Joint Section had been analytically evaluated and found to be plausible, UTRC manufactured samples to undergo basic testing to ascertain whether they were truly a feasible design. For the initial samples, the split-merge connections were manufactured on U-bends which were then brazed to the serpentine circuits. Although this resulted in an effective larger number of joints, it served for validation purposes; in the final design there were no U-bends and the holes were drilled directly onto the serpentine elbows.

UTRC successfully drilled the holes on the U-bends using Electrical Discharge Machining (EDM) (Figure 57). The advantage of this process was avoiding contaminating the tube with debris that would have been produced using mechanical drilling. Avoiding this contamination was critical considering that, if successful, this method would be applied to fully formed serpentine channels, making it much more difficult to clear the inside of the tubes. Furthermore, from a manufacturing perspective, limiting the number of post-processing cleaning steps is critical to developing a low-cost solution.

Figure 57: Split-Merge holes using EDM

Upon receipt of the sample U-bends produced by UTRC, HTT successfully brazed the tube connections to the U-bends (Figure 58). These connections were later brazed onto the HX samples and manifolds upon completion.

Figure 58. Split-Merge brazed connections

Initial braze tests were done with U-bends having a 7/32" (5.55mm) hole to accept a 7.9mm OD tube that went over the U-bend (Figure 59). The straight tube had to have its end modified to follow the U-bend contour where they meet. A special jig was built to hold the two parts in place for brazing.

Tube goes OVER the hole | Braze jig required for brazing | Post-brazed part

Figure 59: Initial Braze Tests.

Due to the difficulty in holding the straight tube in place during brazing, another method using smaller diameter straight tube was investigated, which is more suitable for production. A smaller hole of 5/32" (3.96mm) was made and then expanded to form a collar to accept a 7/32" (5.55mm) tube, using a Flowdrill forming end tool (Figure 60). When inserting a straight 7/32" tube into the hole that now has a collar, the straight tube sat firmly in place. This method eliminated the need for reforming the straight tube end and the need for a braze jig during brazing.

Due to the limited number of available U-bends, initial split-merge braze tests as described above were performed on a straight 7mm OD tube section (Figure 60).

Finally, the method was employed on actual U-bends; 4 brazed split/merge parts were sent to UTRC for mechanical testing and metallography analysis (Figure 61).

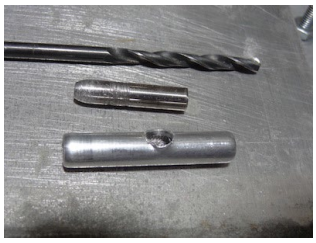

Drill and expand hole creating a collar.

5.55mm tube into the 7mm clad tube + braze ring

Brazed part, no jig required

Figure 60: Second Method: Smaller Diameter Straight Tube.

Parts assembled before flux and braze

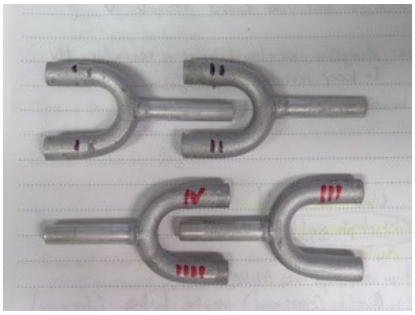

Brazed parts

Figure 61: Final Split-Merge Samples.

UTRC then focused on assessing and mitigating the risks associated with the split-merge joints. The plan involved producing SEM or CT scan samples (Figure 62) to characterize geometry, study the quality and the integrity of the joints, and, finally, model the strength using Finite Element Analysis (FEA). UTRC made holes using EDM process on sample U-bends, which were further brazed by HTT. UTRC performed the mechanical testing on these initial samples, in addition to FEA simulation on the split-merge joint, for validation of the FEA model.

UTRC performed FEA analysis on the split-merge joint (Figure 63) for different loads and stress types. The investigation was limited to an arbitrary section, and traction (Figure 64a), compression (Figure 64b) and angular momentum (Figure 64c) were simulated.

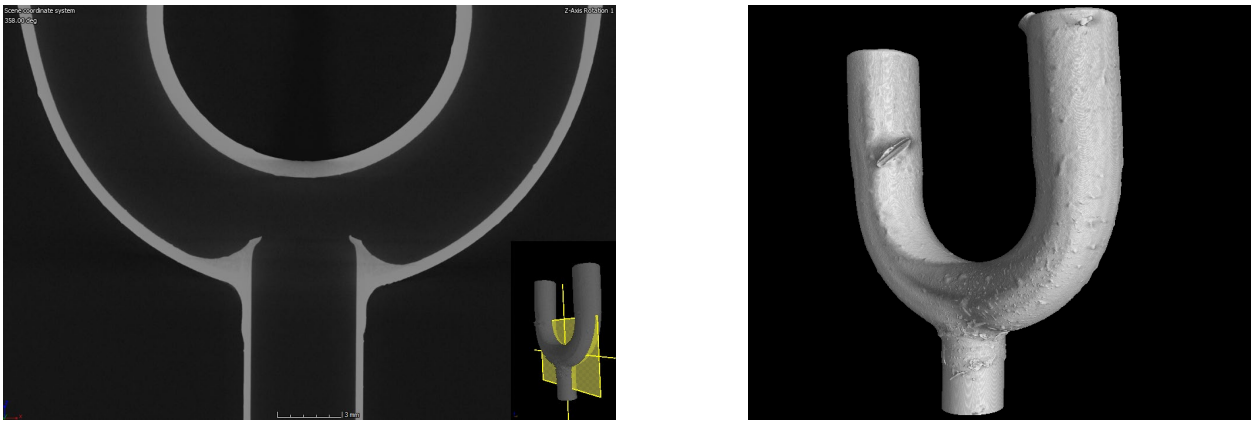

Figure 62: Split-Merge Joint CT Scan.

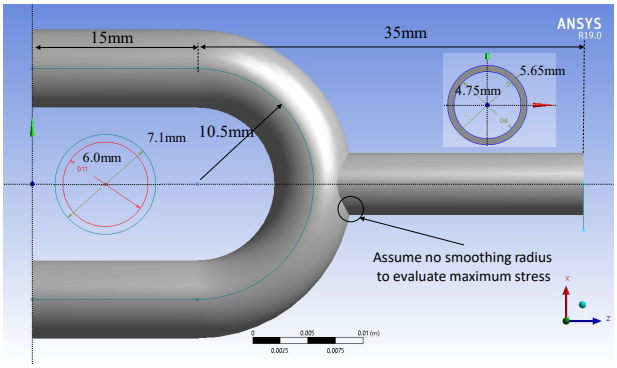

Figure 63: Split-Merge Joint Model.

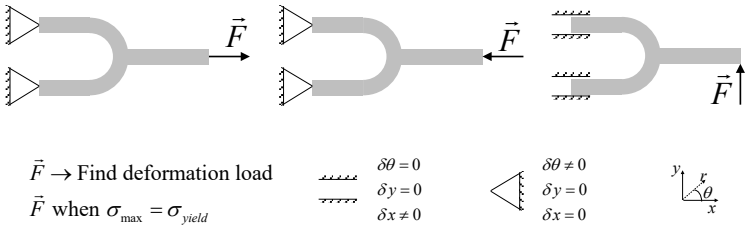

Figure 64: Analyzed cases: a) Traction; b) Compression; c) Angular Momentum.

The results for Yield Strength (Figure 65) showed that in order to deform the joint, a relatively intense force of more than 50N in compression mode was required. For momentum, the force required to deform was significantly smaller, as expected. These analyses were merely hypothetical since realistically, it is unlikely the joints will be under loads of this type. Furthermore, the joints were to be part of the coil, which had higher structural rigidity and additional supports. This mechanical analysis served to provide confidence of the strength of the proposed new joint.

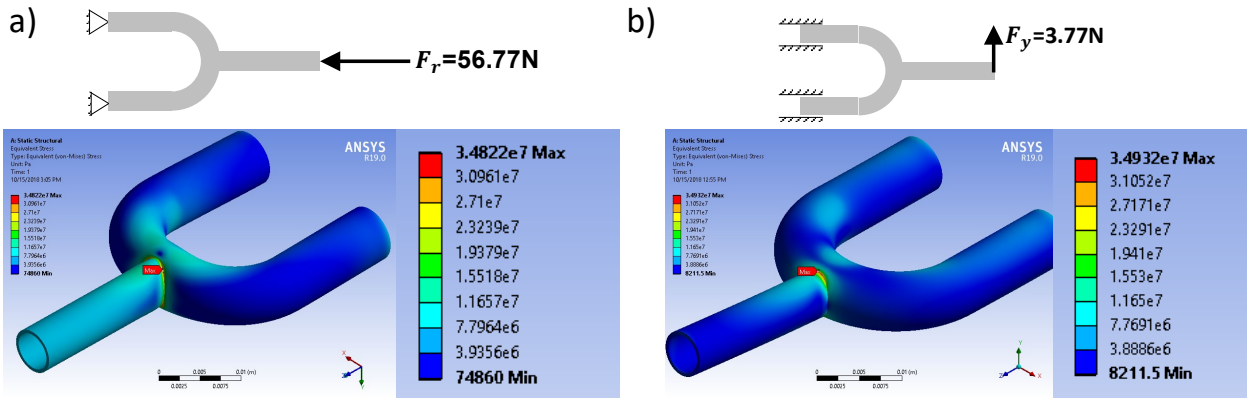

Figure 65: Yield Strength Analysis: a) Compression; b) Angular Momentum

Similar analyses were carried out for the modified split-merge joint. Considering the weakest resistance to angular momentum load, the modified version was expected to be at least 7 times stronger than the original.

6. Enhanced Serpentine HX Prototype Development

Following the initial computation analysis and benchtop testing, and confirmation that the general approach would work, sample HX prototypes were designed and constructed to evaluate the SHX concept and the feasibility as a full HX assembly. The prototypes were constructed concurrently with the optimization studies detailed in the Optimization Section due to time constraints, with some modifications described in the Prototype Construction Section, and together constituted a thorough evaluation of the potential designs.

6.1. HX Optimization Design

Design of the prototype HXs considered four key factors: fin concepts, dog-bone cut gap, variable airflow rate, and alternative serpentine circuiting. The first factor to be considered in the prototype design selection were the fin concepts. The optimization problem discussed in the Optimization Section focused on all louver fin concepts given its higher potential for performance improvement since there are no pre-established rules as to the limit on the number of louvers, louver pitch and so on. For this optimization, the louvers were defined by the number of louvers, a discrete variable, and its corrugation angle (which will fall into the conventional range for louvers). The other dimensions such as height and pitch were functions of tube spacing and minimum distance to wall and/or edges. The minimum distance was

assumed to be 1.5mm, however the number was flexible subject to input from the manufacturer.

Fin thickness has an impact on performance (fin efficiency mainly), material consumption and structural integrity. The first was likely the least important considering that conventional fins are sufficiently thin that the efficiency should not be very sensitive to the thickness. Material consumption and, most importantly, the structural integrity, can be decisive. In particular, these dog-bone fins include nearby enhancements that could weaken the fin sheet at a point that stacking and pushing the serpentines through can damage them. At this moment, the thickness will be considered a fixed parameter and equal to 0.1mm. Steps are being taken to increase the fin strength by adding ribs and louver supports, as advised by the fin producer.

Although there is no rigorous constraint on fin density, the brazing process requires enough space to avoid the capillarity effect to pull the clad material further out in the fins brazing them together and blocking passage and louvers. Based on the results of the benchtop testing, detailed in Section 5.2, a maximum limit of 24 fins per inch (FPI) was recommended. This is also consistent with existing practice in the HVAC industry.

The dog-bone cut angle was investigated as the second significant design factor evaluated thoroughly in the Impacts of the Dog-Bone Cut and Gap Section, and it was suggested that the fin effectiveness can benefit greatly from reducing it. However, the penalties on refrigerant pressure drop and the relatively insignificant capacity improvement in the general parametric study suggested that this angle might not be among the most relevant parameters. This parameter was therefore fixed at 120°.

The third factor to consider was the air frontal velocity and variable airflow rate. Typically, HX design aims for equal or smaller face area, and considering that the airflow rate was at least the same as the baseline, it was logical to use the lower bound equal to the baseline. The upper bounds were defined by practical limitations, such as noise for outdoor units.

Although the variable flowrate did not initially result in great improvements, better outcomes may result after optimization. A benefit of evaluating fixed versus variable flowrate is its small computational cost compared to including an additional design variable entirely, which could require changing the Design of Experiments to be

simulated in CFD. Therefore, the two optimization approaches that will be studied are fixed airflow rates and variable airflow rates (equations 19 and 20).

$$
\begin{array}{ll}
\text{Problem 01:} & \text{Problem 02:} \\
\min f_1 = \Delta P_{air} & \min f_1 = \Delta P_{air} \\
\min f_2 = M_r & \min f_2 = M_r \\
s.t. & s.t. \\
\dot{Q} \geq \dot{Q}_{baseline} & \dot{Q} \geq \dot{Q}_{baseline} \\
T_{sc} \geq 0.0K & T_{sc} \geq 0.0K \\
T_{sh} \geq 2.0K & T_{sh} \geq 2.0K \\
\boxed{\Delta P_{air} \leq \Delta P_{air,baseline}} & \boxed{\Delta P_{air} \cdot \dot{V}_{air} \leq \Delta P_{air,baseline} \cdot \dot{V}_{air,baseline}} \\
R_{\text{joints}} \geq R_{\text{joints,goal}} & R_{\text{joints}} \geq R_{\text{joints,goal}} \\
M_r \leq M_{r,baseline} & M_r \leq M_{r,baseline} \\
V_m \leq V_{m,baseline} & V_m \leq V_{m,baseline}
\end{array}
\tag{19}
$$

Where:

$$
R_{\text{joints}} = 1 - \frac{N_{\text{joints}}}{N_{\text{joints,baseline}}} \rightarrow N_{\text{joints}} = \begin{cases} 2 \cdot N_c, & \text{if conventional joining} \\ N_c + 1, & \text{if split-merge joining} \end{cases} \tag{20}
$$

The final factor studied was alternative serpentine circuiting. In the initial analysis, presented in the Fin Design and Optimization Section, OTS evaluated the two possible serpentine arrangements; i.e. the semi cross flow in counter or parallel (Figure 16a) and the full-cross counter flow (Figure 16b). The latter was the most beneficial in terms of least area reduction and thermal performance. The optimization only considered the straight serpentine arrangement.

Following the selection of a serpentine arrangement, tube spacing, and geometry was also considered. The tube spacing had little restriction except that the center-to-center distance for a bent tube needed to be at least three times the outside diameter. Since only straight serpentines were considered, the minimum vertical spacing met this requirement. The horizontal spacing for a 1-row HX had no additional constraints aside from geometrical tolerances. For multi-row HX's, the serpentine had at least one diagonal bend per row (see Figure 16b); therefore, that diagonal distance also met the minimum requirement. The horizontal spacing was better defined as a function of vertical and diagonal spacing, respectively. The row length was an indirect variable based on coil height and face area. Initially only 1.6m

long tubes were found, which was not yet enough to make a single hairpin for an outdoor unit. The tube supplier was able to provide the tube in a continuous coiled form, so tube length wasn't a limitation. Therefore, the tube length was not initially strictly defined.

Defining objective functions can be complex since different optimization problems can result in very different designs. Multiple objectives are desired since a single-objective optimization problem results in a single design, thus potentially missing opportunities. A multi-objective optimization problem is preferred. Typically, multi-objective optimization requires two or more objectives, as the name suggests, however it is preferable to have no more than two simply because it is easier to visualize (2-dimensional Pareto set) and to evaluate the results. Should more than two objective functions, or different optimization problems are desired, then multiple bi-objective optimization problems should be outlined.

A summary of the design space and fixed parameters for the optimization study used to determine a suitable full HX design is presented in Table 19.

Table 19. Optimization Design Space and Fixed Parameters

Design Variable	*Description*	*Unit*	*Type*	*Range*	*Obs.*
D_o	Tube Diameter	mm	Discrete/Fixed	7.1-8	Depends on tube availability
P_t/D_o	Vertical Spacing to Diameter Ratio	-	Continuous	3.0 - 4.0	-
S_d/D_o	Diagonal Spacing to Diameter Ratio	-	Continuous	3.0 - 4.0	-
N_r	Number of Rows	-	Discrete	1, 2, 3, 4	Depends on tube availability
N_c	Number of Circuits	-	Discrete	3, ..., 7	Depends on tube availability
N_t	Number of Tubes per Circuit	-	Discrete	3, ..., 8	Depends on tube availability
N_{ul}	Number of "Upper Louvers"	-	Discrete	3, ..., 8	Per orientation, total: x2
N_{ll}	Number of "Lower Louvers"	-	Discrete	3, ..., 5	Per orientation, total: x2
FPI	Fin Density	in-1	Continuous	14-24	-
u_{ou}	Velocity for Outdoor HX	m/s	Continuous	1.0 - 1.2	Arbitrary upper bound
u_{io}	Velocity for Indoor HX	m/s	Continuous	2.15-3.15	Arbitrary upper bound
δ_f	Fin Thickness	mm	Fixed	0.1	Subject to revision
δ_m	Minimum Wall / Edge Distance	mm	Fixed	1.5	Subject to revision
θ	Dog-bone cut angle	°	Fixed	120	Subject to revision

The constraints were applied to all performance metrics originally established in addition to the number of joints reduction and all other constraints that were

imposed by manufacturing. Air pressure drop and charge were used as objective functions, and a list of the considered constraints is as follows:

- **Heat load (Q): under the same refrigerant input conditions, the optimum HX's will be required to deliver equal or greater heat load than the baseline.**
- **Sub-cooling (T_{sc} – condenser only): it is desired to have some degree of sub-cooling, so a minimum of saturated liquid will be imposed. Note that the baseline, under the defined conditions, has very low sub-cooling, thus under the baseline input conditions it is not expected to achieve significant sub-cooling.**
- **Super-heating (T_{sh} – evaporator only): similar to sub-cooling, the evaporator outlet needs to be in vapor phase, but also aiming better performance. It will be established an ambitious 2K minimum super-heat.**
- **Refrigerant pressure drop (ΔP_{ref}): the sub-cooling and super-heating indirectly tackle the maximum pressure drop, but a minimum pressure drop should be defined as well. In this optimization, the pressure drop will be allowed to vary between 50% lower to 20% higher than the baseline.**
- **Air pressure drop (ΔP_{air}): if considering a fixed flow rate problem, then the pressure drop will be limited to equal or lower than the baseline. If considering variable airflow rate, then the pumping power will be constrained as such that the product of volumetric flow rate by pressure drop must be equal or lower than the baseline.**
- **Joint reduction: the joint reduction must be equal or greater than established by this project's scope: 70% for outdoor and 85% for indoor.**
- **Refrigerant charge (M_r): estimation is very inaccurate, however a very objective way to evaluate it is the total tube internal volume. If the HX's have comparable performance under the same input conditions, then the internal volume will be a direct indication of the amount of charge. In this optimization the internal volume will be constrained to equal or smaller than the baseline. Charge also indirectly represents environmental impact and energy consumption altogether. The less charge, the less amount of potential refrigerant leaked into the atmosphere, which is one of the primary motivations for this project. In addition, the charge reduction reduces the system's overall weight, thus potentially reducing shipping costs and transportation energy consumption. Furthermore, the less charge, the faster the system's response could be under transient conditions, such as cycling (on-**

off). Although none of these are directly evaluated, they are all potential benefits from reducing charge.

- Material (Vm): typically, it is difficult to assess the material cost given the many intermediate processes between raw material to a final product, however measurements such as volume and weight have a direct reflection on natural resources consumed. Considering that aluminum tubes will be used for this optimization, the volume of material will be used as a constraint, which should be equal or lower than the baseline.

6.2. Prototype Construction

As mentioned in the Optimization Section, technical issues with CFD and optimization software caused delays in obtaining an optimized HX prototype design. In the interests of not delaying the schedule further and to obtain more insights on manufacturing and performance, the team proceeded with the HX design described below, which was expected to perform well enough to sufficiently meet the project criteria.

HTT had 7.1mm OD with 1.6m long tubes immediately available, which were used to build a smaller sample HX. For airside validation, the HX does not need to be the actual HX size, nor circuited as the original design. Additionally, the HX needed to fit inside OTS's wind tunnel cross-section. Given the design dimensions and the available resources, a 4 circuit, 1ft x 1.1ft face area HX (Figure 66) was manufactured as a proof-of-concept for manufacturing and airside performance validation purposes. This exercise provided important lessons when moving forward to developing the tools to manufacture additional HXs, in addition to providing a higher level of confidence in the developed numerical models.

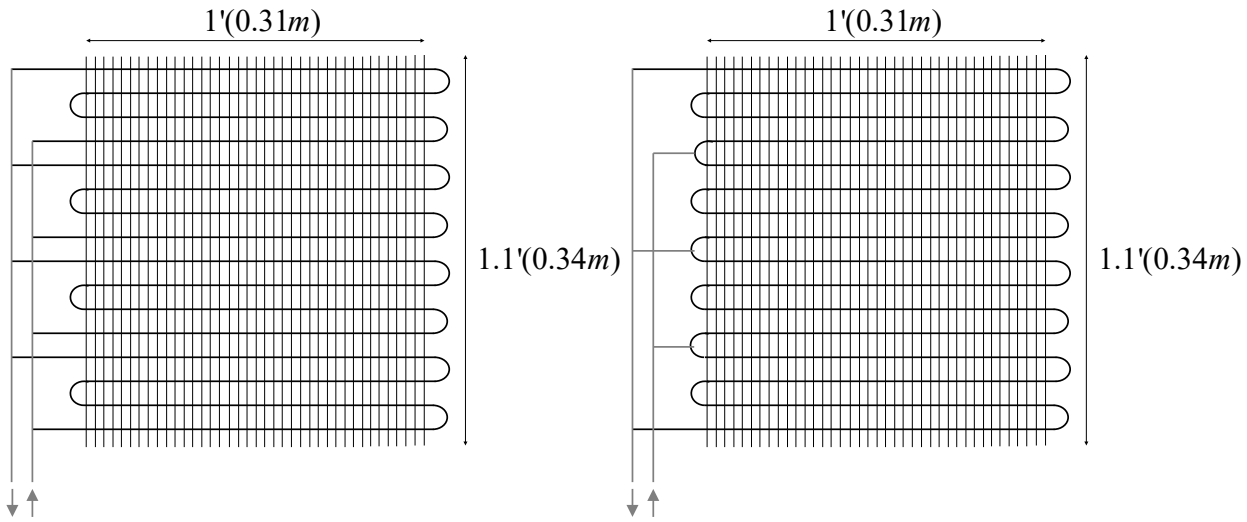

Figure 66. Sample HX Schematic Ideas

To construct the next round of prototype HXs, existing manufacturing equipment was used to produce the serpentine tubes in view of future production, except that straight lengths were used rather than a coiled round of continuous tube. This affected the tolerance on the length of the "legs." 25 serpentines were produced with the legs measuring within 3mm of each other with a final lead length (outside tangent of loop to end of tube) in the range of 397.51mm to 400.05mm. This issue did not exist in the next run when the tube was supplied in coil form, as is customary in production. "U" bends were also produced out of the clad tube material to be used for connections for this interim stage. The U-bends served as serpentine connectors (elbows) for evaluation of the split-merge circuiting approach. For the latter, UTRC provided guidance and offered their manufacturing facilities to make the holes on the elbows that allowed reducing the number of joints by a factor of ~2.

The tubes for the prototypes were 7.0mm OD and 20+ meters long, in hand-wound coils. Later prototypes were fabricated by tube bending and brazing into serpentine coils.

Two of the four samples were circuited using conventional circuiting (Figure 66, left), and two had the split-merge connections (Figure 66, right) detailed in the Split-Merge Joint Section.

The fin tool consists of two dies: one for the louver cuts and the other for the dog-bone cut and collar. Brazeway successfully developed the first as shown in Figure 67. The parts were inspected by OTS and HTT, and both parties determined that the

louver die was satisfactory and could be used to produce full fins for the prototype HXs.

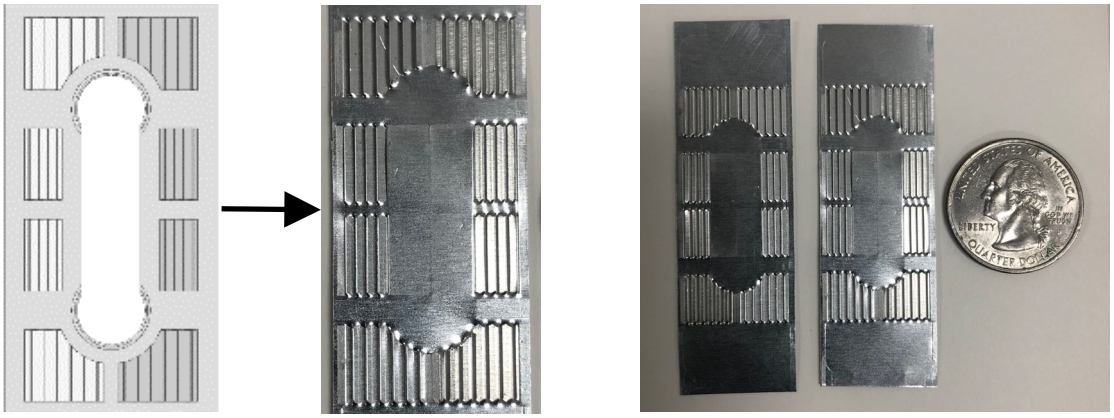

Figure 67. New fin sample with the louver cuts.

The fin material was an H-Temper aluminum alloy, which is sturdy and adequate for the application, however, the collars formed showed some tears. Brazeway successfully built the collar on an O-Temper alloy, but it was too soft and could compromise the integrity of the fins further in the manufacturing process. OTS and HTT agreed that the preferred fin material was H-Temper material. Challenges in getting the H-Temper to work, however, ultimately prevented its use. Brazeway was ultimately successful in utilizing the O-Temper material, though care had to be taken in handling the produced fins and resultant heat exchanger. The fin material temper only affects the making and the handling of the fins. H-temper material is more difficult to form, being harder than soft O-temper. The fin material temper does not affect the brazing of the fins to the tubes. Either O-temper or H-temper material fin will come out of the furnace annealed and at O-temper.

The tears in the collars, though unacceptable for conventional pressure expanded tube-fin joints, were potentially not as problematic in this technology since the clad material filled in the gaps during the brazing process. There was a concern, however, that the clad material would "leak" and flow towards the louvers creating undesired brazed blockages within the louver cuts themselves.

Brazeway also faced initial issues in building the collar with re-flare. This feature allows for the stacking of the fins without a "telescoping" effect and provides the required fin spacing. Because the re-flare was problematic for prototype development, the initial batch of fins were shipped without them (Figure 68).

When Brazeway tried to add the re-flare to the fin, they encountered numerous problems with the tool die manufacturer and with the aluminum material; H14 temper material was deemed too hard for the re-flare resulting in multiple splits (Figure 69a). Brazeway did finally successfully build a round collar without tears on an O temper material (Figure 69b).

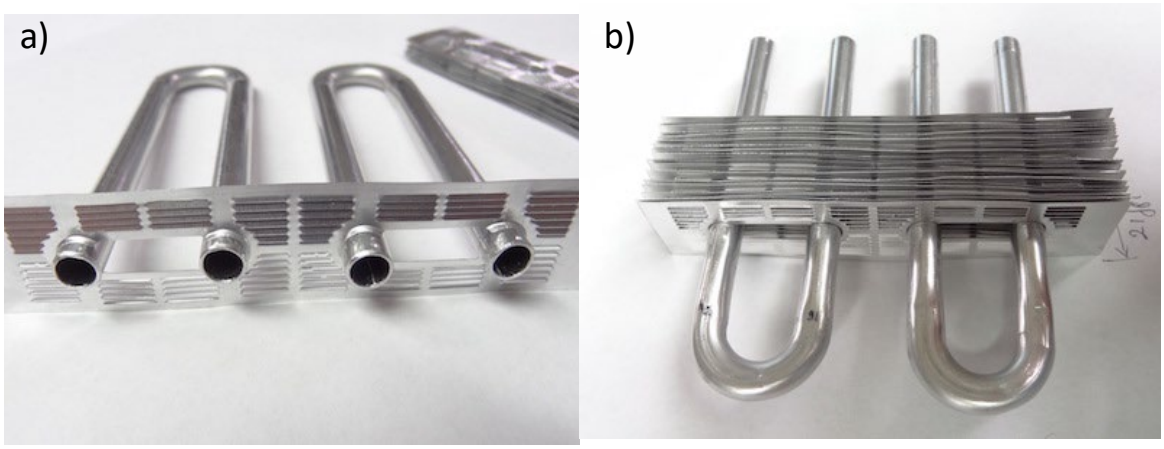

Figure 68: a) Testing the hole size with hairpin tubes; b) 21fpi manually-gapped fin density

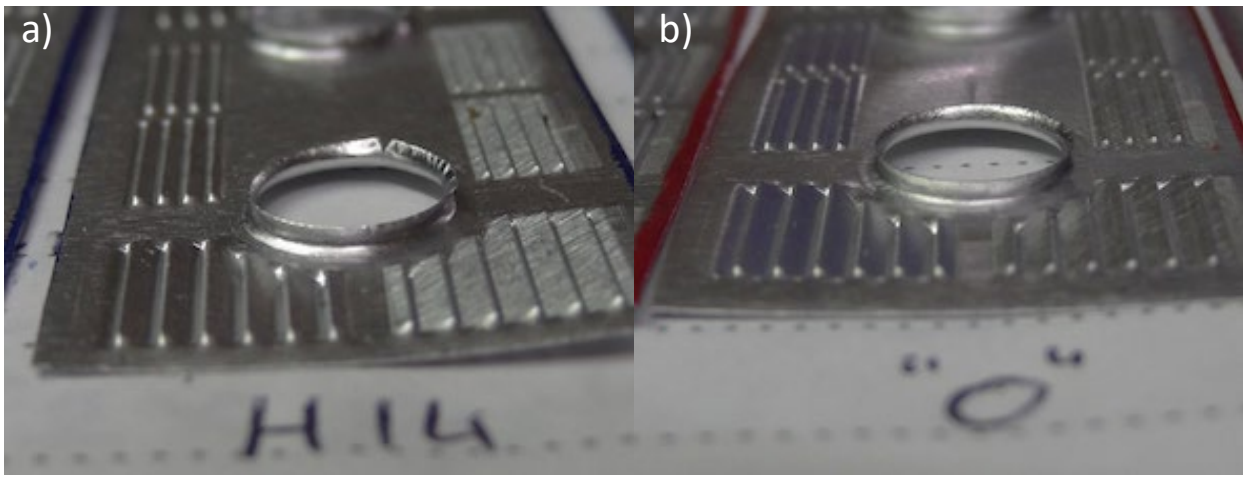

Figure 69: Round collars with re-flare: a) H14 Temper; b) O Temper

In October 2018, Brazeway assembled a full fin for the prototype made on O temper material with the dog-bone cut (Figure 70) and provided plans for one without the dog-bone cut as well. The main concern remains the malleability of the temper that may impose challenges in the assembly without damaging the fins and its enhancements.

In a parallel effort, HTT evaluated the brazing of the newly developed fins. The sample HX assembly illustrated in Figure 71a was tested in the furnace. The fins were successfully brazed onto the tubes (Figure 71b), and no brazing material was observed in between the fins or the louvers.

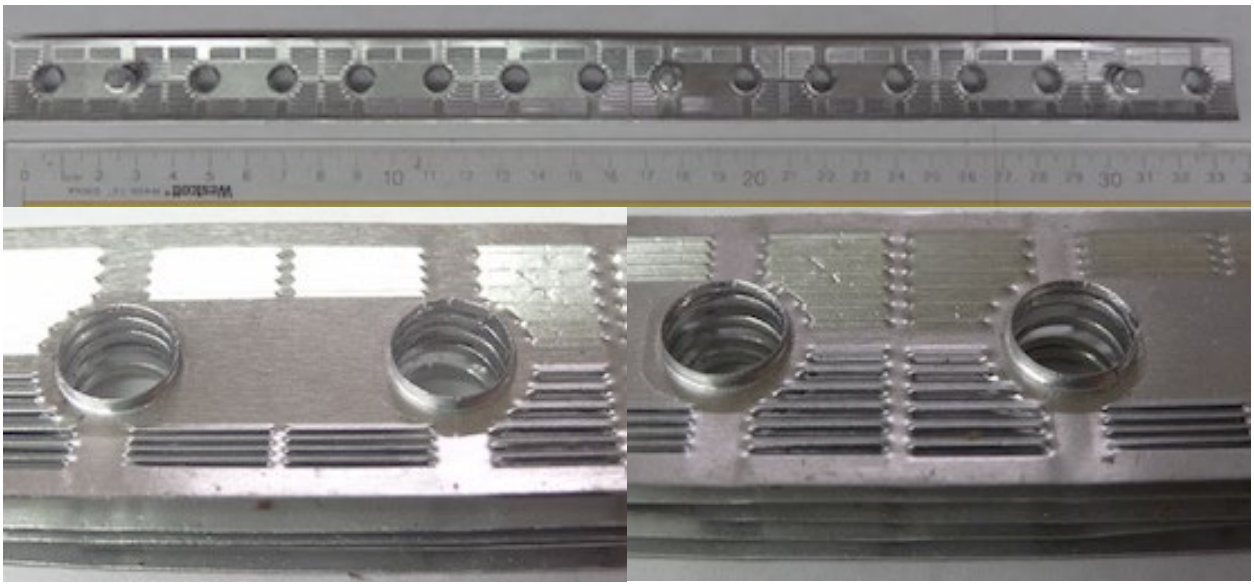

Figure 70: Full fin O temper material.

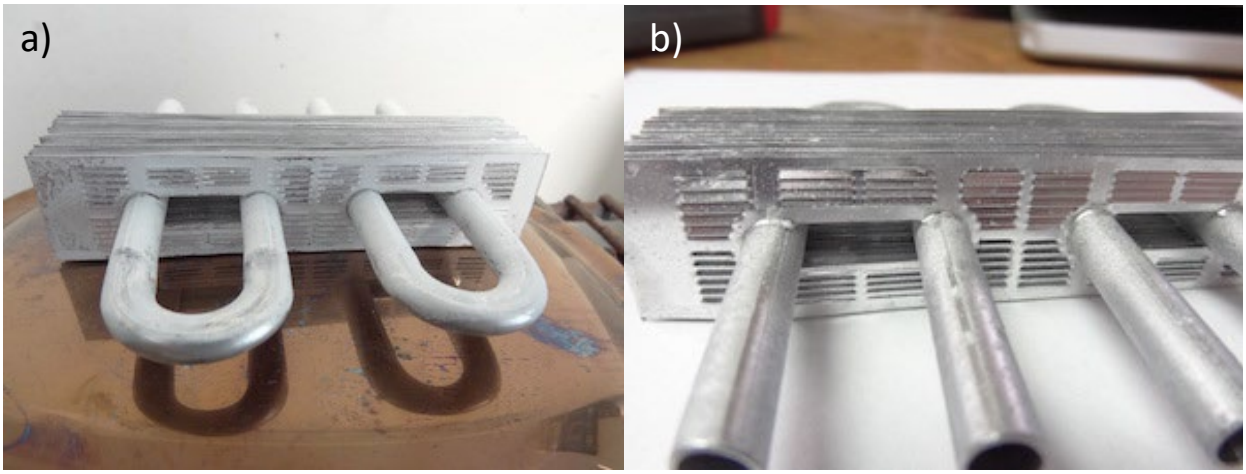

Figure 71: a) Fluxed sample before brazing; b) Brazed sample.

After successfully assembling an O temper heat exchanger without damaging the fin enhancements, Brazeway built the fins and assembled four prototypes (Table 20 and Figure 72a). The targeted fin density for these prototypes was 21 FPI; while three of them resulted in a slightly less-dense finned region, one (HX4) resulted in slightly higher density. The latter exhibited less uniform fin distribution than the first three

due to the lack of re-flare, which allowed some fins to telescope – thus the higher density. The re-flares on the first prototypes, however, enlarged the tube holes resulting in gaps of 0.1-0.2mm (Figure 72b) based on spot inspection over random regions of the prototypes. The last prototype (HX4) did not appear to have any gaps at all.

Table 20. Prototypes Heat Exchanger General Specifications.

Prototype #	# Fins	Finned Length (mm)	FPI	Remarks	Observation	Circuit
HX1	253	320	20.0	Re-flare fin collar	~5% non brazed fins	Conventional
HX2	242	320	19.2	Re-flare fin collar	~5% non brazed fins	Split-Merge
HX3	253	320	20.0	Re-flare fin collar	~5% non brazed fins	Split-Merge
HX4	274	320	21.7	No re-flare	<1% non brazed fins	Modified Split-Merge

All HXs were sent to Arconic for brazing, along with fluxing and brazing guidelines and a recommended brazing cycle. Arconic successfully brazed all four coils without sacrificing or damaging any of them (Figure 73). Due to the gaps noted above, however, 4-5% of the joints did not braze entirely. For HX4, that figure was less than 1%.

For the fin brazing process, HTT built the manifolds and circuits onto the prototypes. HX1 and HX3 were equivalent, and each was circuited using the conventional and split-merge method, respectively, while HX2 was also circuited using the split-merge method (Figure 74).

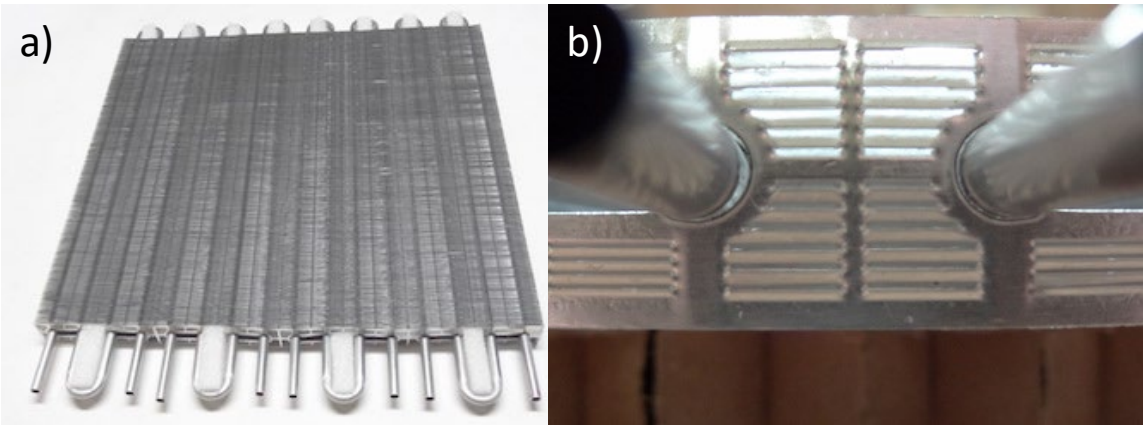

Figure 72: Prototype assembly before brazing: a) Perspective view of HX1; b) Tube-fin gap close in.

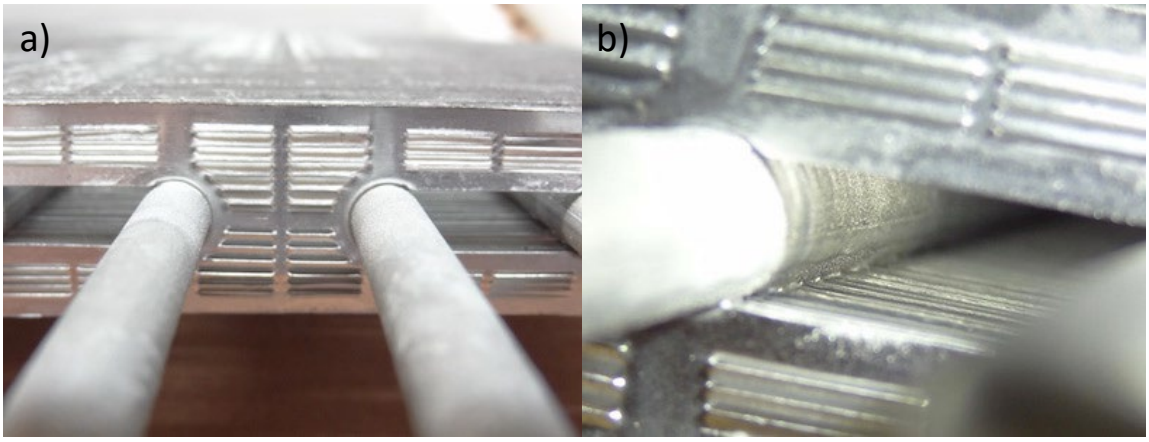

Figure 73: Brazed tube and fin: a) Collar to tube joint; b) View of internal brazed fillet.

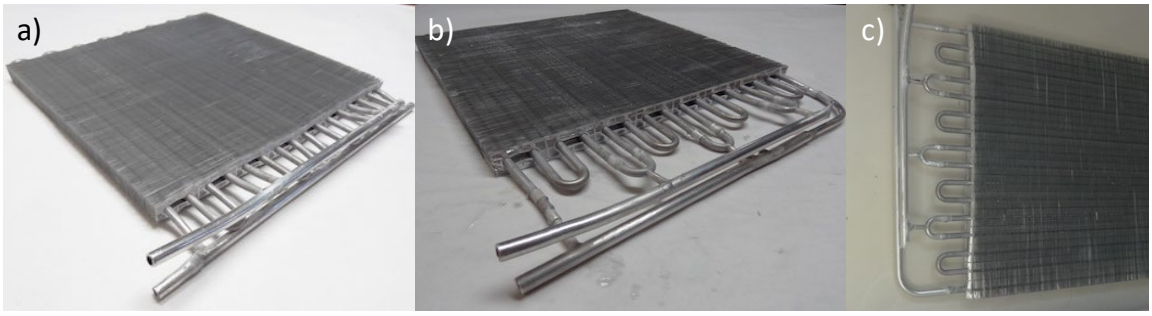

Figure 74. Prototypes with manifolds: a) HX1; b) HX2; c) HX3.

The circuiting for HX4 was determined from the results of the initial performance tests on HX 1-3 discussed in the next section (HX Testing).

6.3. HX Testing

All four prototypes (Table 20) were tested at OTS' temperature and humidity-controlled wind-tunnel (Figure 75), while one prototype also underwent Accelerated Life Tests (ALT), or cyclic testing. The purpose of the performance tests was to validate CFD predictions on airside thermal-hydraulic characteristics, CoilDesigner® prediction of HX overall performance, and to evaluate the differences, if any, between conventional and split-merge circuiting on the fluid (internal) side, particularly in regard to pressure drop. The purpose of the cyclic testing was to predict real-time cycles needed to cause plastic deformation and failure on the split-merge joints and fin-to-tube brazed joints.

Figure 75. View of OTS laboratory, including temperature and humidity-controlled wind tunnels.

6.3.1. Performance Testing

To achieve the objectives outlined above, each HX was tested for three or four air flow rates and two water flow rates, as shown in Table 21.

Table 21. Performance Test Matrix for Each Prototype HX.

Air temp.	Air velocity	Water temp.	Water flowrate
°C	m/s	°C	g/s
25	0.5, 1.0, 2.0, 3.0*	50	100, 150, 200

The tests exhibited a good energy balance between air and water side for all 4 HX's, with less than 1.5% deviation (Figure 76). Additionally, the HX1 and HX3 prototypes, having the same geometry characteristics, agreed well with 2% and 3% difference in

capacity and airside pressure drop, respectively. The latter suggested that both manufacturing and testing procedure have reliable repeatability.

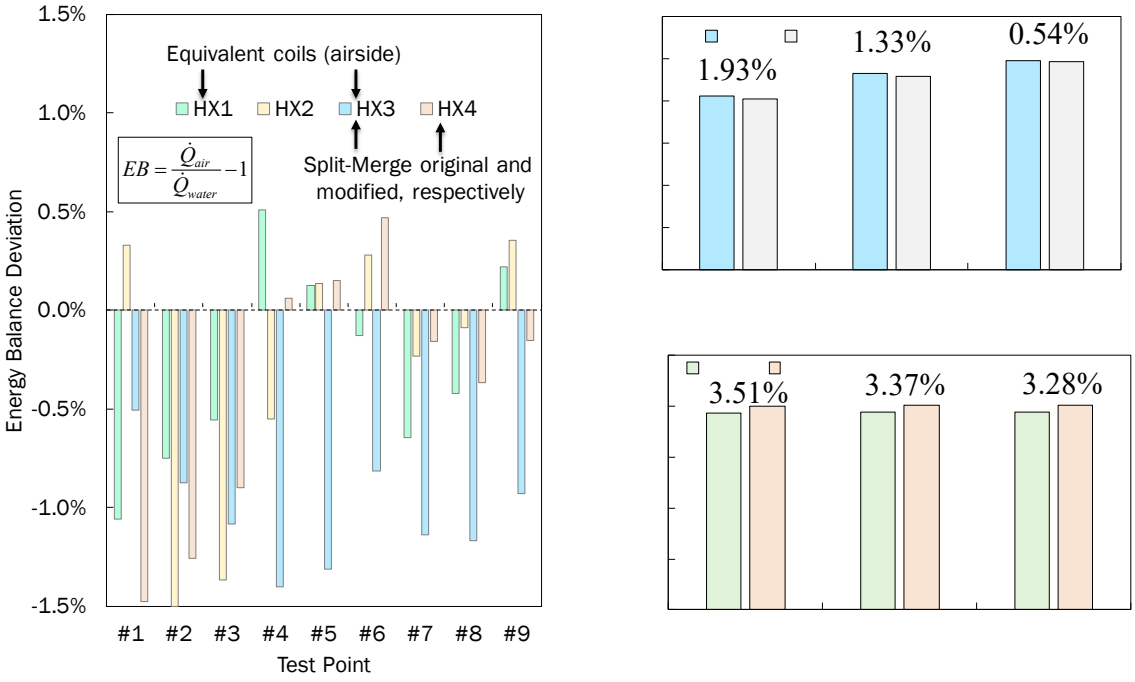

Figure 76. Energy Balances and Repeatability Comparison for Prototype HX Testing

The predicted capacity from simulation results deviated in approximately 20% for HX1 and HX3, while for HX4 the deviation was no larger than 5% (Figure 76). The deviation could not be attributed to numerical uncertainty alone, given that the agreement between numerical and experimental data was not consistent among the coils.

The plots on the left hand-side in Figure 78 show that the predicted airside pressure drop was very consistent with the tested data, with a maximum deviation of 10%, but an average of below 5%. This indicated that the model captured the physics well. For heat transfer, the CFD simulations estimated the airside thermal resistance alone, whereas the reduced data from test results lumped all resistances, including tube wall and fin-tube contact, together with airside. The latter is one of the main reasons why CFD predictions of convective heat transfer coefficients are consistently higher than observed.

For this particular case, the differences considered between HX1 (or HX3) and HX4 were limited to fin density alone, which has weak impact on heat transfer

coefficient. In fact, the CFD simulations for both cases were almost identical. However, the tested data suggested a 20% deviation between HX1 and HX4, with the latter much closer to the predicted values (Figure 77). This difference was most likely due to the number of non-brazed fins, where HX4 had a much higher rate of successful joints than its counterparts, and therefore a much smaller contact resistance.

Although it was expected that if the brazed joints were improved, the predicted performance will be much more accurate, the deviation for HX4 was the same order of magnitude of the margin for heat load improvement from the optimization.

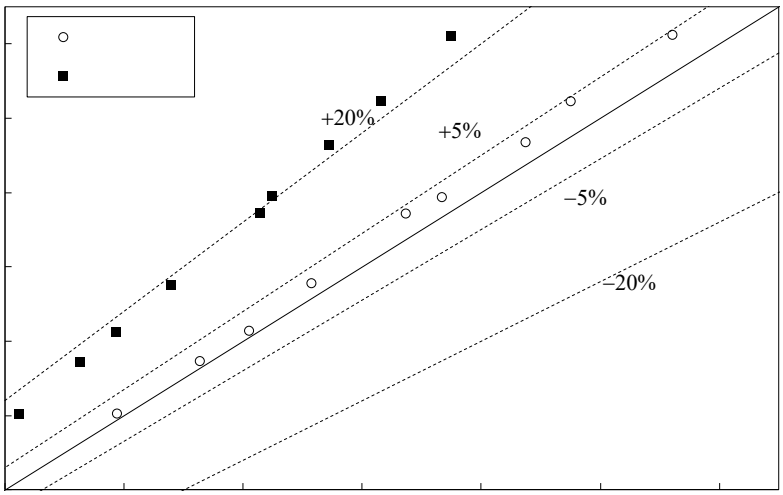

Figure 77: Verification and Validation of simulation results

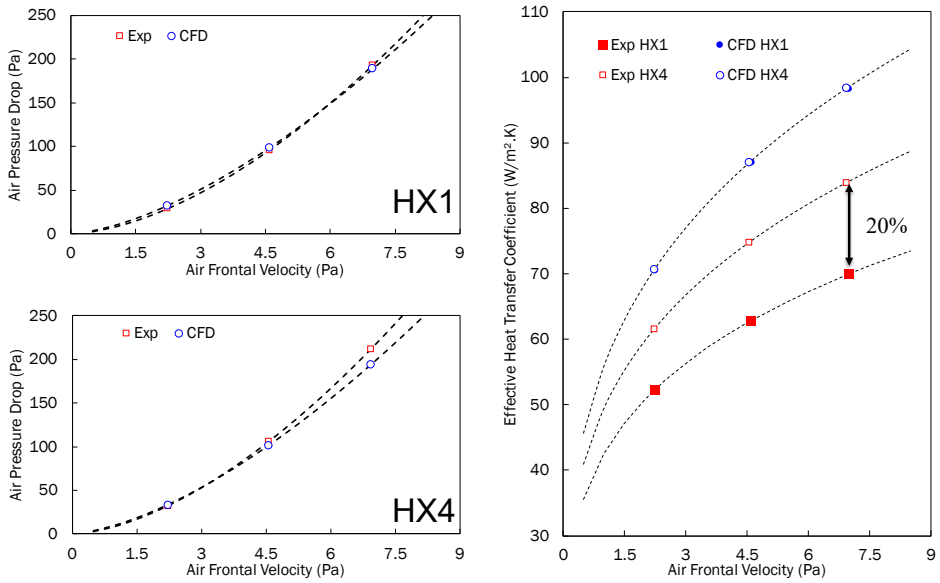

Figure 78: Airside thermal-hydraulic characteristics validation

Another important distinction between HX1, HX3 and HX4 was the circuiting. The first had conventional circuiting with dedicated inlets and outlets for each circuit, while HX3 and HX4 had the split-merge. The difference between the former two was that the modified version had twice as large the cross-sectional area, and a single contraction-expansion neck without a connecting tube. The original split-merge connection resulted in a water pressure drop that was twice as high as compared to conventional circuiting, while the modified version exhibited similar levels of pressure drop as the conventional (Figure 78). Similar results were obtained from simple 2D CFD simulations (Figure 79).

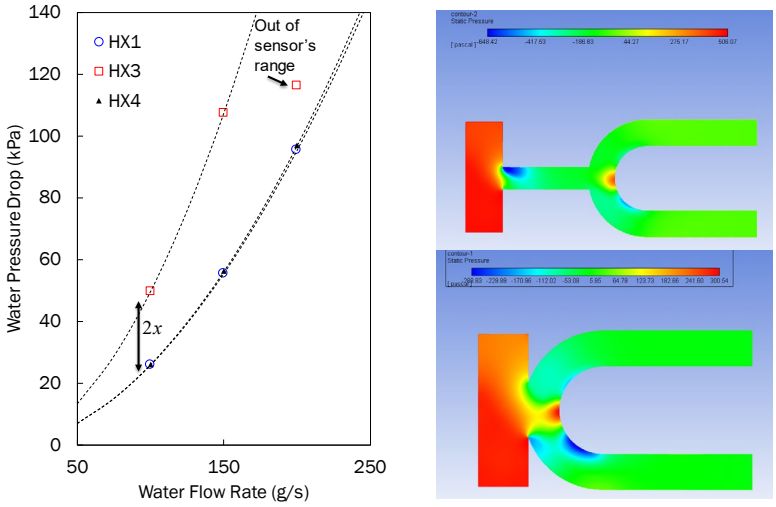

Figure 79: Water-Side Pressure Drop

6.3.2.Cyclic Testing

One of the four HX prototypes underwent Accelerated Life Tests (ALT) to predict real-time cycles needed to cause plastic deformation and failure on the split-merge joints and fin-to-tube brazed joints. The approach consisted of testing a certain number of cycles and use of statistical methods, such as ones described in Meeker et al. (2008) to predict eventual future failures and/or performance degradation.

The test itself was based on a thermal-mechanical cycling test employed by Bowers et al. (2014) on microchannel heat exchangers. The test setup consisted of a heat pump, using R410A at typical operating conditions, connected to the test subject in series and switching flow direction so that the test subject would alternate between evaporating and condensing conditions within a short amount of time (Figure 80, Figure 81). It was anticipated that within a month's timeframe, cycling 8-hours every day, it would be possible to test 10,000 to 15,000 cycles. For every couple of thousand cycles, the HX was inspected for fin-to-tube brazed joint failures, and a normal distribution for metal/brazed joint strain was computed. The latter was measured using strain gauges placed at the weakest locations.

The setup ran continuously between May 20 and July 16, 2019, resulting in a total of approximately 82,000 cycles. Brazed joints on fins and manifolds were monitored using strain gauges placed conveniently at the weakest locations. There were no visible signs of failure or fatigue and the heat exchanger survived completion of cyclic testing. UTRC assisted in providing the correct plots of the signal over time which showed a consistent fluctuation (tube expansion and contraction) around the baseline (zero) (Figure 82), therefore no failure nor permanent deformation is observed.

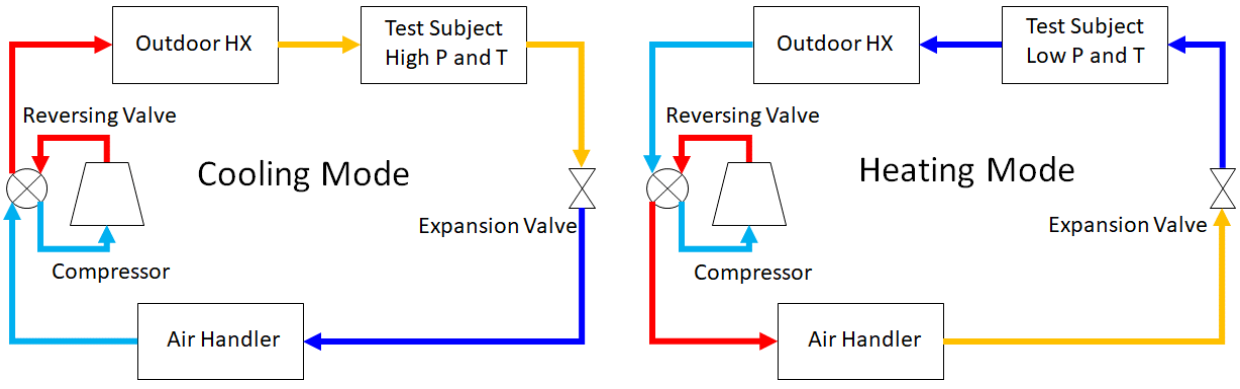

Figure 80: Schematic Diagram.

Figure 81: Test Setup at OTS' Laboratory.

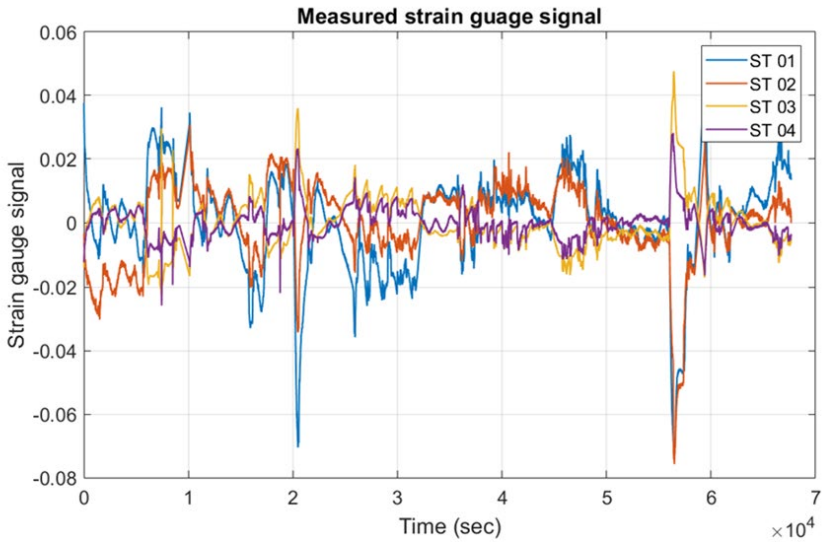

Figure 82: Mechanic Cyclic Tests: Strain Gauge Sensors, Sample Data

After the cycling tests, hot water performance tests were repeated for the prototype HX to assess any potential performance loss caused by fin-to-tube joint failure. Figure 83 shows airside HTCs of the coil before (BC#1 & BC#2) and after (AC#1) cycling tests. As can be seen in the graph, the thermal performance of the coil following thermal cycling is well within the margin of measurement uncertainties.

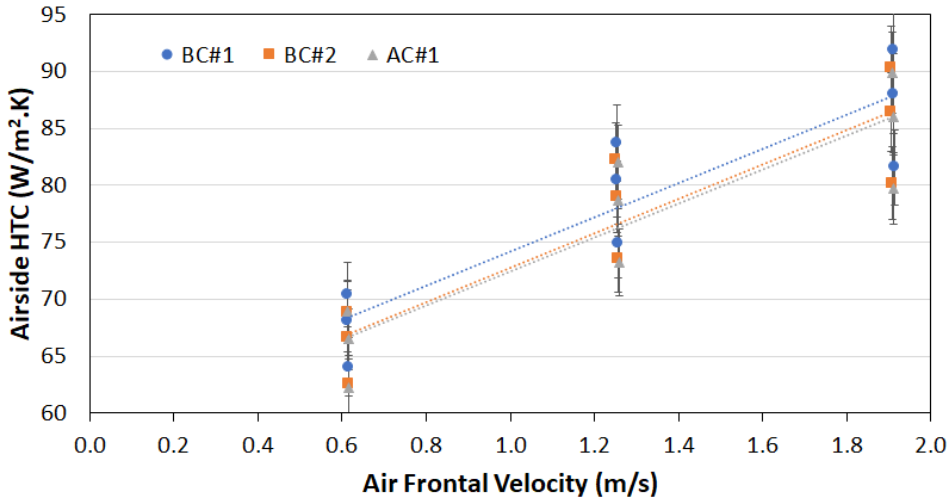

Figure 83: Airside Thermal Characteristics Before (BC#1 & BC#2) and After (AC#1) Cycling Tests

6.4. Conclusions for the SHX Prototype

Construction and testing of the SHX prototypes were successful. Both conventional serpentine circuiting and the split-merge joint approaches were tested. A modified split-merge connection was chosen for the fourth and final prototype SHX because it exhibited similar pressure drop levels as the conventional, as opposed to the increased pressure drop exhibited by non-modified split-merge circuiting. Testing for this HX resulted in a deviation from the expected capacity on the order of 5%, indicating that the model captured the physics well.

The success or lack thereof of brazing the joints of any given HX greatly affected its contact resistance. A more successful brazing greatly lowered contact resistance, and lead to much better performance.

Based on 82,000 cycles, no failure or permanent deformation was observed in these prototype HXs as a result of cyclic testing. Based on the testing results, construction process, and optimization, these HX prototypes were deemed ready for system-level integration and implementation.

7. System-Level Implementation

To truly evaluate the effectiveness of the SHX, it must be assessed in the context of the full system. With the design optimized and the feasibility of the SHX construction itself confirmed, the team was able to integrate additional prototype HXs into full system assemblies for testing.

The original intent of the project was to contrast a full-size condenser (outdoor unit) for a residential air conditioner or heat pump application. While the prototype SHXs were successful in confirming performance, what they also revealed were several challenges in manufacturing and handling that drove the team to consider alternative approaches for system level integration. In particular, a full-size condenser would have would have required prohibitively expensive and time-consuming new materials and construction. Further, residential condensers are typically bent to a "C" or "D" shape, enabling their enclosure in the condensing unit housing. Given the manufacturing process used for the SHX, and the challenge in fin material and fragility, bending a prototype SHX of this size was deemed too risky for the project.

As such, alternate coil sizes and configurations were explored in an attempt to mitigate the riskiest element and integrate the HX design into an existing system. Three alternate applications – a gas absorption heat pump water heater, a residential freezer, and a through-the-wall heat pump – were pursued, two in collaboration with possible commercialization partners. Evaluation of the initial system performance for the residential AC/HP case and each of the alternate system applications is described herein.

7.1. Modeling System Performance

For completeness of the numerical analysis, prior to HX testing and any integration with an actual system, selected optimum designs for a full-size condenser from the Pareto fronts presented in the optimization 5.1.5.3 Results Section were simulated in VapCyc®, a proprietary vapor compression cycle simulation tool, and compared against the baseline performance. The results showed performance improvement on the order of 1-2% for COP and cooling capacity over the baseline system (Figure 84).

The results also showed that the heat load in the condenser was, for most designs, very close to the baseline which was expected prior to the system simulation. The reduction in refrigerant pressure drop in the condenser had a positive impact on power consumption, and thus the overall COP. The three designs with considerably lower refrigerant pressure drop had an additional circuit, thus reducing the mass flux.

As noted above, while the initial system level analysis suggested a positive outcome for use of the SHX as a condenser for a residential heat pump or air conditioning

system, other manufacturing concerns and prototype limitations shifted the attention to incorporate the SHX concept in other applications.

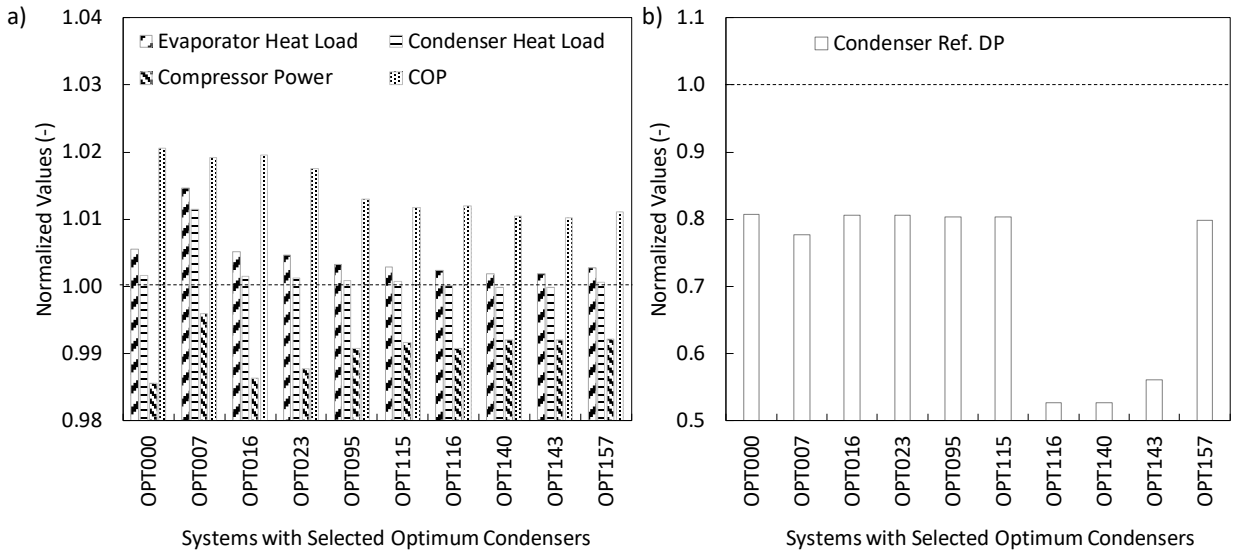

Figure 84: System Level Simulation Results.

7.2. Ammonia Gas Absorption Heat Pump Water Heater

The ammonia (NH3) gas absorption heat pump water heater developed by Stone Mountain Technologies Institute (SMTI) was chosen as one of several target systems for the novel SHX technology as opposed to the light commercial or residential R410A heat pump condenser. The baseline heat exchanger provided by SMTI was tested in a wind tunnel at the OTS laboratory for assessment of airside performance purposes and comparison with tested data obtained with the brazed SHX prototype tested in 2019. The results show that the baseline and SHX have equivalent airside effective convective heat transfer coefficient (Figure 85), with the SHX showing greater performance for lower velocities. This indicates that the SHX technology has potential for equivalent or even greater performance than the baseline. OTS provided SMTI performance curves for airside performance and they sized a HX appropriate for their needs. The heat exchanger consists of a rectangle of 13.5" x 17" and two rows (Figure 86) – unlike the original OTS SHX prototypes.

Two 2-row heat exchanger cores were provided by Brazeway at the end of March 2020 (Figure 87). Upon receipt, the fins seemed somewhat loose on the tubes, so a few material and collar adjustments were tested, as depicted in Figure 88. Different fin material temper was tested for the fins, resulting in slightly different collar

tightness over the tubes. The red arrows on the right image depict fins with loose collars and the green arrows depict fins with tight collars. The investigation concluded that the fins can be used as produced and the two heat exchangers made for SMTI were sent for brazing.

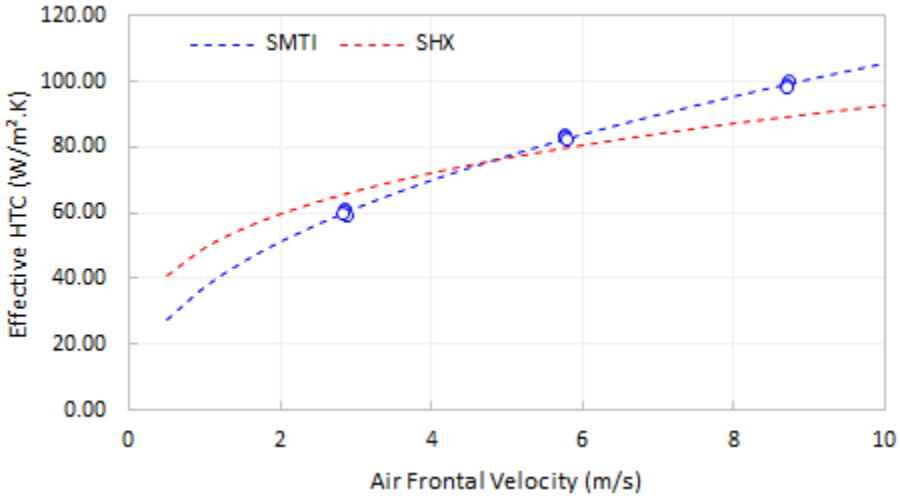

Figure 85: Airside Thermal Characteristics Comparison.

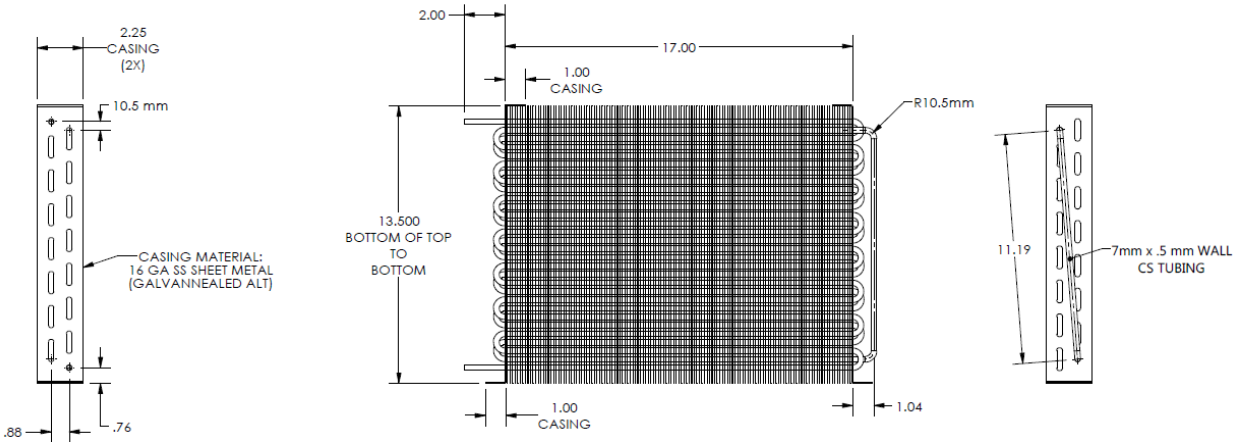

Figure 86: SMTI Prototype Drawing for SHX Fin.

A connecting tube was added to complete the circuitry (Figure 89) and the heat exchangers were sent to Arconic for brazing. Ultimately, the fins brazed very well to the tubes. On one HX, only nine collars could be slightly moved out of a few hundred tested. On the other coil, no loose collars were found.

The heat exchangers were leak tested with Nitrogen at 400PSI and no leaks were found. With the connecting tube, there are only two joints that could leak – meeting the main project objective. If hairpins were used, there would be 28 additional joints.

Following final assembly and leak testing at HTT, SMTI received one sample for testing within their gas absorption NH_3 heat pump water heater, and performed tests to benchmark current heat exchanger performance, followed by testing the new prototype under the same test conditions. OTS received the second sample and performed a series of wind tunnel heat exchanger-only tests to confirm performance.

For the heat exchanger-only, 15 tests were first performed in dry conditions using hot water as the working fluid in the OTS wind tunnel (Table 22). These experiments measured the air-side pressure drop of the heat exchanger as well as the capacity, which could then be used to determine heat transfer coefficients. Test conditions included lower air velocities relevant to most HVAC&R applications as well as much higher air velocities consistent with past testing performed under this project. Ideally, higher water flow rates would be utilized to minimize water-side temperature differences, however the high water-side pressure drop of the single-circuit heat exchanger was prohibitive of higher water flow rates.

These tests were important to confirm performance relative to model predictions that would identify any potential issues with the fabrication process or any shortcomings that might occur during system-level testing. Figure 90 shows the experimentally measured air-side pressure drops and capacities compared against model predictions. Predictions were based on a CoilDesigner® model of the heat exchanger with pressure drop and heat transfer correlations developed by power fitting CFD simulation data of the SHX fin. The results show excellent agreement with predicted performance and lower air-side pressure drop than predicted; this is likely due to the fact the SMTI prototype had 15 fins per inch and two banks, while the CFD models were originally developed for higher fin densities and only one bank of tubes. These tests were deemed successful and allowed the team to move forward with system-level testing with confidence.

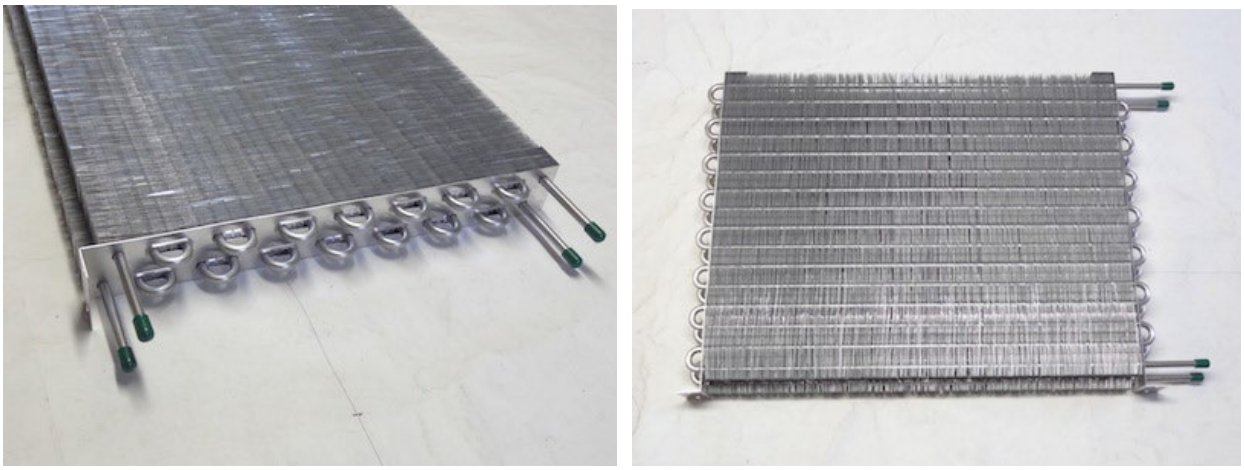

Figure 87: Heat Exchanger Core Prototypes for SMTI

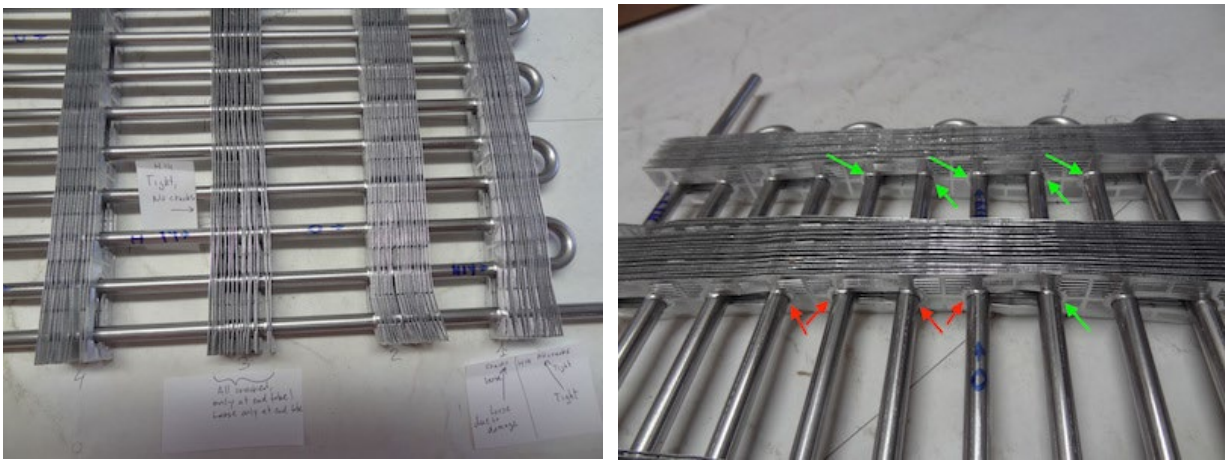

Figure 88: Testing of Fin Material and Proposed Collar Adjustments

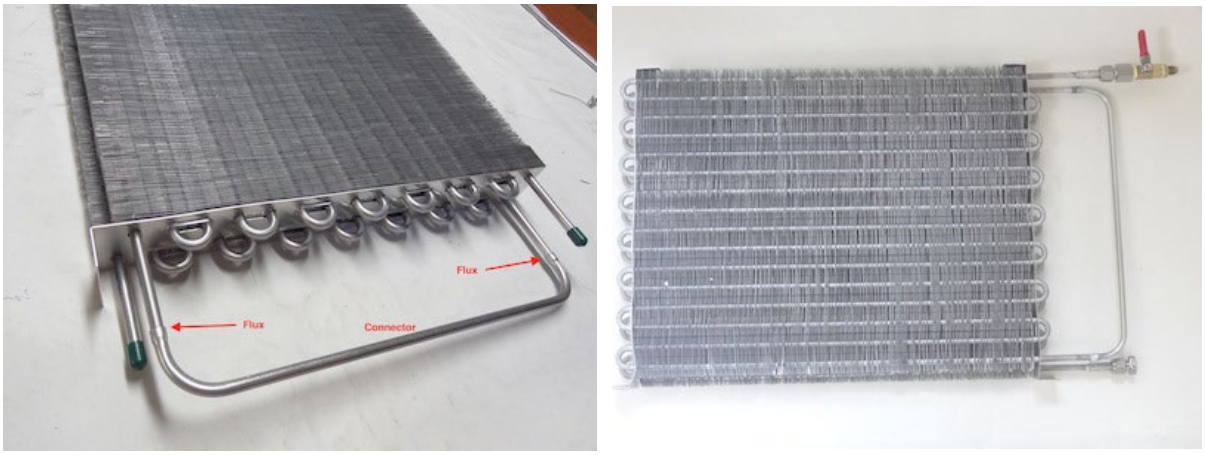

Figure 89: Connecting Tube and Final Prototype Assembly

With the prototype samples still in hand and installed in the OTS wind tunnel, the team had an opportunity to further study the performance of the SHX. To date all modeling and analysis work had focused on dry condition performance of the SHX. This was due to the complexity of condensation physics and the lower maturity of multiphase modeling in CFD simulation tools. While appropriate for condensers and some cooling conditions, dry surface conditions are not representative of evaporator performance in dehumidification conditions. Understanding the SHX's performance in dehumidification conditions is an essential step to enable its implementation as an indoor evaporator in an air conditioning or refrigeration application or as the outdoor unit in a heat pump. In order to begin to fill this knowledge gap, an additional 18 tests were performed on the sample SHX. These tests were performed with cold water (below the dew point of the warm, humid air) as the working fluid under a range of humidity and flow conditions. Table 23 shows the matrix of test conditions, which were focused on air velocities more relevant to HVAC dehumidification conditions and the SMTI system. Figure 91 shows the energy balance error of the tests along with the uncertainty. While acceptable energy balances were achieved between air- and water-side capacities, there is a high uncertainty in the air-side capacity due to the latent capacity's high sensitivity to relative humidity uncertainty.

Table 22: Hot Water Dry Test Conditions for SMTI Prototype

	Water Temperature	Water Flow Rate	Air Temperature	Velocity
	°C	g/s	°C	m/s
Tolerance	**0.5**	**1**	**0.5**	**10%**
Test #1	60	80	16	1
Test #2	60	90	16	1
Test #3	60	100	16	1
Test #4	60	80	16	2
Test #5	60	90	16	2
Test #6	60	100	16	2
Test #7	60	80	16	3
Test #8	60	90	16	3
Test #9	60	100	16	3
Test #10	60	80	16	6
Test #11	60	90	16	6
Test #12	60	100	16	6
Test #13	60	80	16	9
Test #14	60	90	16	9
Test #15	60	100	16	9

Test results are shown in Figure 92 and show general agreement with model predictions for capacity and air-side pressure drop. Sensible heat ratios range from 54-88% and average 69%, indicating that significant dehumidification is occurring relative to the total heat load. Interestingly, the observed air-side pressure drop is not significantly higher than the predictions or measurements in the dry condition. Typically cooling coils in wet conditions experience significantly higher air pressure drops than in dry conditions. This is a promising result and requires further investigation. However, it is essential to note the aforementioned limitation in water mass flow rate leads to a large water temperature change across the coil meaning that many sections of the heat exchanger may be above the dew point and doing little-to-no dehumidification and therefore would not be subject to increased pressure drop due to condensate retention. If the total load of the heat exchanger were greater, it is possible the retention of condensate on the fins could lead to increased pressure drop.

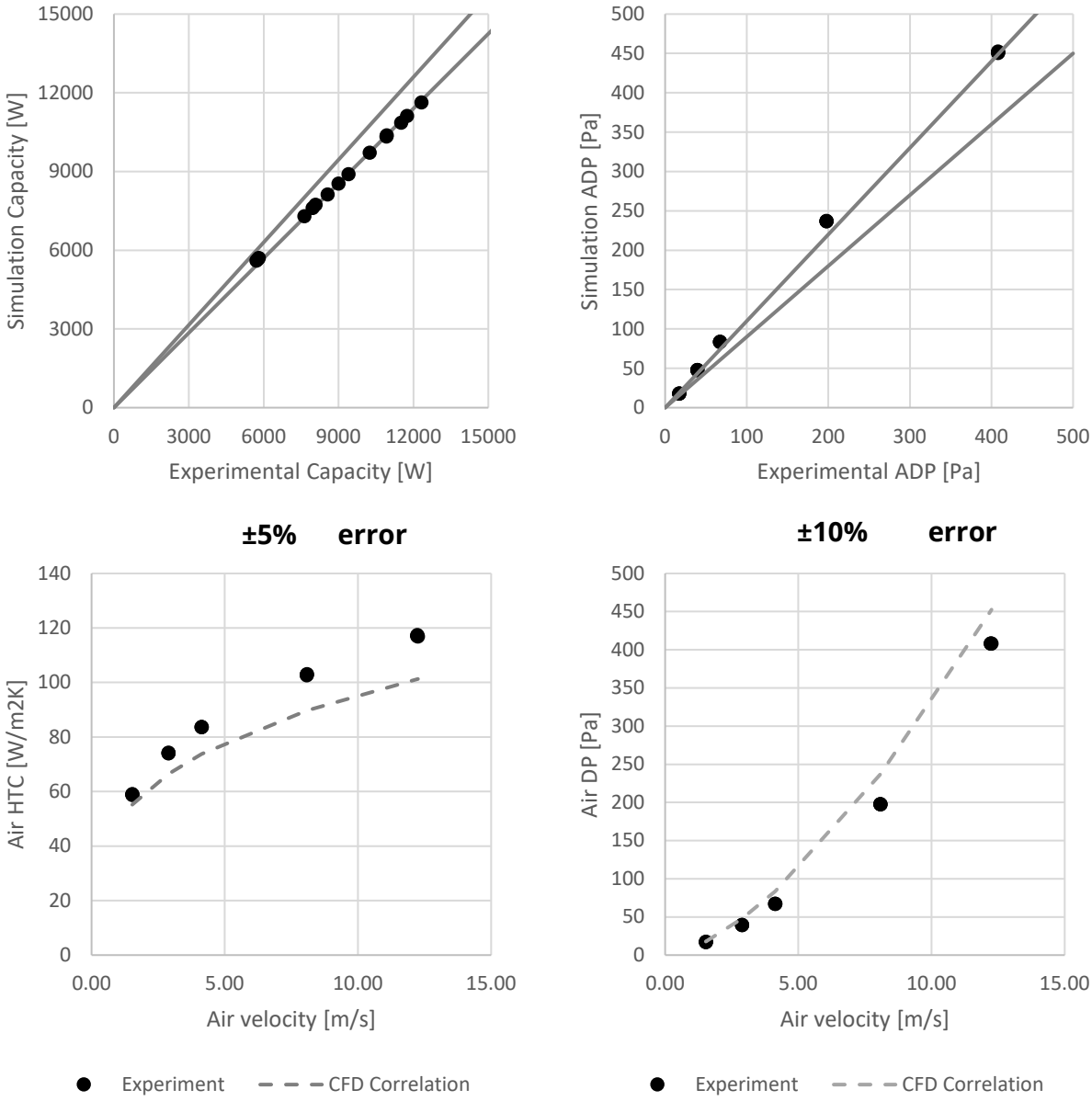

Figure 90: Experimental Measurements – Dry tests of SMTI 15 FPI prototype

Table 23: Wet condition test matrix

Water Inlet Temperature	Water Flow Rate	Air Inlet Temperature	Air Inlet RH	Air Velocity
°C	g/s	°C	%	m/s
9.6	80.0	30.1	63.9	3.1
9.6	90.0	30.1	64.0	3.1
9.9	100.0	29.7	63.8	4.6
9.9	100.0	30.6	63.3	1.7
9.5	90.0	30.5	63.3	1.7
10.0	100.0	33.0	55.6	4.7
9.9	90.0	33.0	55.7	4.7
9.5	80.0	33.0	55.7	4.7
9.4	80.0	33.0	55.7	3.1
9.9	90.0	33.0	55.6	3.1
9.9	100.0	33.0	55.7	3.1
9.9	90.0	33.0	55.0	1.7
9.7	80.0	33.0	55.0	1.7
9.6	80.0	30.0	63.4	1.7
10.0	100.0	30.0	63.9	3.1
9.9	80.0	30.0	64.1	4.6
9.9	90.0	30.0	64.0	4.6
10.1	80.0	33.0	55.1	1.7

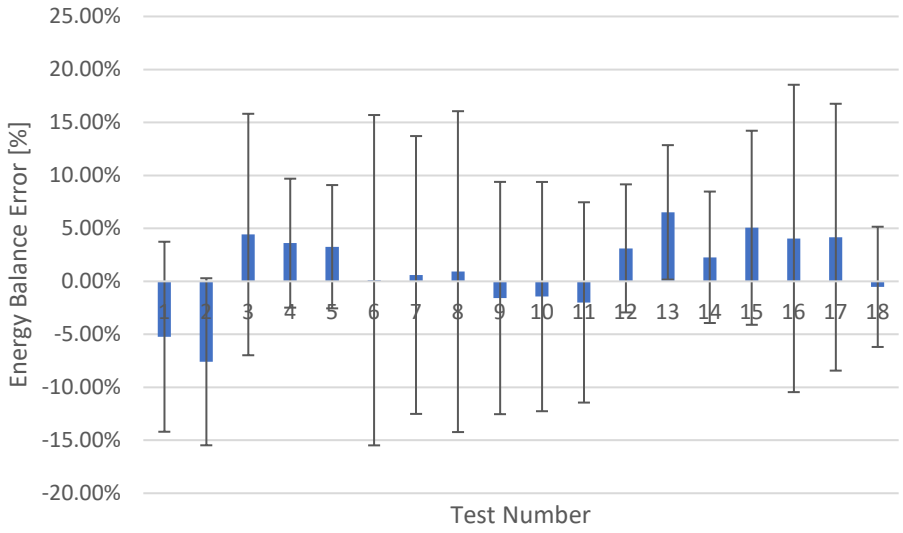

Figure 91: Wet Condition Energy Balances

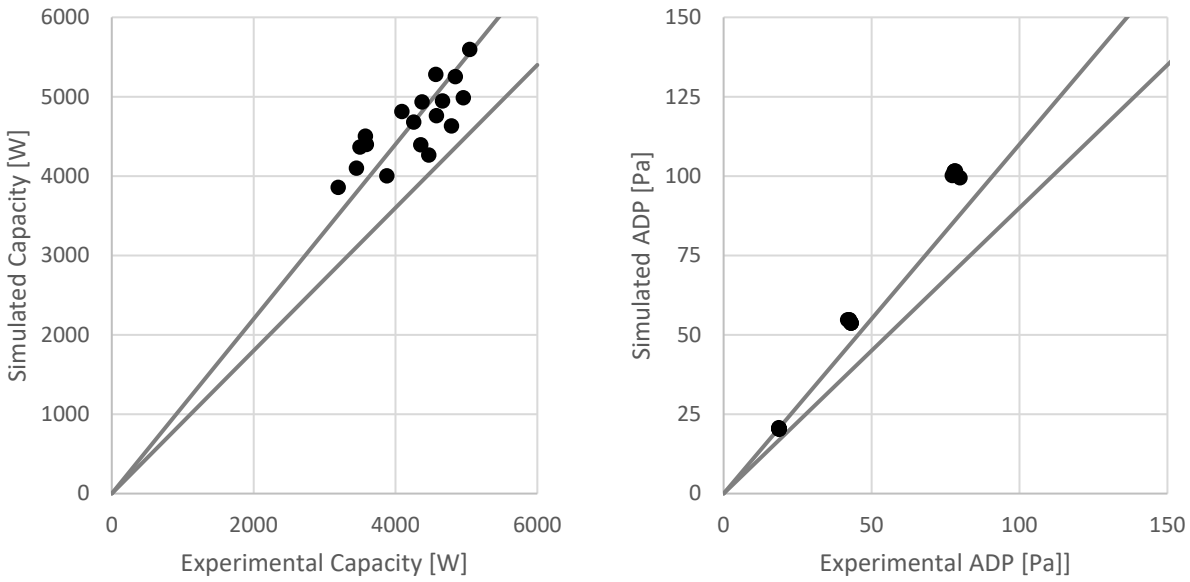

Figure 92: Wet Condition Test Results (10% Error Bars)

In parallel with heat exchanger-only testing, SMTI conducted system level testing using the SHX as the evaporator for the gas absorption heat pump water heater. Pictures of the serpentine coil installed in the SMTI unit are depicted in Figure 93. SMTI's heat pump utilizes ammonia-water as the solution where ammonia is the refrigerant and water the absorbent. The evaporator will see 99+% ammonia and <1% water; it is difficult to fully remove the water vapor from the solution prior to this point in the system. Given the use of ammonia and water, it is very important that the aluminum used is compatible with ammonium hydroxide. The coil was installed in the heat pump for approximately 8 months with no signs of a material failure or degradation.

There are numerous advantages to using aluminum instead of carbon steel in the evaporator for the SMTI system. The primary reason is aluminum's superior heat transfer coefficient. One of the essential elements of a thermally driven heat pump's performance is its ability to transfer heat. The example at hand is taking heat from the ambient to evaporate the refrigerant. This process has a strong impact on the overall efficiency of the cycle. As such, the thermal conductivity of the materials provides a direct indication of the potential results. Aluminum has an average thermal conductivity of 237 W/m-K (137 Btu/ft-hr-F) while carbon steel has an average thermal conductivity of only 45 W/m-K (25 Btu/ft-hr-F). Such a difference

demonstrates the enormity of the benefit in utilizing aluminum over carbon steel for this application.

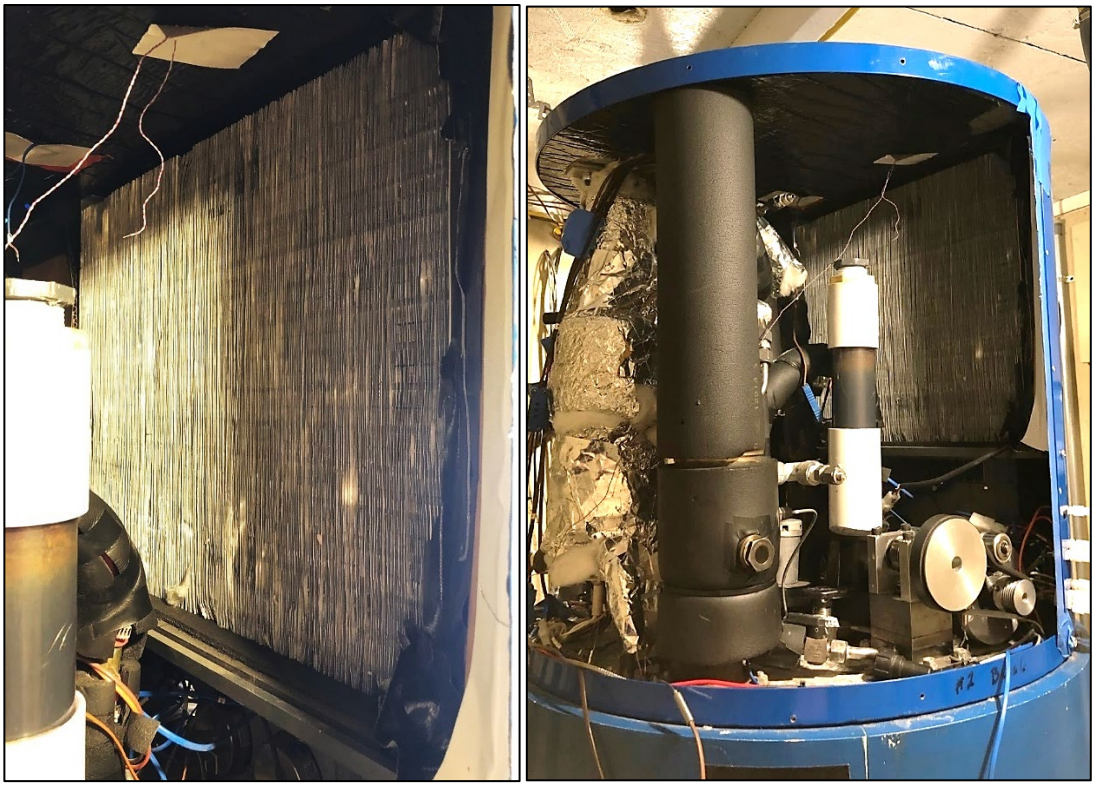

Figure 93: Advanced Serpentine Heat Exchanger (left) as Installed in the SMTI Heat Pump System (right)

To evaluate the potential of the advanced SHX, a baseline carbon steel coil was first tested on one of SMTI's water heaters inside an environmental chamber. The room and unit were outfitted with extra sensors to increase the reliability of the measurements taken. A picture of the baseline carbon steel coil within the SMTI heat pump water heater is depicted in Figure 94. Once a range of tests had been completed on the carbon steel coil, it was cut out of the heat pump and the advanced SHX coil was plumbed in place using compression fittings. The coil then went through an identical set of tests to compare performance.

Results are depicted in Figure 95 and Figure 96. As seen in Figure 95, the advanced SHX provided an increase in performance based on system COP where the heat load from the hydronically-coupled heat exchangers is divided by the gas input. Using the same heat pump to test both coils helped to narrow this performance increase to the

change in evaporators. Albeit one could also see this improvement by looking at the increase in evaporator load for the given tests, as shown in Figure 96.

Figure 94: Baseline Carbone Steel Heat Exchanger in the SMTI Heat Pump Water Heater

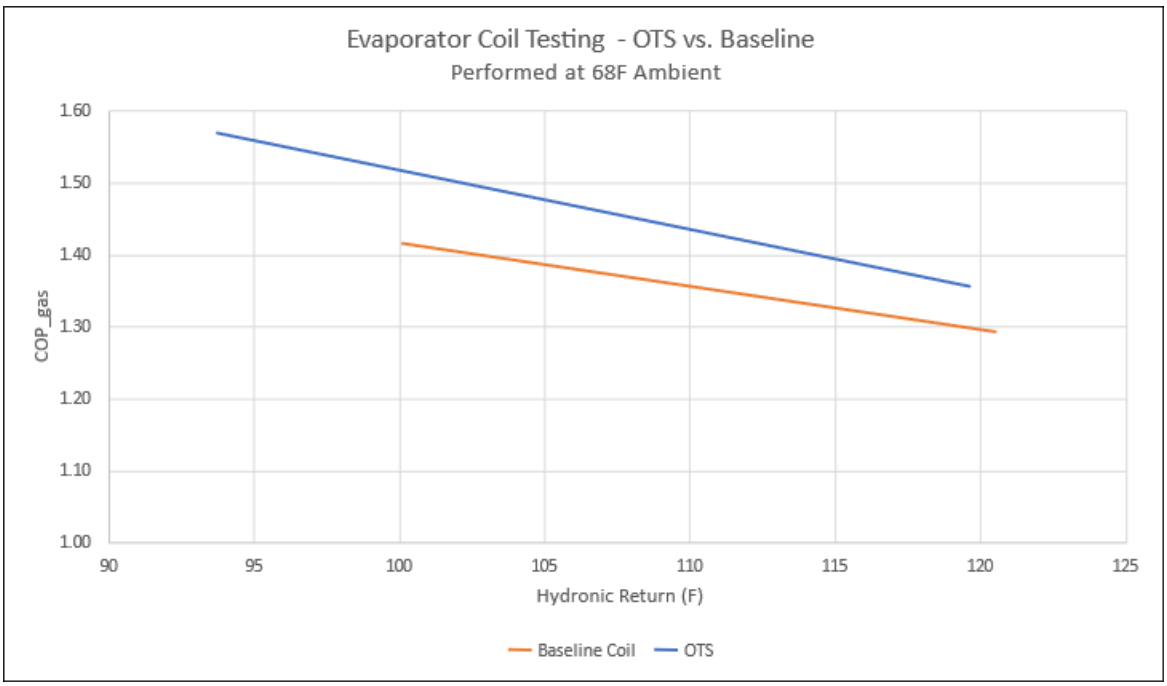

Figure 95: Heat Exchanger Performance Comparison Based on System COP

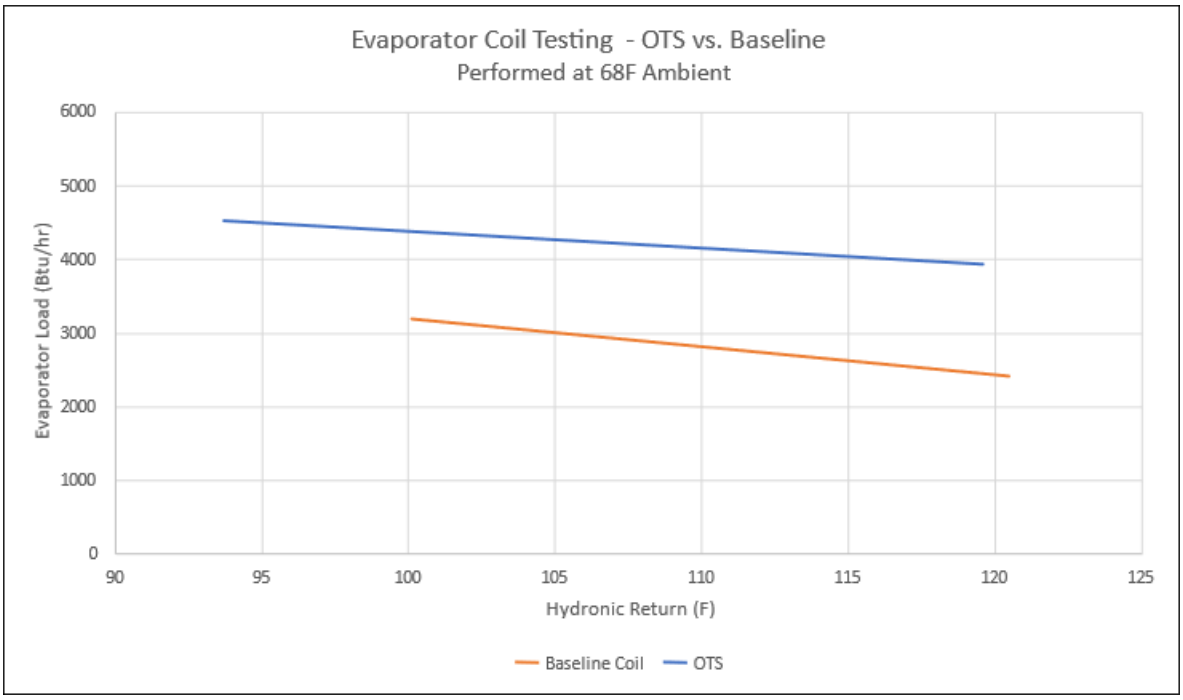

Figure 96: Heat Exchanger Performance Comparison Based on Evaporator Load

Another measure of improvement was the power consumption from the evaporator fan motor. At the same fan speed, the advanced SHX coil provided about 8 cfm higher airflow and had a reduction of about 2 Watts. SMTI could not accurately measure the air-side pressure drop but this reduction in power consumption (i.e. load on the motor) implies that the advanced SHX coil provides a lower pressure drop as compared to the baseline.

Another benefit of using the advanced aluminum SHX is its corrosion resistance. Steel requires additional coatings, paints, or protective layers to prevent rust or corrosion from typical ambient conditions, which adds more cost and potential failures. Aluminum, however, naturally forms a "coating" of aluminum oxide, which acts as a protective layer from rust and corrosion. Since the evaporator will naturally collect condensation during operation of the heat pump it is vital that the tubes used are capable of withstanding years of exposure. As seen in Figure 94, the carbon steel baseline coil with painted return bends has already started showing signs of surface rust after only a few years of operation.

Furthermore, aluminum is over half as dense as carbon steel (7.8 g/cm^3 versus 2.7 g/cm^3). Such a decrease in weight not only sees benefits from decreasing the overall shipping and transportation cost, but also makes it more manageable for contractors during installation.

In summary, the advanced SHX is an attractive option for replacement to SMTI's previous carbon steel evaporator coil. The improved heat transfer of aluminum versus steel leading to higher system performance, reduction in weight, added corrosion resistance, and much lower leak potential all make it a likely candidate for a production option. While aluminum has currently a 50% higher price than steel on a per kilogram basis, the added manufacturing step of brazing steel U-bends brings the ASHX and steel coil closer in cost. Further, the ASHX will be closest in cost to steel of either aluminum microchannel or copper RTPF coils, and therefore presents a viable option for commercialization of the advanced SHX alone as well as the SMTI heat pump water heater system.

7.3. Residential Freezer

In parallel with the efforts to demonstrate the SHX technology with the SMTI absorption heat pump, OTS and HTT contacted Sub-Zero, Inc. (Sub-Zero), a domestic

refrigeration and appliance company. Serpentine heat exchangers are commonly used in refrigeration for their ease of construction and low cost. Lower fin density is required on heat exchangers used in such applications to reduce the negative effects of fouling. Producing a serpentine heat exchanger that has the potential to provide better thermal performance for little or no incremental cost has significant potential in this application. As such, OTS explored the prospect of developing and testing prototype heat exchangers for a domestic freezer by producing two possible designs for SubZero.

Given the potential for fouling in a refrigerator/freezer condenser, the proposed SHX designs for SubZero had only 6 and 8 FPI. OTS first conducted additional CFD analyses for the serpentine fin design to confirm that the correlations and assumptions used for the SubZero coil would still be appropriate given the difference in required fin density. Analysis revealed that the enhanced serpentine fin has a higher convective heat transfer coefficient and a lower fin efficiency than the SubZero baseline design, but overall, the *effective* heat transfer coefficient is comparable. As such, CoilDesigner® was used to design the two possible configurations, which were approved by SubZero in August 2020.

The prototype heat exchangers for the SubZero refrigerator were completed by Brazeway and delivered to HTT in late December 2020. Brazeway constructed the prototype cores, while HTT brazed the heat exchangers in an inert atmosphere furnace as opposed to outsourcing to Arconic. Modifications to the furnace and a retort box enabled brazing of aluminum heat exchangers in-house at HTT.

Adapter sleeves from the 7mm tubes to 3/8" OD were attached to the appropriate tubes in order to attach port fittings, and a return-bend was attached to the other two tubes to complete the circuit, as shown in Figure 97. In production, the return bend will be part of the serpentine circuit. The heat exchanger was then brazed in the furnace. A post-braze joint test showed good fin to tube brazing (Figure 98).

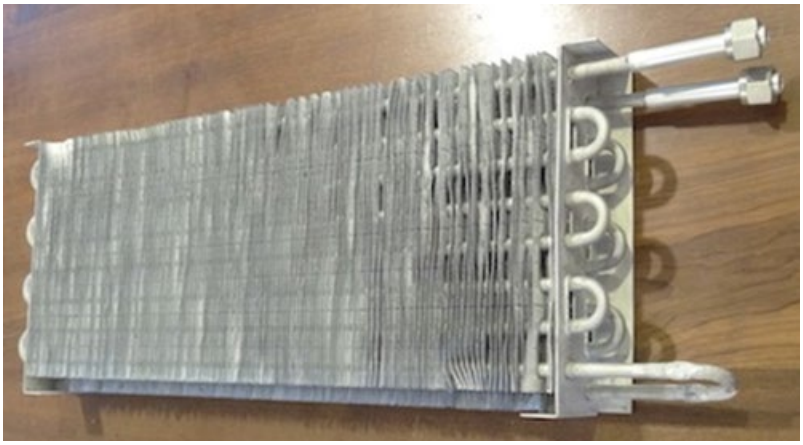

Figure 97: Brazed SubZero Prototype

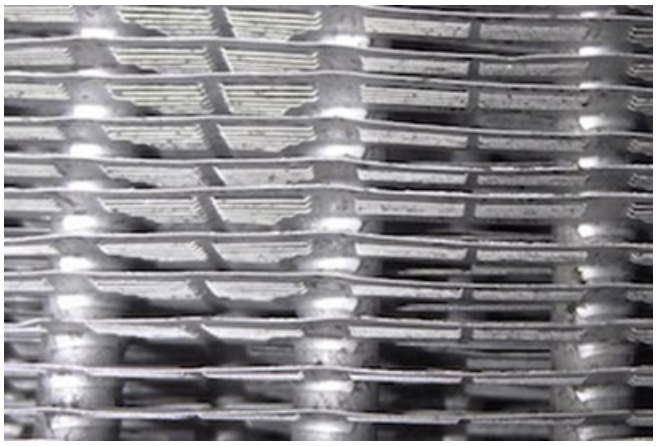

Figure 98: SubZero Prototype, Brazed Fins to Tubes

The heat exchanger was leak free under a 300 PSI Nitrogen pressure test, shown in Figure 99. The heat exchanger was then shipped to Sub-Zero for testing in their appliance.

Once received, Sub-Zero worked to integrate the prototype coil as a condenser within a built-in 36" all-freezer appliance using R-600a (isobutane) as the refrigerant. Sub-Zero conducted three levels of baseline testing to compare against the advanced SHX. These included a conventional a wire on tube condenser (Figure 100), a tube-fin (Figure 101) condenser, and a microchannel condenser (not pictured). After completing baseline testing, Sub-Zero installed the prototype advanced SHX, as shown in Figure 102. Testing was conducted in a controlled environment in accordance with the Association of Home Appliance Manufacturers (AHAM) test procedure.

Figure 99: SubZero Prototype Leak Pressure Test

Figure 100: Wire on Tube Baseline Heat Exchanger in Sub-Zero System Assembly

Figure 101: Tube-Fin Baseline Heat Exchanger in Sub-Zero System Assembly

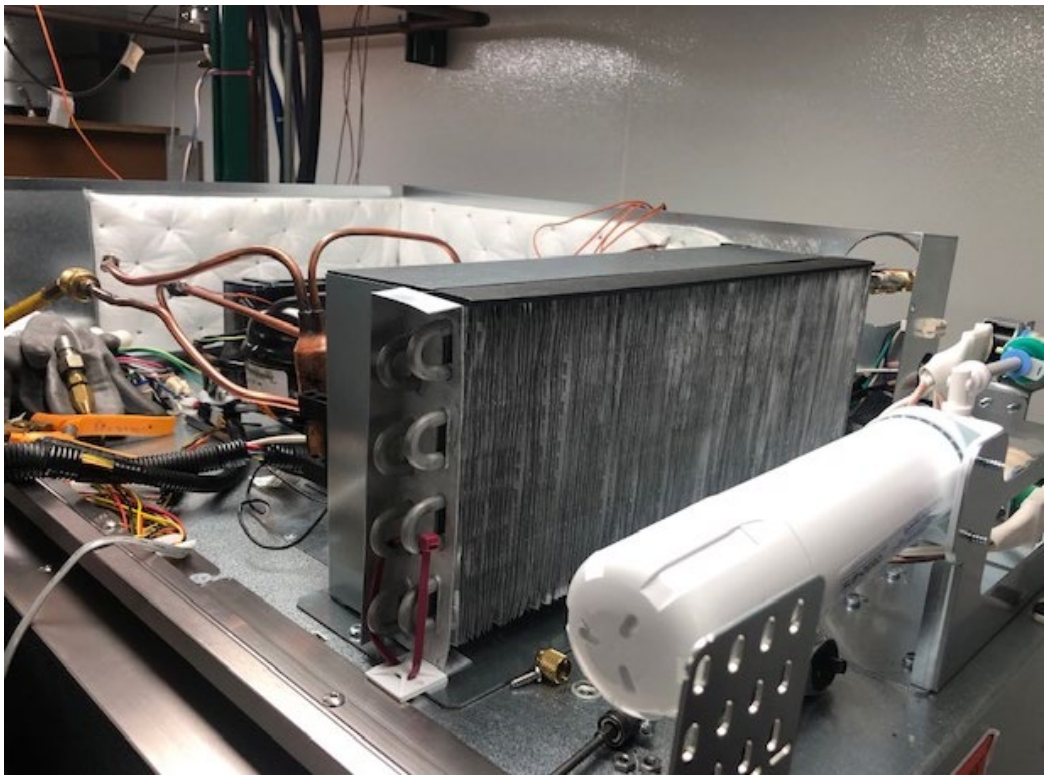

Figure 102: Prototype Advanced Serpentine Heat Exchanger Installed in Sub-Zero Assembly

Results are summarized in Table 24. Early tests with the advanced SHX resulted in higher compressor run time suggesting that the cooling capacity was low; this is typically a symptom of low refrigerant charge. Subsequent tests with additional system charge resulted in improved efficiency and decreased run time.

Ultimately, testing revealed that the prototype advanced SHX could achieve higher efficiency (2.6% less energy consumption) than the wire-on-tube condenser baseline. Energy efficiency was less than that measured for the tube-fin and microchannel baselines, but still very competitive, especially considering a prototype compared against mass-produced coils.

Overall, the results are extremely promising as they indicate the prototype can achieve comparable efficiency to the existing product at a likely much lower cost. It should also be noted that the prototype heat exchanger has some known defects (some incomplete brazing between fins and tubes) that when corrected in mass production would further improve performance.

While not specifically tested, it is also expected that the ASHX design would not have any significant impact or increase in dust accumulation or other coil fouling. Similar fin spacing is maintained to wire-on-tube and fin-tube coils currently in use.

Table 24: Sub-Zero System Testing Results

Parameter	Baseline			Advanced Serpentine HX	
	Wire on Tube	Fin on Tube	Microchannel	Initial Charge	Best Charge
Average Power (W)	58.25	56.05	54.40	57.81	56.88
Cabinet Temperature Average (°F)	0.05	0.00	-0.54	-0.08	-0.56
Average Ambient Temperature (°F)	89.95	89.59	89.40	89.68	89.58
R600a Charge (g)	85	85	83	85	91
Calculated Energy Consumption (kWh/day)	1.226	1.174	1.141	1.215	1.194

7.4. Through-the-Wall Heat Pump

One of the prototype coils originally designed and constructed for SMTI remained at the OTS laboratory, available for additional testing. Given it's relatively small size, OTS opted to test the prototype in a through-the-wall heat pump. A 7,400 Btu/hr (cooling capacity) model from Amana, as shown in Figure 103, was selected for testing.

Figure 103: Amana PBH073G35CC Through-the-Wall Unit

The Amana's condenser has similar face area to the SHX coil such that replacement was not a significant challenge. There were several notable differences between the prototype coil and the baseline outdoor coil for the Amana unit, however, which are summarized in Table 25. It is important to note that the prototype coil tested was *not* originally designed or sized for the Amana system. The prototype coil had less than half of the airside surface area of the baseline tube-fin heat exchanger and ~75% less material mass; as such, its performance should reasonably be expected to be much lower.

Taking on this demonstration independently of the system manufacturer required OTS to make several assumptions about the system design and performance to determine feasibility. A CoilDesigner® model of the condenser was created to simulate cooling mode performance at the 95°F ambient condition. A comparison of the two coils and their respective circuitries is shown in Figure 104. Using the system's rated EER to estimate compressor power input and condenser heat rejection, and assuming an air flow rate from similar products, the CoilDesigner®

model demonstrated the SHX's ability to reject the required heat at 122°F condensing temperature, which is typical of these systems.

The Amana unit was installed in a temperature and humidity controlled environmental chamber which was split into two compartments. One side represented the indoor, conditioned side, as shown in Figure 105; the other represented the outdoor side and was controlled to maintain a consistent ambient temperature. Testing was initially done with the unit as-is, using the baseline tube-fin condenser, as shown in Figure 106. Once baseline testing was completed, the condenser coil was replaced with the advanced SHX, as shown in Figure 107.

Table 25: Outdoor coil geometry comparison

		Tube-Fin Coil		Serpentine Coil	
Dimension	**Units**	**EN**	**SI**	**EN**	**SI**
Tube Material	-	Copper		Aluminum	
Tube outer diameter (D_o)	in/mm	0.315	8.00	0.278	7.05
Tube inner diameter (D_i)	in/mm	0.252	6.40	0.199	5.05
Tube thickness (δ_t)	in/mm	0.031	0.80	0.039	1.00
Tube transverse pitch (P_t)	in/mm	0.748	19.00	0.866	22.00
Tube longitudinal pitch (P_l)	in/mm	0.827	21.00	0.827	21.00
Number of rows (N_r)	-	17		16	
Number of tube banks (N_t)	-	3		2	
Fin Material	-	Aluminum		Aluminum	
Fin Type	-	Louver		Louver	
Fin Density (F_d)	in^{-1}/m^{-1}	16	630	17	669
Fin thickness (δ_f)	in/mm	0.004	0.110	0.004	0.110
Fin pitch (F_p)	in/mm	0.058	1.478	0.054	1.384
Coil length (L)	in/mm	17.87	454.0	12.59	320.0
Coil depth (D)	in/mm	2.244	57.0	1.732	44.0
Coil height (H)	in/mm	14.055	357.0	13.228	336.0
Primary Heat Transfer Area (A_p)	ft^2/m^2	5.831	0.542	2.283	0.212
Secondary Heat Transfer Area (A_s)	ft^2/m^2	109.1	10.138	54.78	5.089
Total Air Side Heat Transfer Area (A_a)	ft^2/m^2	114.9	10.679	57.06	5.301
Refrigerant Side Heat Transfer Area (A_r)	ft^2/m^2	5.011	0.466	1.749	0.162
Coil Face Area (A_f)	ft^2/m^2	1.745	0.162	1.157	0.108
Tube Material Mass (m_t)	lb/kg	8.221	3.729	1.159	0.526
Fin Material Mass (m_f)	lb/kg	3.810	1.728	1.829	0.83
Total Material Mass (m_{tot})	lb/kg	12.031	5.457	2.988	1.355

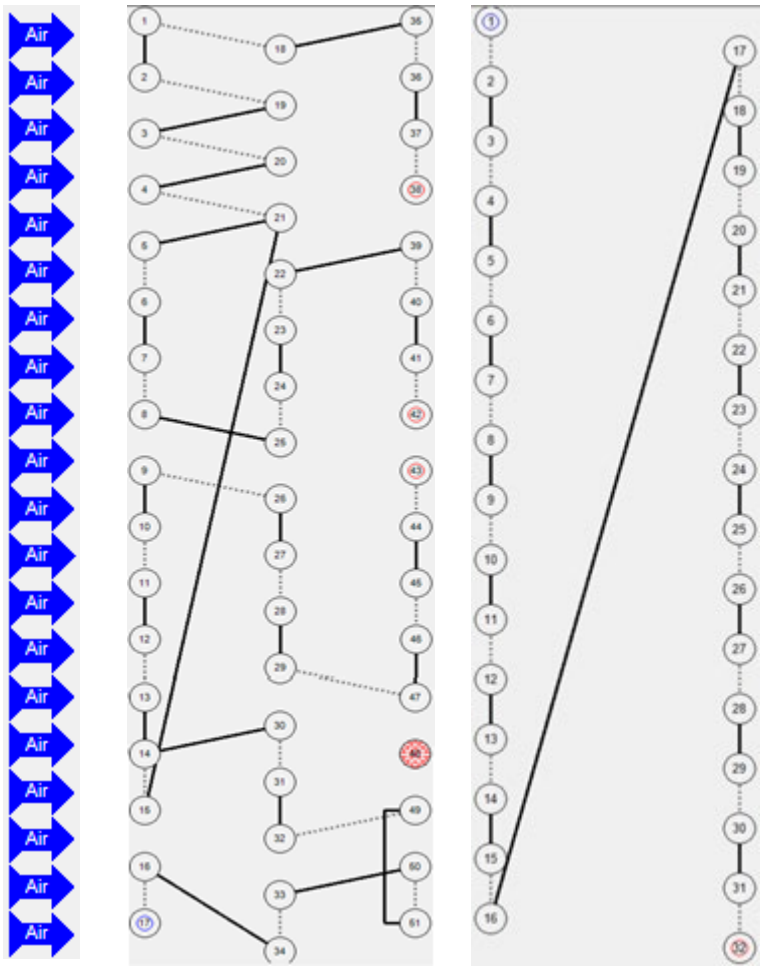

Figure 104: Outdoor coil circuitry: tube-fin coil (left); serpentine coil (right)

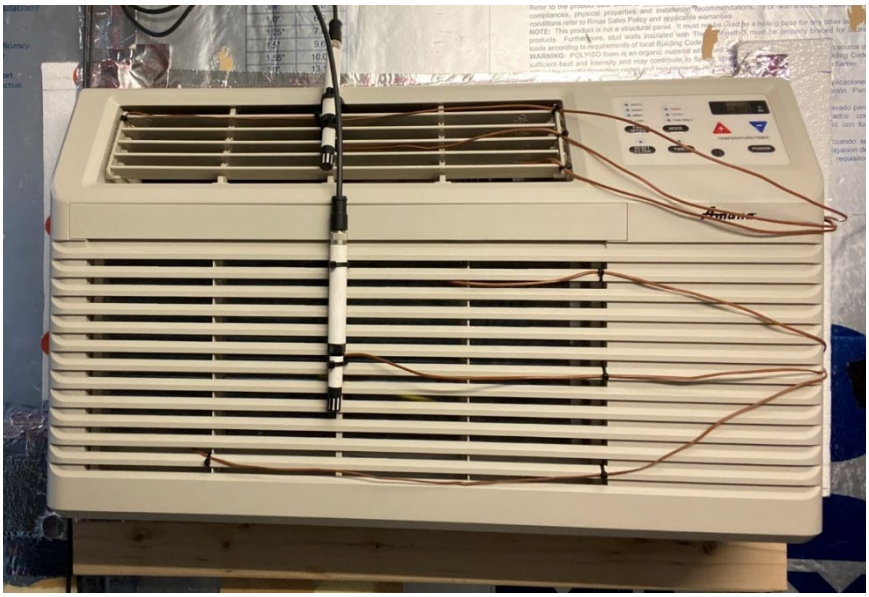

Figure 105: Amana PBH073G35CC Through-the-Wall Unit (indoor coil)

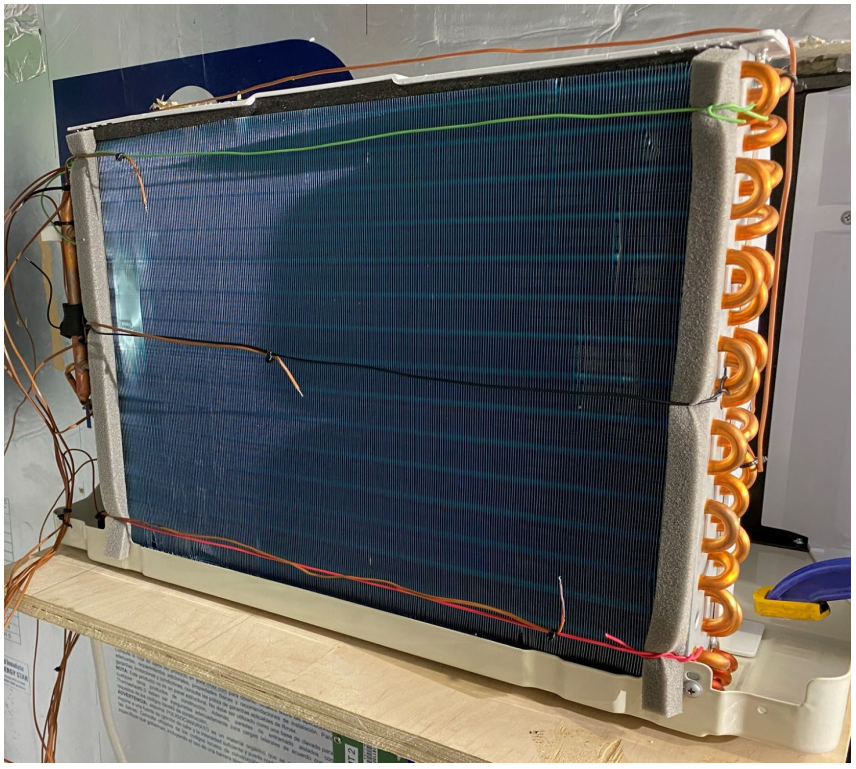

Figure 106: Amana PBH073G35CC Through-the-Wall Unit with Baseline Outdoor Tube-Fin Coil

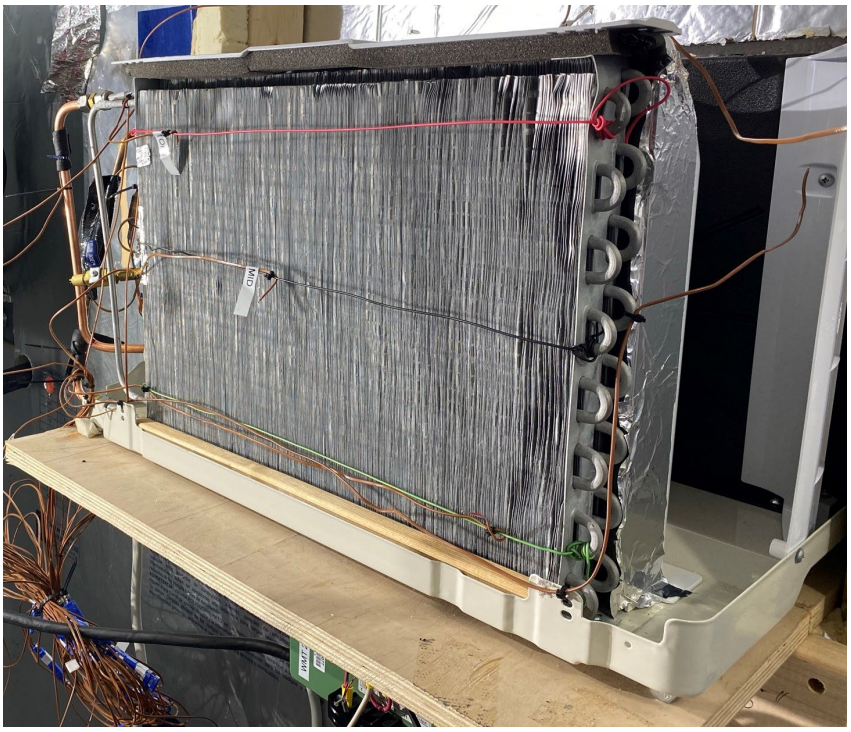

Figure 107: Amana PBH073G35CC Through-the-Wall Unit with Outdoor Serpentine Coil

Performance tests were conducted in both cooling and heating modes according to ANSI/ASHRAE Standard 16-2016 using the test conditions specified in ANSI/AHRI Standard 210/240 (Table 26). For each the baseline and advanced SHX cases, four tests were initially conducted to identify the appropriate refrigerant charge that would optimize performance. Performance tests were conducted using a refrigerant charge for which the unit had the highest COP. Ultimately, this meant a more than 60% reduction in refrigerant change for the advanced SHX as compared to the baseline condenser.

Table 26: ANSI/AHRI Standard 210/240 Test Conditions

	Air Entering Indoor Unit			Air Entering Outdoor Unit		
Mode	**Dry-Bulb [F]**	**Wet-Bulb [F]**	**RH [%]**	**Dry-Bulb [F]**	**Wet-Bulb [F]**	**RH [%]**
Cooling	80	67	51	95	75	40
Heating	70	60	56	47	43	73

Table 27 compares the unit performance in cooling and heating modes with the baseline tube-fin and serpentine condensers. It is clear that the unit capacity and the COP with the serpentine condenser is lower than those with the baseline tube-fin

heat exchanger. This is largely an effect of the smaller surface area of the SHX as noted in the original comparison. Although it was expected that the condenser air flow rate was higher because of the fewer tubes banks, lower fin density, and fin type of the serpentine coil, the specifics of the fan behavior were not known. The air condenser air flow rate and pressure drop across the outdoor coil were not measured during the test. Regardless, these test results demonstrate the heat exchanger's ability to operate in this application despite its considerably lower size, mass and cost, as well as indicate its potential for further optimization for such systems.

Table 27: Heat pump performance comparison with tube-fin and serpentine condensers

	Cooling			Heating		
	Baseline Tube-Fin Condenser	Advanced Serpentine Condenser	Diff.	Baseline Tube-Fin Condenser	Advanced Serpentine Condenser	Diff.
Refrigerant Charge [g]	800	490	-63.3%	800	490	-63.3%
Sensible Capacity [Btu/h]	4,039	3,897	-3.7%	7,529	6,664	-13.0%
Latent Capacity [Btu/h]	3,463	2,884	-20.1%	0	0	0
Total Unit Capacity [Btu/h]	7,503	6,780	-10.7%	7,529	6,664	-13.0%
Unit Power Usage [W]	629	685	8.2%	578	551	-4.8%
COP [-]	3.50	2.90	-20.6%	3.82	3.54	-7.8%
EER [Btu/W-h]	11.9	9.9	-20.6%	13.0	12.1	-7.8%

8. Conclusions and Recommendations

An alternative serpentine heat exchanger concept was successfully designed, analyzed, prototyped and tested demonstrating the ability to replace conventional HXs with an alternate technology that reduces refrigerant leakage by way of joint reduction. Four prototype SHXs were independently tested, verifying initial modeling work and confirming the proposed manufacturing methods. Further prototypes were then successfully demonstrated in three system applications: a novel gas absorption heat pump water heater, a residential freezer, and a through-the-wall heat pump.

Advantages of the SHX were demonstrated throughout the project including:

- **Elimination of conventional U-bends and the need to braze them, thus eliminating additional manufacturing steps;**
- **Elimination of the tube expansion process, saving a manufacturing step, but also allowing for inner grooved tubes to remain undamaged, ultimately improving tube efficiency and overall heat transfer performance;**

- **Simple construction, with a one-step-brazing process to a complete finished product;**
- **Comparable or improved heat transfer performance over the baseline condition;**
- **Reduced weight;**
- **Added corrosion resistance (as applicable);**
- **Reduced internal volume, allowing for lower refrigerant charge; and,**
- **Reduced cost as compared to copper tube-fin (76% cost reduction), aluminum tube-fin (19% cost reduction) and microchannel (16% cost reduction) HXs.**

Work is underway to commercialize the SHX for each of the demonstrated system applications as well as additional markets. While the SHX design incorporates fin enhancements and the tube-to-fin braze joint, it allows for adequate flexibility to be adapted from one application to another, allowing potential for success and larger spread adoption than for a single end-use. As was seen with testing the SHX in the through-the-wall heat pump, however, proper design is critical to meeting or exceeding baseline performance both in terms of capacity and efficiency.

From a manufacturing standpoint, it is anticipated that full production SHXs would have an improved process over the prototypes, resulting in additional performance gain. The prototype HXs had known defects (incomplete brazing between fins and tubes) that when corrected in mass production will further improve heat transfer performance.

Overall, the advanced SHX is an extremely promising technology. Development work has demonstrated that the concept can achieve comparable efficiency to baseline HXs for multiple applications and for likely a much lower cost while further reducing the number of brazed joints and thus the potential for refrigerant leakage.

9. References

Agba, E. I., et al., "An Investigation of the Effects of Autobrazer Parameter Variations on the Quality of Return Bend Joints" (1997). *Proceedings of the Institution of Mechanical Engineers*. vol. 211. doi: 10.1243/0954405971516400.

AHRI, December 2015 AC/HP, Refrigerator and Hot Water Heater Shipments, https://www.ahrinet.org/App_Content/ahri/files/Statistics/Monthly%20Shipments/2015/December_2015.pdf

AHRI, December 2019 AC/HP, Refrigerator and Hot Water Heater Shipments, http://www.ahrinet.org/App_Content/ahri/files/Statistics/Monthly%20Shipments/2019/December_2019.pdf

AHRI, February 2020 AC/HP, Refrigerator and Hot Water Heater Shipments with AC/HP by capacity. https://www.ahrinet.org/App_Content/ahri/files/Statistics/Monthly%20Shipments/2020/February_2020.pdf

"AHRI Releases December 2019 U.S. Heating and Cooling Equipment Shipment Data" (2020). Air-Conditioning, Heating & Refrigeration Institute (AHRI), http://ahrinet.org/App_Content/ahri/files/Statistics/Monthly%20Shipments/2019/December_2019.pdf.

Avallone, E.A. and Baumeistter, T., *Marks' Standard Handbook for Mechanical Engineers* (2018). McGraw-Hill Education, pp. 13–15.

Bacellar, D., Li, S., Martin, C., Shabtay, Y., Black, J. Evaluation of Contact Resistance and Fin Effectiveness of Enhanced , Brazed "Dogbone" Fin and Serpentine Tube Heat Exchangers for Air Conditioning and Heat Pump Applications. (2021). *International Refrigeration and Air Conditioning Conference*. Paper 2105.

Boesing, D., "Dissimilar Metals And The Risk of Galvanic Corrosion in Mating Connectors" (2015). *The Samtec Blog*. blog.samtec.com/post/dissimilar-metals-in-mating-connectors/.

Bowers, C. D., et al., "Accelerated Thermal Cycling test for Heat Exchangers Used in Reversible Heat Pump" (2014). *International Refrigeration and Air Conditioning Conference*. Paper 1459.

BTO Market Calculator. http://trynthink.github.io/scout/calculator.html.

Buss Almeida, V.A. and Hoch, B.O., "Failure Analysis of Brazed Joints—A Case Study." (2019). Journal of Failure Analysis and Prevention, vol. 19, pp. 809–813. doi:10.1007/s11668-019-00664-4.

"Central Air Conditioners and Air-Source Heat Pumps" (2021). Air-Conditioning, Heating, & Refrigeration Institute (AHRI). http://www.ahrinet.org/site/496/Resources/Statistics/Historical-Data/Central-Air-Conditioners-and-Air-Source- Heat-Pumps.

Chemours (2016). Opteon-XL41_PIB.pdf.

Cevallos, J.G., et al., "Polymer Heat Exchangers - History, Opportunity and Challenges" (2012). *Heat Transfer Engineering,* vol. 33, no. 13, pp. 1075-1093. doi: 10.1080/01457632.2012.663654.

Deru, M. and Torcellini, P., "Source Energy and Emission Factors for Energy Use in Buildings (Revised)" (2007). National Renewable Energy Laboratory.

"Dragon 15/20 - Induction Brazing Robot" (2021). UltraFlex Power Technologies. ultraflexpower.com/induction-products/induction-heating-systems/dragon-15-the-induction-brazing-robot/.

EIA. 2015. *Residential Energy Consumption Survey.* Table Hc7.2.

ElSherbini, A.I.; Jacobi, A.M.; and Hrnjak, P.S., "Experimental investigation of thermal contact resistance in plain-fin-and-tube evaporators with collarless fins" (2003). International Journal of Refrigeration, vol. 26, pp. 527-536. doi: 10.1016/S0140-7007(03)00007-0.

EPA (2019a). Inventory of US Greenhouse Gas Emissions and Sinks: 1990-2017.

EPA (2019b). US GHG Inventory 2019: Annex 3 additional source or sink categories part A.

Fletcher, J., "Refrigerant poisoning: Causes, symptoms, and treatment" (2018). https://www.medicalnewstoday.com/articles/322165#treatment.

Goetzler, W.; Guernsey, M.; and Young, J., "Research & Development Opportunities for Joining Technologies in HVAC&R" (2015). *Office of Energy Efficiency and Renewable Energy*, p.11.

Goswami, D.Y., et al., "Effect of refrigerant charge on the performance of air-conditioning systems" (1997) ***Proceedings of the Thirty-Second Intersociety Energy Conversion Engineering Conference*** **(Cat. No.97CH6203), vol. 3, pp. 1635-1640.**

Hussein, A., et al., "Review of polymers for heat exchanger applications: Factors concerning thermal conductivity" (2017). ***Applied Thermal Engineering,*** **vol. 113, pp. 1118-1127. doi: 10.1016/j.applthermaleng.2016.11.041.**

Jiang, H.; Aute, V.; and Radermacher, R., "CoilDesigner: a general-purpose simulation and design tool for air-to-refrigerant heat exchangers" (2006). ***International Journal of Refrigeration,*** **vol. 29, pp. 601-610. doi: 10.1016/j.ijrefrig.2005.09.019.**

McCracken, S. A., "Evaluation of Joining Techniques for Copper Tubing in AC&R Applications" (1997). Air-Conditioning and Refrigeration Technology Institute (AHRI).

McCracken, S.A. and Beal, R.E., "Evaluation of Joining Techniques for Copper Tubing in AC&R Applications--Part Two" (1998).

Miljkovic, N., et al. "Improved Braze Joint Quality Through Use of Enhanced Surface Technologies" (2019). 2019 Building Technologies Office Peer Review, Arlington, VA.

Meeker, W. Q, et al., "Using Accelerated Life Tests Results to Predict Product Field Reliability" (2009). ***Technometrics*****, vol. 51, pp. 146-161. doi: 10.1198/TECH.2009.0016.**

Thurman, J. and Scanlan, J., "Refrigerant Management/Leak Checking 101" (2007). The Food Industry Association.

Schmidt, T., "Heat transfer calculations for extended surfaces" (1949). ***Refrigerating Engineering,*** **vol. 4, pp. 351-357.**

"SOLVAY - asking more from chemistry," (2017). Solvay. http://www.solvay.com.

Somani, V., "Heat Exchanger Corrosion: Fundamentals to Application" (2017). ASHRAE 2017 Winter Conference, Las Vegas, NV.

Tajfar, M.; Ganjeh, E.; and Mirbagheri, M.H., "Evaluation of Copper Brazed Joint Failure by Thermal-Fatigue Test Applicable in Heat Exchangers" (2015). ***Journal of Alloys and Compounds*****, vol. 656, pp. 347–356. doi: 10.1016/j.jallcom.2015.09.276.**

"Troubleshooting Brazing Joints" (2021). The Harris Products Group, www.harrisproductsgroup.com/en/Expert-Advice/tech-tips/troubleshooting-brazing-joints.aspx.

Wang, C. et al., "Heat transfer and friction correlation for compact louvered fin-and-tube heat exchangers" (1999). *International Journal of Heat and Mass Transfer*, vol. 42, pp. 1945-1956. doi: 10.1016/S0017-9310(98)00302-0.

Wang, C.; Lee, W.; and Sheu, W., "A comparative study of compact enhanced fin-and-tube heat exchangers" (2001). *International Journal of Heat and Mass Transfer,* vol. 44, pp. 3565-3573. doi: 10.1016/S0017-9310(01)00011-4.

Zhang, M., et al., "Life Cycle Climate Performance Model for Residential Heat Pump Systems" (2011). 35.

10. Appendix A: CFD Settings

CFD settings:

1. **Mesh size: 1.0mm (polyhedral elements)**
2. **Boundary layer: 3.0mm, 10 layers, 1.2 growth**
3. **Dry air – ideal gas**
4. **K-e realizable turbulence model**
5. **B. C.: uniform inlet velocity/temperature; constant wall temp.**
6. **Steady-state**

With the transition to ANSYS, new CFD settings were established:

- **Computational domain resolution size: 2.0M elements (hexahedrons and tetrahedrons)**
- **Average element size: 0.11mm**
- **Boundary layer: 0.55mm, 16 layers, 1.2 growth**
- **Dry air – ideal gas**
- **K-e realizable turbulence model**
- **B. C.: uniform inlet velocity/temperature; constant wall temp.**
- **Steady-state**

Table 28 shows the comparison of the airside thermal-hydraulic characteristics between the correlation (Wang, et al., 2001) and CFD simulations using Star CCM+ and ANSYS 18.0. All methods predicted the heat transfer coefficient within a small range (standard deviation of ~3W/m²K). The pressure prediction using ANSYS was much closer to the correlation prediction, with a difference of 14% as opposed to the 94% encountered between Star CCM+ and the correlation. For residential coils, values on the order of 50Pa are more typical. This study verified the CFD models.

Table 28: CFD vs. Correlation (Wang et al., 2001) for the Indoor HX.

Metric	Correlation	CFD Star CCM+	Rel. Diff (against corr.)	CFD ANSYS	Rel. Diff (against corr.)
η_o*h (W/m².K)	82.05	80.18	-2.28%	84.14	2.55%
η_o (Schmidt)	0.81	0.74	-8.64%	0.79	-2.88%
h (W/m².K)	101.3	108.8	7.40%	107.0	5.59%
ΔP (Pa)	45.8	89.1	94.54%	52.3	14.13%